Non-linear optical effects in cold and hot rubidium gases

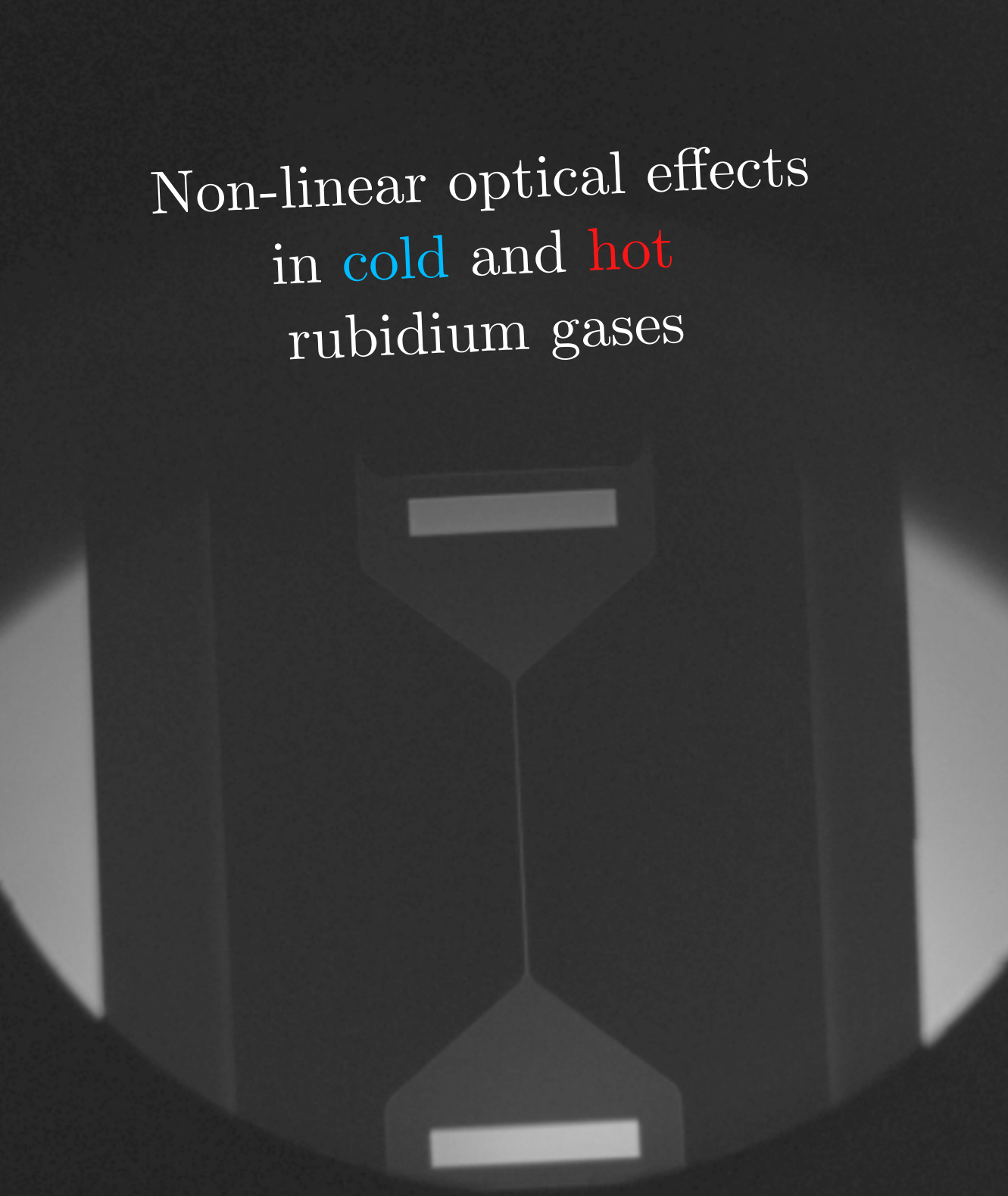

Arjon van Lange

NON-LINEAR OPTICAL EFFECTS IN COLD AND HOT RUBIDIUM GASES

Arie Johannes van Lange

Cover

The front cover shows a microscope image of a bridge waveguide, with tapered launchpads at each side. The launchpads contain the surface grating couplers designed in chapter 2 of this thesis. The freestanding, 200 nm wide and 100 µm long bridge was fabricated using e-beam lithography in a 220 nm thin silicon nitride membrane by Andries Lof at the Amolf Nanolab Amsterdam. The image is taken in the Fourier microscope setup shown in figure 2.5, with white light illumination using an LED.

The back cover shows an image of the same bridge waveguide, which is mirrored to represent the bottom view of the sample. It is best viewed by holding the thesis face up and lifting it over your head to investigate the 'sample' from underneath. For this image, the bottom launchpad is illuminated with laserlight with a wavelength of 780 nm under an angle of 3° from normal incidence. The light is coupled into the membrane and funneled into the waveguide bridge. A bright spot is visible at the waveguide bridge entrance due to enhanced scattering. The light then travels through the bridge and is coupled out at the top launchpad. The image demonstrates that light can be coupled into the nanophotonic waveguide bridge using surface grating couplers under near-normal incidence.

Nanophotonics
Debye Institute for Nanomaterials Science
Departement Natuur- en Sterrenkunde
Faculteit Bètawetenschappen
Universiteit Utrecht

Printed by Gildeprint, Enschede
ISBN 978-90-393-7309-5
DOI 10.33540/107

Non-linear optical effects in cold and hot rubidium gases

Niet-lineaire optische effecten in koude en hete rubidium gassen

(met een samenvatting in het Nederlands)

PROEFSCHRIFT

ter verkrijging van de graad van doctor
aan de Universiteit Utrecht op gezag van
de rector magnificus, prof. dr. H. R. B. M. Kummeling,
ingevolge het besluit van het college voor promoties
in het openbaar te verdedigen
op woensdag 26 augustus 2020
des ochtends te 11.00 uur

door

Arie Johannes van Lange

geboren op 8 oktober 1985 te Haarlem

Promotor: Prof. dr. P. van der Straten
Copromotor: Dr. D. van Oosten

This work is financially supported by the *Nederlandse organisatie voor wetenschappelijk onderzoek* (NWO). A significant in-kind contribution (sample fabrication) was received from the AMOLF NanoLab Amsterdam.

Contents

1 Introduction

Look around you. Everything you see is the result of interactions between light and matter. After all, every ray of light entering your eyes has interacted with matter in some way. Or in fact, in precisely such a way, that the world looks the way it does. If you look at it this way, everyone is a lifelong expert in light-matter interaction; using it day-in day-out to make sense of world, exactly knowing how to interpret and react to the light that hits your eye. But knowing how to use a concept and truly understanding it, are two completely different things! Especially in the eyes of the physicist.

Light-matter interaction does not only influence our life in this practical manner. The electronic devices we use every day also rely heavily on the interaction of light with matter, especially for communication. Messages sent over the internet travel as packets of light through glass fibre cables, are received in the device and converted to an electronic signal using this interaction. In the future electronic devices might be replaced completely by photonic devices, in which the signal can remain a photon. But even then, the manipulations to the signal must still be performed through light-matter interaction, because photons cannot interact with one another directly. Well, at least not at reasonable energy scales. Therefore matter is required to mediate the interaction to alter the signal in the desired way. As photonic chips become smaller and smaller, the functional elements on such photonic integrated circuits have to shrink to sizes for which interactions approach their fundamental limit. It is therefore important to acquire a fundamental understanding of the interaction between light and matter. In this thesis, the fundamental building block of matter, the atom, is used to probe this fundamental interaction on the nanoscale.

1.1 Photonics

The speed of calculations of electronic chips is eventually and inevitably limited by the speed of the electrons. Therefore a switch to light (photons) as information carrier in such devices is a logical option to further enhance the performance of these computational chips. After all, nothing moves faster than light. For this transition, the functional parts in an electronic device, e.g. the transistor, need to be replaced with parts with similar functionality in a photonic device [1, 2]. The logical operations applied to electronic signals thus need to be translated to logical operations on photonic signals. Unfortunately these operations cannot be performed with light alone, because light does not interact with other light directly. When two light beams cross paths with each-other they appear unaltered at the other side: there is no such thing as a collision for photons. To circumvent this issue, matter should be present at the crossing of the light beams to mediate the interaction between photons [3]. For all-optical devices the understanding of of light-matter interactions is thus essential for the design of functional parts of photonic integrated circuits [4]. In this thesis we aim to probe the fundamentals of the interaction, rather than work towards a specific functionality.

Nanophotonics

In the photonic integrated circuits mentioned above, light is typically confined to a thin device layer. The functionality is achieved by suitably designed dielectric and metallic nanoscale structures. Here we enter the realm of nanophotonics and nano-optics, the study of light on the nanoscale [5]. This field encompasses all phenomena in which light is confined to smaller features than its own vacuum wavelength. The confinement is typically supplied by structuring matter on the nanoscale. In photonic crystals the periodic sub-wavelength structures in the material can guide, slow and trap light [6, 7]. In plasmonic structures the nanoshapes of metals are used to design and develop nano-antennas and nano-waveguides [8–10]. These antennas can be used to connect the confined optical near-field to the free space optical far-field with a broadband operating range. Light can also be confined in dielectric waveguides, from which the connection to the far-field is often performed by surface grating coupling [11–14]. This technique is especially common practice in photonic integrated circuits [15]. Confined to these sub-wavelength features, light can exhibit high peak intensities and high field gradients interesting for non-linear optics. This allows for precise spectroscopy measurements and spectroscopic sensing [16, 17], electromagnetically induced transparency and slow light propagation to boost intensity [18] *and* for sensing and trapping (cold) atoms. Since atoms are the fundamental building blocks of matter and their behaviour is well documented [19], the interaction of atoms with the intense light in nanophotonic structures, opens a way to understand the fundamentals of the interaction.

1.2 Cold atoms and hot atomic vapours

Laser cooling and trapping of neutral atoms was developed in pursuit of a Bose Einstein condensate (BEC) of neutral atoms. BEC was first achieved in 1995 in a dilute rubidium gas [20] and in a dilute sodium gas [21], for which the Nobel Prize for physics was awarded to Ketterle, Wieman and Cornell in 2001. The ability to trap and cool atoms down to $\sim 100\,\mu K$, also opened up the possibility of loading them into more sophisticated and versatile traps. Atoms have been trapped in all-optical traps acting as optical tweezers and in optical lattices [22], which opened the door for cold atoms as a highly controllable model for other physical systems and to perform quantum simulations [23]. Atoms trapped in hollow-core optical fibre waveguide trap can create effective photon-photon interactions [24, 25]. For even smaller traps for cold atoms, nanophotonic structures are used. Atoms have been trapped in the evanescent field of a nanocavity in a 1D photonic crystal on the tip of a tapered fibre [26, 27], in the evanescent field of a bottleneck resonator in a stretched fibre [28–30] and in an alligator resonator trap in a waveguide bridge in vacuum [31–33]. In addition, several other traps have been proposed, including nanoplasmonic traps [34–36] and a single atom trap around a nanocavity in a 1D photonic crystal in a waveguide bridge, that requires only a fraction of a photon to trap an atom [37]. In these experiments, small numbers of atoms are trapped by a small amount of light. Conversely, only small amounts of light are required for non-linear optical effects due to saturation of the small number of atoms. These small signals can however make it difficult to measure and unravel the non-linearity of the interactions.

Nonlinear effects in the interaction between light and matter can also be studied in hot atomic vapours, where a high density of atoms interact with high intensity light. Here we see remarkable phenomena, such as electromagnetically induced transparency, in which an originally opaque dense vapour becomes transparent when excited with an intense control beam of laser light [38–40]. In slow-light experiments, the group velocity of the light is reduced by several orders of magnitude compared to the speed of light in vacuum [41, 42]. This dramatic reduction of speed to almost zero led to effectively storing light pulses in dense atomic vapours [43–47], which shows great promise in quantum network communication and synchronisation [48, 49].

The non-linear behaviour also has an intriguing effect on the beam profiles of light travelling through a dense vapour. At frequencies below the atomic resonance, the propagation of the optical field was found to be analogous to the time evolution of a 2D-Bose gas with repulsive interactions [50, 51]. During propagation, a speckled input profile with random phase can steadily be converted to a coherent Gaussian beam [50]. During this gradual change, the partial coherence in the statistics allows for new applications, as it combines the properties of completely incoherent light of an incandescent light source, suitable for imaging, with the properties of purely coherent light of a laser beam, suitable for long range communication and metrology. For frequencies above the atomic resonance,

beams with extraordinary shapes have been observed emerging from a dense rubidium vapour. Gaussian beams of nearly resonant light, focused strongly in the non-linear medium have produced size-variable dark-hollow beams: optical modes with a bright ring around a dark centre [52] and Bessel-Gauss modes, which have self-reconstructing properties upon hitting an obstacle [53]. These beam shapes and statistics show great promise for use in information transfer and imaging. For the understanding of the light-matter interaction, the insight into the non-linear behaviour is valuable.

1.3 This thesis

In this thesis, we study the non-linear interaction of light with rubidium atoms in two different ways: We investigate the interaction of light confined in a thin Si_3N_4 layer with cold rubidium atoms in chapters 2 and 3, and we study the propagation of intense light through a dense rubidium vapour in chapters 4 and 5. We choose atoms, because they are the fundamental building blocks of matter. Rubidium is a common choice of atom in atom optics for its favourable, low melting point of 39.3 °C and the availability of affordable commercial laser systems at its transition wavelength of 780 nm. Silicon nitride is a suitable choice for waveguiding at wavelengths of 780 nm [54].

In chapter 2, we design and test surface grating couplers in a thin freestanding Si_3N_4 membrane to couple light into the guided mode of the membrane. We find an elegantly simple design condition to calculate the optimal grating period and find a coupling efficiency of up to 12%. In chapter 3, we prepare the versatile atom transport apparatus for photonics to measure the interaction between light in the membrane waveguide and cold atoms brought to the surface in an optical lift. Performance of the optical lift is improved and optimised to have an atom flux of 100 atoms/µs. Sensitive measurement devices, are prepared to measure a few percent drop in a 12 pW signal for transmission. Mechanical vibrations, traced back to the rotation stage motion to move the optical dipole trap, turn out to obscure the signal. A redesign of this part of the setup is required to make the versatile atom transport apparatus ready for routine operation.

In chapter 4, we study the transmission of a high intensity laser beam through a dense rubidium vapour. A model is constructed that includes non-linear effects in intensity (saturation and optical pumping) and atomic density (interaction broadening and collisional depumping). The model is compared to measurements of on-resonance transmission through a 10 cm long heated rubidium cell. We find quantitative agreement and show that all the non-linear effects mentioned above are required to understand the characteristic features in the transmission. The model is a powerful tool to calculate interaction of light and atomic vapours at high light intensity and/or high atomic density. In chapter 5, we observe characteristic profiles, such as a ring-shape emerging from the heated rubidium cell for frequencies above the atomic resonance. These shapes appear for specific detunings from the atomic resonance and at specific intensities. We follow the

detuning of these shapes as a function of intensity. The resulting detuning curves coincide with high transmission regions in the transmission spectra for the same intensities. With proper scaling, the curves collapse onto a universal dimensionless detuning curve. These observations suggest they are manifestations of the same phenomenon, for which spontaneous formation of soliton modes is the most promising explanation. We propose several research routes to investigate whether these emerging profiles are indeed the mode profiles of soliton modes.

2

Surface grating coupling into a thin Silicon Nitride layer*

For future atom-photonic devices, the incoupling method is expected to become the main bottleneck in the scaling of the number of devices, as current devices use side-coupling, which is restricted to the sample edges. In this chapter we describe how light from above is coupled directly from free space into a freestanding membrane of 220 nm thin silicon nitride (Si_3N_4) with surface grating couplers. The design for these couplers is modelled, captured in an elegant design formula and experimentally tested. A coupling efficiency of 12% makes experimental coupling to an array of atom-photonic devices possible. The elegant design formula makes grating design straightforward for all dielectric materials and wavelengths. For this formula, determination of the correct effective index of the specific waveguide mode inside the grating layer is essential.

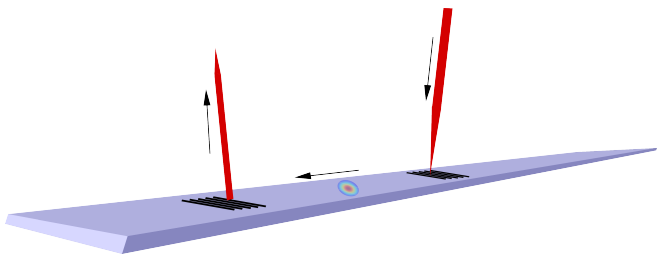

Figure 2.1 Artistic schematic of the in- and outcoupling of light by surface grating couplers and transmission through the thin Si_3N_4 membrane.

*This chapter is published as *Non-contact surface grating coupling for arrays of atom-photonic devices*, Arie Johannes van Lange, Andries Lof and Dries van Oosten, *J. Opt. Soc. Am. B* **37**(4) 921-926 (2020).

2.1 Introduction

In recent years large advancements have been made in atom-light interaction in the strong coupling regime [4]. In cavity quantum electrodynamics this strong coupling shows the promise of applications in quantum information processing [1]. Atoms have been coupled to an optical trapping field in several ways. In pioneering experiments, an ultracold atom was coupled to a microcavity with conventional mirrors [55]. The size of the cavity and consequently of the complete device has since then become smaller and smaller. As examples of such atom-nanophotonic systems, ultracold atoms were trapped in the evanescent field of light in a bottleneck resonator of a stretched fibre [28–30] and in the evanescent field of a nanocavity resonance of a 1D photonic crystal waveguide attached to the tip of a tapered fibre [26, 27]. In an alternative approach, a fibre was butt-coupled to a waveguide bridge in vacuum. In its center an alligator resonator trap was fabricated to trap the atom in its mouth [31–33]. In all these experiments two quantum objects are strongly coupled: the photon in the nanocavity and the atom. This coupling of two dissimilar quantum systems shows great promise for quantum information processing and these systems have shown basic device functionality in experiments. The next step is to make these experimental prototypes into easily addressable building blocks for large scale devices.

The scaling challenge to make an array of individually addressable blocks of these devices is similar to the scaling in electrical engineering: from a single transistor to the vast arrays of transistors constituting our modern day computer chips. Bottleneck in this progress is the available area for input and output connections. Early integrated circuits had connectors around the edges creating a 1D contact interface. The big leap forward came from addressing the devices from the top, unlocking a 2D contact interface. A similar approach for atom-photonic devices demands coupling in from the top instead of butt-coupling at the edge, whilst preserving pristine space in the vacuum for the trapped atoms. As a result, the coupling must be through free space and at a distance. In the experiments mentioned above, the devices are addressed by a single fibre or a line of fibres from the side of the sample. Surface grating couplers offer an alternative, scalable technique to inject light directly into the device membrane layer from the top at a distance.

Grating couplers were developed in the photonics industry and have become standard practice for on-chip testing of its constituent individual devices. Typically, surface grating couplers are addressed from the top and designed to operate at small angles of incidence. The large tolerance in acceptance angle, beam size and beam curvature make them convenient to use [14, 56–58]. Although generally addressed by a fibre in contact with the surface, the technique is also applicable to incoming beams of light. Surface grating couplers can couple light into the device membrane directly from free space at near normal incidence angle. Therefore, a whole array of devices can be addressed by redirecting the beam from outside the vacuum chamber. The benign tolerance in acceptance angle, beam size and

beam curvature make them convenient for large scale use. For on-wafer purposes, the efficiency is optimised for buried oxide layer thickness on the substrate and even an oxide overlayer [11, 59]. For freestanding membranes of our interest, the optimum depends more heavily on other parameters, which we capture in theory and numerical simulation. Since this technique is readily applicable to any membrane, it can provide new opportunities for experiments coupling atoms to vibrating membranes [60]. The technique is also highly compatible with the use in quantum gas microscopes [61–63].

In this work, we derive and numerically test an elegant design formula for grating pitch and depth. In the design, the correct determination of the effective index of the TE and TM fundamental modes plays a defining role. We follow the design to fabricate the grating couplers and show their behaviour experimentally in a Fourier microscope setup.

2.2 Theory of the design formula

In our design, the surface grating couplers aim to couple the first grating diffraction order into the slab waveguide mode, exploiting Wood's anomaly [64]. This requires phase matching between the beam incident on the grating grooves and the guided mode in the grating layer. In a schematic representation of the process in figure 2.2 we see the beam with wave vector $\mathbf{k}$ impinging on the grating with grating pitch Λ under an angle ϑ. The supported waveguide mode has propagation constant β. The phase matching condition for the first diffraction order is

$$k_z = \beta - K, \tag{2.1}$$

where $K = \frac{2\pi}{\Lambda}$ and $k_z = ||\mathbf{k}|| \sin\vartheta$. In this Equation, we see that the reciprocal lattice constant K overcomes the momentum mismatch between the incoming beam and the guided mode in the grating layer. The Equation can be rewritten in terms of the vacuum wavelength λ_0, such that $k_z = ||\mathbf{k}|| \sin\vartheta = \frac{2\pi}{\lambda_0} \sin\vartheta$ and $\beta = \frac{2\pi}{\lambda_0} n_{\text{eff}}$, where n_{eff} is the effective refractive index of the mode propagating in the grating slab. The phase matching condition becomes

$$\sin\vartheta = n_{\text{eff}} - \frac{\lambda_0}{\Lambda}, \tag{2.2}$$

which leads to the following design condition for the grating pitch,

$$\Lambda = \frac{\lambda_0}{n_{\text{eff}} - \sin\vartheta}. \tag{2.3}$$

From these equations, the pivotal role of n_{eff} in the design is apparent. In the thin device membrane grating layers of interest, the effective index depends significantly on the depth and duty cycle of the grating *and* on the mode profile.

Because even the fundamental mode has evanescent tails extending far into the vacuum, the effective index differs significantly from the bulk index and should be calculated with care.

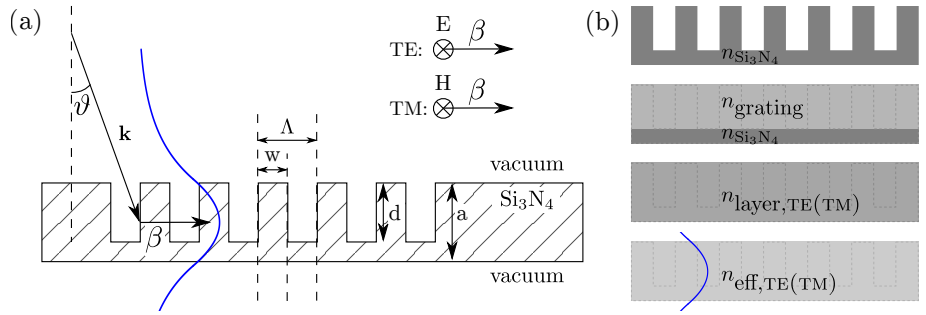

Figure 2.2 (a) Schematic representation of the incoupling process and relevant design parameters. The blue line represents the vertical profile of the electric field of the TE mode. (b) Schematic representation of intermediate effective media in the calculation of the effective refractive index for the fundamental TE (TM) mode in the membrane layer with grating. From top to bottom the initial structure of the membrane, the membrane after averaging the grating indices (horizontal averaging), th membrane after vertical averaging), and the membrane effective index for the TE (TM) mode. The blue line again represents the vertical component of the electric field of the TE mode.

2.2.1 The effective index

In the following, we consider as an example a grating in a 220 nm thick Si_3N_4 layer. For vacuum wavelengths around 780 nm, this layer only supports the fundamental transverse magnetic (TM) and transverse electric (TE) modes. The index n_{eff} appearing in equation 2.3 is the effective index of these modes in the *grating layer*. The propagation in such a layer is in general time-consuming to calculate, but simple to estimate using effective medium theory to find the bulk grating layer index and subsequent solving of Maxwell's equations for the index of the guided fundamental modes. This approach is schematically depicted in figure 2.2b.

The refractive indices for the bulk grating layer are calculated by averaging the geometrical properties of the grating layer: thickness a, groove depth d and duty cycle $f = w/\Lambda$, where w is the grating ridge width. The particular type of averaging is determined by the orientation of the polarisation with respect to the interfaces. As we will show, the zeroth order approximation of effective medium theory [65, 66] leads to excellent correspondence experiments and numerical simulations. It states that when the electric field is parallel to the interface $n_{\text{eff}}^2 = f n_1^2 + (1-f) n_2^2$ and when it is perpendicular to the interface $n_{\text{eff}}^{-2} = f n_1^{-2} + (1-f) n_2^{-2}$. It is important to note that the TE and TM mode in this work are defined with respect to the slab waveguide interface rather than the grating line interfaces.

We consider two averaging steps; first we average the grating grooves with the vacuum in between to find an effective grating index and subsequently average it with the remaining Si_3N_4 layer. The grating lines are parallel to the electric field for both the slab TE and the TM mode, such that

$$n_{\text{grating}} = \sqrt{f n^2_{\text{Si}_3\text{N}_4} + (1-f)\, n^2_{\text{vacuum}}}. \tag{2.4}$$

For the interface between the grating and the remaining Si_3N_4 layer however, the TE mode is parallel to the interface and the TM mode is perpendicular. The appropriate effective indices of the layer are thus

$$n_{\text{layer,TE}} = \sqrt{\frac{d}{a} n^2_{\text{grating}} + \left(1 - \frac{d}{a}\right) n^2_{\text{Si}_3\text{N}_4}}, \tag{2.5}$$

$$n_{\text{layer,TM}} = \left(\frac{d}{a}\frac{1}{n^2_{\text{grating}}} + \left(1 - \frac{d}{a}\right)\frac{1}{n^2_{\text{Si}_3\text{N}_4}}\right)^{-\frac{1}{2}}. \tag{2.6}$$

Subsequently, Maxwell's equations are solved for a layered medium of a slab with index $n_{\text{layer,TE(TM)}}$ surrounded by vacuum, with the appropriate boundary conditions for TE (TM) mode. The derivation follows the lines of Burke [67], but we solve the equation numerically rather than graphically. The derivation and the python code for numerically solving the resulting equation can be found in appendix A[†]. As an example, for $d = \frac{3}{4}a$ and $f = \frac{1}{2}$, which are the values for optimum coupling for similar grating structures [11, 15], we find values $n_{\text{grating}} = 1.58$, $n_{\text{layer,TE}} = 1.69$ and $n_{\text{layer,TM}} = 1.65$. The resulting n_{eff} for the fundamental TE and TM mode are wavelength dependent and the values for $\lambda_0 \simeq 780$ nm are

$$n_{\text{eff,TE}} \simeq 1.41 \qquad \text{and} \qquad n_{\text{eff,TM}} \simeq 1.20. \tag{2.7}$$

Note that these indices differ considerably from the bulk indices $n_{\text{layer,TE}}$ and $n_{\text{layer,TM}}$ due to the spatial extent of the mode wings into the vacuum. Moreover, these indices are significantly different from those of the modes supported by a 220 nm slab of Si_3N_4 without a grating, which are $n_{\text{slab,TE}} = 1.71$ and $n_{\text{slab,TM}} = 1.41$ for $\lambda_0 = 780$ nm.

2.3 Numerical calculations

To test the design condition described above, the Stanford Stratified Structure Solver (S^4) Python package[‡] is used. S^4 is a frequency domain code, which uses Rigorous Coupled Wave Analysis and an S-matrix algorithm [68] and is suitable

[†]This sentence and the appendix are not part of the original publication.
[‡]S^4 version 1.1 downloaded from `https://web.stanford.edu/group/fan/S4/install.html`

to calculate transmission through a patterned layer, i.e. a grating. Convergence is verified for the used Fourier basis of 50 Fourier orders. The excitation plane wave is varied in incident angle, frequency and polarisation. The forward transmission is measured under the grating layer over the entire grating layer. The grating layer geometry is as top image of figure 2.2b and can be considered to extent infinitely in the horizontal directions[§]. As the simulation is a closed system, the rest of the light is necessarily scattered in the backward direction. We exploit Wood's anomaly to attribute a sharp decrease in the transmission to the opening of a new reflection channel; namely light coupled into the grating layer and coupled out in the backward direction. For a plane wave this process is so effective that the transmission becomes zero due to the destructive interference between different transmission paths.

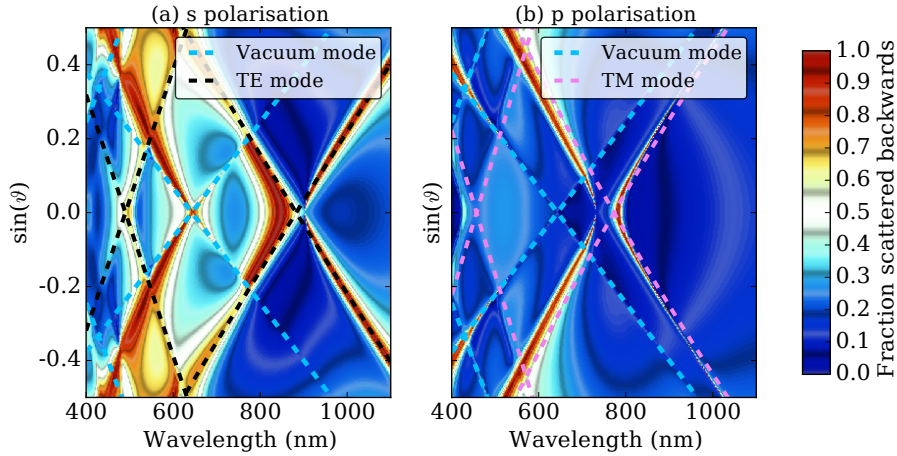

Figure 2.3 Colour plot of backward flux through a line just above a grating layer. The dashed lines are solutions of the diffraction equation (equation 2.2) for the TE mode with $n_{\text{eff}} = n_{\text{eff,TE}}$, the TM mode with $n_{\text{eff}} = n_{\text{eff,TM}}$ and the vacuum-mode with $n_{\text{eff}} = 1$.

Figure 2.3 shows the backward scattered fraction for a 220 nm thick slab with $d = 170$ nm and $\Lambda = 643$ nm for s and p polarisations. The maxima in these plots occur on specific lines in angle-wavelength space. They are symmetric around zero angle, because there is no preference in direction of the excited mode. For s (p) polarisation, the lines along which maxima occur clearly match with the calculated diffraction condition curves for the TE (TM) mode in this slab, which are indicated by the dashed lines. The design formula has thus proved to be effective and the determination of n_{eff} accurate. The TE (TM) mode is expected to be excited by s (p) polarisation, because the electric fields of the incoming beam and the slab waveguide mode are oriented in the same direction.

Our primary interest is in the TM mode in the grating layer, because this

[§]This sentence is not part of the original publication.

mode has the largest evanescent tails above the waveguide and is thus most suitable for atom-photonic applications. In experiment we therefore investigate p-polarised light coupling to the TM mode, for which we first design and fabricate the grating couplers.

2.4 Grating fabrication

The fabrication process starts with an array of membranes of stoichiometric Si_3N_4 ($n = 2.014$) purchased from Small Tech Supplies. The free-standing membranes are on a silicon support and have dimensions of 1 mm x 100 µm and 220 nm thickness.

The surface grating couplers are fabricated using focused ion beam milling (FIB) at the nanocenter of NWO-institute AMOLF in Amsterdam[¶]. Grooves are milled to a depth of $\frac{3}{4}$ of the thickness of the slab and with a duty cycle of $\frac{1}{2}$, because these values have proven to give the highest coupling efficiency for similar structures[11, 15]. The pitch is varied between 640 and 700 nm. On each of the membranes, one pitch is chosen for the gratings on that membrane. Gratings of 20 lines of 60 µm wide are placed 20, 30, 50 and 100 µm apart to test the transmission. Figure 2.4 shows electron microscope images and a cross section schematic of one of the resulting membranes.

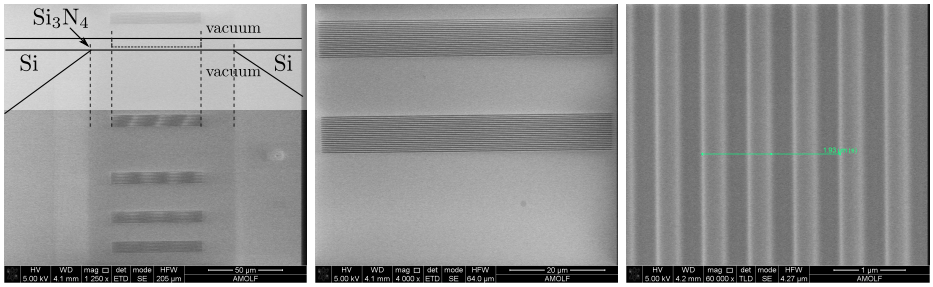

Figure 2.4 Cross section view schematic (top left overlay) and top view SEM pictures of a Si_3N_4-membrane with five fabricated grating couplers. Grating couplers consist of 20 lines with pitch 643 nm and duty cycle of 0.5. The spacing between the gratings is 20, 30, 50 and 100 μm.

2.5 Experimental setup

Samples are characterised in a microscopy setup reported in Ref. [69] with the addition of an acquisition arm (See figure 2.5). The setup combines real space and Fourier space control. More particularly, the setup can be used for controlling

[¶]FEI Helios dual beam FIB (Ga+ milling) set to 30 kV acceleration voltage, 280 pA ion beam current, 26 µs dwell time and 30 loops.

the incidence angle of light that is offered for incoupling at one location in the field of view of a microscope objective, while at the same time giving access to real space imaging of outcoupling of light at another position in the field of view. Ref. [69] provides a detailed and accurate description of the setup components as used in this work. The setup is shown schematically in figure 2.5.

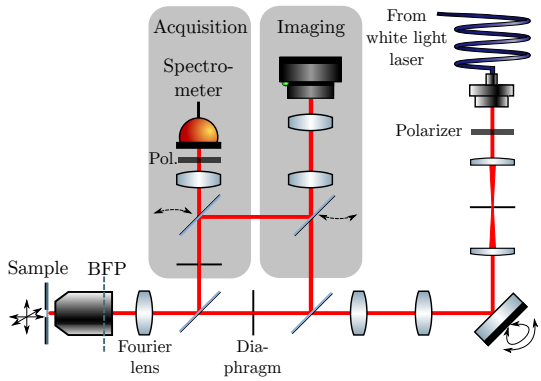

Figure 2.5 The Fourier microscope setup at NWO-institute AMOLF used to characterise the grating samples. The light source is a super continuum white light laser (NKT photonics SuperK extreme), the microscope objective is an Olympus 100x, NA 0.95 M Plan IR objective and the acquisition is performed by an Avantes peltier cooled Si CCD array spectrometer (AvaSpec-2048TEC-USB2-2).

The sample is mounted on a x,y,z-translation stage and positioned in the focus of the microscope objective. The excitation beam originating from a super continuum white light laser arrives on the table through a paddle polarisation controller. The beam undergoes polarisation and spatial filtering before arriving at two galvo mirrors on the bottom right. The two galvo mirrors allow the beam angle to be scanned in two directions. The telescope after the galvo mirrors, together with the Fourier lens, translates this angle to a well-defined spot on the back focal plane (BFP), thereby selecting a specific angle of excitation of the sample. The spot is scanned over the BFP of the objective to excite over a large range of angles consecutively.

In addition to the angle, we can also select a specific location for excitation on the sample. In the intermediate image plane before the Fourier lens, a movable diaphragm ensures that only the incoupling grating is illuminated. The sample (as well as the diaphragm opening) is imaged on the camera through the imaging arm. The sample can also be imaged through the acquisition arm by turning in a flip mirror. In this arm, a second diaphragm is placed to select the outcoupling grating. With the flip mirror in the acquisition arm removed, the light is sent to a spectrometer. This way, we scan the angle of the excitation and measure the spectrum from the outcoupling grating. A polarisation filter can be placed in the acquisition arm for cross and parallel polarisation measurements.

2.6 Results

In the experiment, light is coupled through a 220 nm thick Si_3N_4 membrane in air by two surface grating couplers separated by 20 µm as is schematically depicted in figure 2.1[‖]. Figure 2.6 shows the wavelength-angle dependence of transmission of p polarised excitation light with grating couplers with a pitch of 643 nm. The outcoupled light is verified to have parallel polarisation. The results are compared to the simulation for the same grating parameters. The diffraction condition from equation 2.2 are plotted for air (n_{eff} =1) and the TM mode in the grating slab ($n_{\text{eff}} = n_{\text{eff,TM}}$).

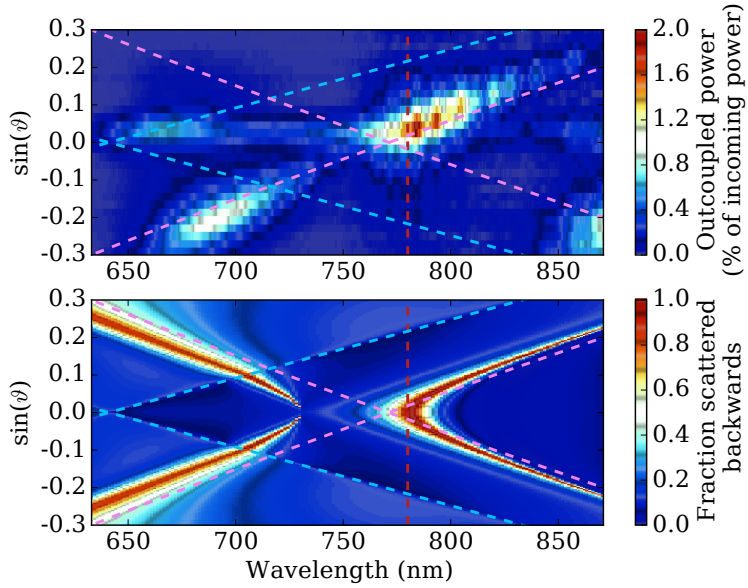

Figure 2.6 Experimental results (top) and simulation (bottom) of transmission of p polarised light through a 220 nm thin slab of Si_3N_4 surrounded by air. In- and outcoupling through a surface grating coupler with pitch 643 nm, groove depth 170 nm. Dashed lines are grating conditions for the TM mode (pink) and air mode (blue) and the resonance wavelength of rubidium (red) at 780 nm.

The maxima in transmission appear on the diffraction condition for the TM mode and also coincide with the maxima of the simulation. This further confirms the effectiveness of the design formula and the accuracy of the n_{eff} determination. In comparison with the simulation results we note the following differences.

Firstly, the experiment shows no signal for opposite angles whereas the simulation does. The simulation considers an infinite grating layer and captures modes excited in both positive and negative direction. In the experiment, only

[‖]This sentence and figure 2.1 are not part of the original publication.

the modes directed towards the outcoupling gating can be measured. Indeed, if the measured transmission direction is inverted by switching the selected in- and outcoupling grating, the graph is mirrored in the line of 0°. Secondly, in the experimental data the high transmission region near the diffraction condition line has a substructure with several maxima separated by ∼10 nm. We attribute these maxima to interference caused by partial reflection on the interfaces between the grating layer and the regular Si_3N_4 waveguide layer, which is not included in the simulation. In particular, the 20 µm long Si_3N_4 waveguide slab between the gratings would give rise to etalon modes with roughly the same wavelength separation of ∼10.5 nm.

To determine the transmission efficiency, the outcoupled power is compared to the incident power, which is measured by the spectrometer just before entering the microscope objective. Importantly, we see there is considerable transmission at 780 nm at near normal incidence. This shows that the design works and we understand how the incoupling depends on the design parameters.

To determine the optimum pitch for a given wavelength, we measure transmission for gratings with varying pitches on several membranes. We take the crosscuts at 780 nm as shown in figure 2.6. For all the pitches we combine the experimental data, simulation output and diffraction condition in figure 2.7.

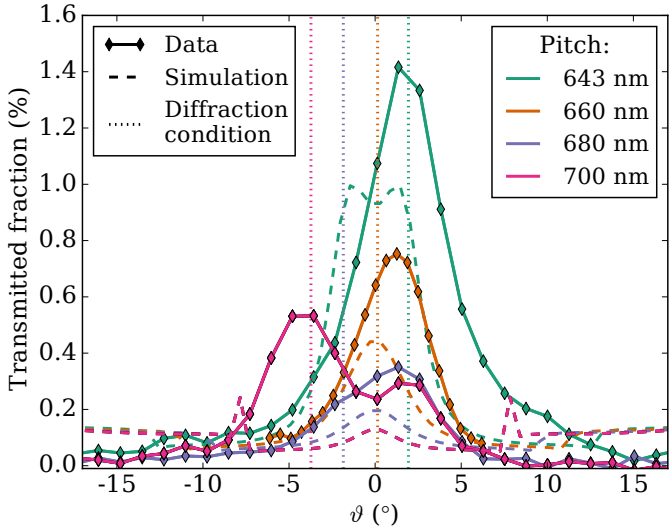

Figure 2.7 Transmission of 780 nm light for several pitches. Each pitch has its own colour. For each pitch the diffraction condition from equation 2.2 for n_{eff} of the grating layer (dash-dot vertical line), the results from simulation (dashed line) and data from experiments (connected diamonds) are drawn.

Figure 2.7 shows that design, simulation and experiment are in good qualitative agreement. The shifts in the transmission maximum for different pitches exhibit the same trend. Therefore, the design condition of equation 2.3 properly

describes the position of maximum transmission. The most suitable pitch out of this collection is 643 nm with a maximum transmission of almost 1.4% at near normal incidence. The total transmission of 1.4% indicates that the single coupler efficiency is 12%. This value is a lower limit, because the losses in the remainder of the waveguide and in the setup are included in the efficiency. The efficiency compares well to the values found in literature for a Si_3N_4 grating coupler with an unoptimised buried oxide layer and without an overgrowth layer [11] and for a Si_3N_4 grating coupler suspended in SiO_2 [56]. More advanced structures of grating couplers in suspended waveguides of Si and Ge show great increase in efficiency and functionality, which may also provide good prospects for use in silicon nitride [12, 13].

2.7 Conclusion

In conclusion, we find an elegantly simple design condition for efficient coupling and transmission at any desired wavelength and angle in thin dielectric waveguide layers. The design condition is confirmed by simulation results for a single grating coupler. We used the condition to design and fabricate surface grating couplers with efficiency as high as 12%, and achieved a total transmission efficiency through the incoupler-waveguide-outcoupler system of 1.4%. For light with a wavelength of 780 nm, the design shows optimum light transmission through a 220 nm-thick slab of Si_3N_4 for a surface grating coupler with 20 grooves with a pitch of 643 nm at a depth of 170 nm. For any choice of wavelength, dielectric material and thickness of the waveguide, optimum incoupling parameters can be easily calculated using the design formula with the correct guided mode effective index.

3

Cold atoms brought in contact with a silicon nitride waveguide

In this chapter we discuss how cold atoms are brought in contact with the Si_3N_4 membrane surface in between the surface grating couplers and what effect the atoms have on the transmission through the waveguide. Membranes are placed in a versatile atom transport apparatus for photonics, in which rubidium atoms are cooled to 100 µK in a series of magneto-optical and optical traps. These ultracold atoms are ultimately trapped in an optical lift, which lowers them into the evanescent field of the membrane waveguide mode. We optimise the velocity of the lift to have maximum atom flux to the membrane.
The goal of the experiment is to measure a small dip in transmission though the waveguide, when atoms are in the evanescent field of the waveguide mode. The resonant light coupled into the membrane waveguide must have very low power to avoid saturation of the atomic transition. Detection with an avalanche photodiode module in photon counting mode is in principle sensitive enough, however mechanical vibrations in practice obscure the expected dip in transmission.

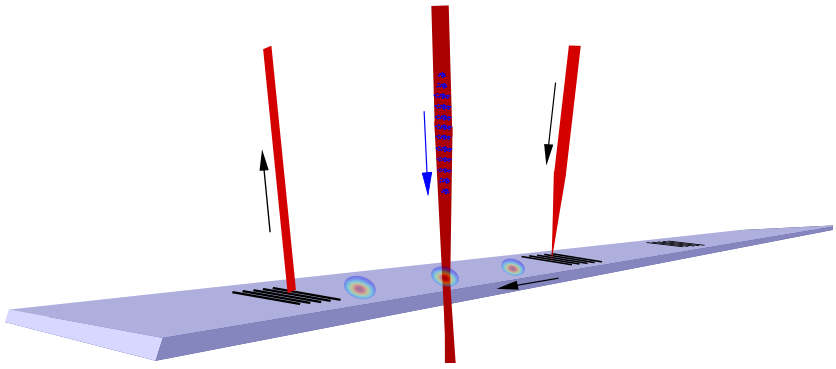

Figure 3.1 Artistic illustration of cold atoms brought into contact with the Si_3N_4 waveguide. The blue dots are the atoms, the red lines the light beams, black lines are the grating couplers and the waveguide mode is depicted as an intensity colour map on three positions along the membrane.

3.1 Introduction

The combination of the fields of cold atoms and nanophotonics has resulted in fascinating experiments revealing the interaction between cold atoms and light in nanophotonic structures. Locally, the intensity of light in these nanophotonic structures can be very high and have extremely high gradients, which can be exploited to form efficient atom traps. Atoms have been trapped in the evanescent field of a nanocavity in a 1D photonic crystal on the tip of a tapered fibre [26, 27], in the evanescent field of a bottleneck resonator in a stretched fibre [28–30] and in an alligator resonator trap in a waveguide bridge in vacuum [31–33]. In addition, several other traps have been proposed, including nanoplasmonic traps [34–36] and a single atom trap around a nanocavity in a 1D photonic crystal in a waveguide bridge, that requires only a fraction of a photon to trap an atom [37].

Usually, these experiments require highly specialised setups, designed for one of these experiments specifically. Switching to a different type of nanophotonic sample typically requires major revisions to the experimental setup and therefore a considerable amount of time. In our group a versatile atom transport apparatus for photonics has been developed and set up [70]. This sophisticated and involved setup is designed to study the interaction of ultracold rubidium atoms with light in nanophotonic samples. In this flexible experimental apparatus, the exchange of samples is performed within 30 minutes using a load-lock system, and the setup is pumped back down to operational pressures in a few hours.

In this chapter, we report on the final stages of improvements to the setup required for measuring the atom-light interaction. We insert a sample containing the devices designed in chapter 2 into this setup. Figure 3.2 shows the sample holder with sample in the apparatus, a close up of the sample in the sample holder and an optical microscope image of the sample. We characterise and optimise the optical lift to maximise the atom flux towards the surface of the membrane waveguide between two grating couplers. We couple light into the waveguide through the surface grating couplers and measure the outcoupled light from the outcoupling grating. This way we measure the transmission through the waveguide with and without atoms in the evanescent field of the waveguide. In this signal disturbances of periodic nature were observed hampering the detection of the expected dip. The source of the signal disturbance are mechanical vibrations that can be traced back to the motion of the rotation stage used to position the atoms above the sample. The amplitude of the vibrations is reduced severely, but still exceeds the expected dip in the signal caused by absorption of the atoms.

3.2 A versatile atom transport apparatus for photonics

In brief, the above mentioned experimental setup to cool, trap and position atoms operates as follows. ^{87}Rb atoms are successively caught in a 2D-magneto-optical

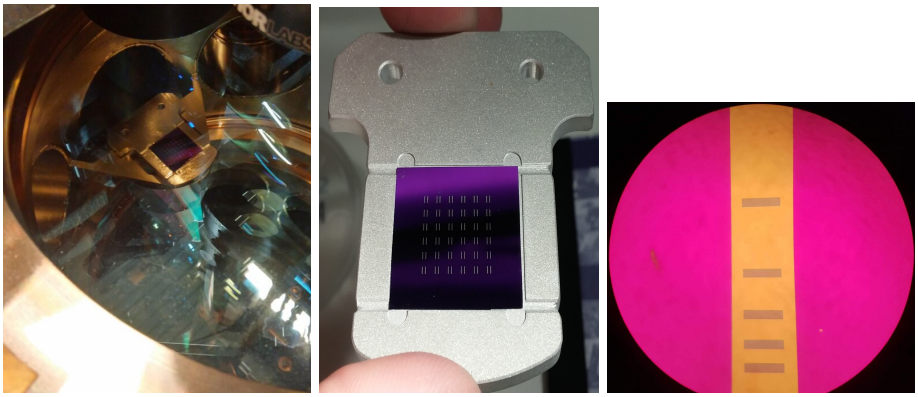

Figure 3.2 (left) The sample holder with sample on the sample table of the versatile atom transport apparatus for photonics. (centre) The sample holder with the sample containing 72 membranes. Gratings are positioned on the membranes closest to the centre. (right) Optical microscope image of the gratings on an individual membrane.

trap, 3D-magneto-optical trap, optical dipole trap and a standing wave optical dipole trap. The atoms are cooled in the magneto-optical traps to 100 µK and transferred to an optical dipole trap. In this trap, atoms are moved from the centre of the 3D-MOT to above the sample table, by rotating the last mirror of the optical dipole trap using a rotation stage. Above the sample, atoms are loaded in an optical lattice that subsequently acts as *an optical lift* to lower the atoms towards the sample surface. With the atoms close to the sample surface, we can perform experiments to measure their interaction with light in the sample.

The thesis of Mußmann [70] describes, characterises and optimises the entire setup, in which various technical challenges are overcome. Further improvements are reported by Voutyras [71]. In this chapter, we describe the parts of the setup vital for understanding the experiments and report on final improvements to the setup and optimisation of those parts of the setup.

3.2.1 Atom imaging

The atoms in the optical lift are imaged from the top by absorption imaging. The atoms are illuminated from the bottom by resonant probe light and the camera takes an image from the top. The atoms cast a shadow on the camera due to the strong absorption on resonance. To calculate the number of atoms from this image, two additional images need to be taken: a reference image without atoms but with probe light and a background image with neither atoms nor probe light. From the intensity of these images, the optical column density (OD) along the imaging axis is calculated for each pixel by

$$\mathrm{OD} = -ln\left(\frac{I_{\mathrm{atoms}} - I_{\mathrm{bg}}}{I_{\mathrm{reference}} - I_{\mathrm{bg}}}\right). \tag{3.1}$$

A typical image of the OD is shown in figure 3.3b, in which two membranes (blue) and a cloud of atoms (yellow) are clearly visible. The areas outside the membrane, where probe light is blocked by the substrate of the sample, are too noisy to pass the threshold for analysis and are left blank in the image.

The total number of atoms can now be calculated by

$$N = \frac{MA_{\text{pixel}}}{\sigma_0}\left(1 + \frac{\alpha I}{I_{\text{sat}}}\right)\sum_{n,m}\text{OD}(x_n, y_m), \tag{3.2}$$

where $M = 4.4$ is the magnification of the imaging system, $A_{\text{pixel}} = 55\,\mu\text{m}^2$ is the pixel area, $\sigma_0 = 3\lambda^2/(2\pi)$ is the on-resonance absorption cross section, n and m are the pixels in the region to be summed over. In figure 3.3b, this region is bounded by the white circle surrounding the atom cloud, and a background atom number is determined in the other white circle to correct for any differences in the probe intensity between image and reference image.

The term $1 + \frac{\alpha I}{I_{\text{sat}}}$ is the saturation correction, with $I_{\text{sat}} = 1.666\,\text{mW/cm}^2$, I the intensity of the probe beam at the atom location and α the average transition strength over the probe time span. The latter two parameters are difficult to determine directly, because α changes during probing due to optical pumping and the beam waist and power cannot be measured in situ in the vacuum chamber. Instead, the input probe power P_{in} is measured outside the vacuum chamber. We define $\eta P_{\text{in}} = \alpha I$ and determine the parameter η by demanding the atom number to stay constant for measurements at several input powers P_{in}. After all, the atom number should not depend on the probe power. We find $\eta = 14\,\text{cm}^{-2}$ for $P_{\text{in}} \simeq 40\,\mu\text{W}$ and a probe time of $50\,\mu\text{s}$, where we note that η is an effective inverse beam area, that includes the effective transition strength and losses before reaching the atoms' location in the vacuum chamber.

3.2.2 The optical lift

Trapped above the sample surface in an optical lattice of two counterpropagating laser beams, the atoms are ready to be transported to the sample surface (see figure 3.3a). When we apply a frequency difference Δf between the two laser beams, the lattice is set in motion and acts as an optical lift for the rubidium atoms. The lift moves the atoms by one laser wavelength every $t = 1/\Delta f$, such that the velocity of the atoms is given by

$$v = \lambda_c\,\Delta f, \tag{3.3}$$

where the centre wavelength of the laser $\lambda_c = 780.525\,\text{nm}$, is detuned half a nanometer from the ^{87}Rb D_2-line. In the experiment $\Delta f(t)$ is chosen as the trapezoid shown in figure 3.4a. The distance travelled can be written as

$$d = \int_0^{t_{\text{hold}}} v dt = \int_0^{t_{\text{hold}}} \lambda_c\,\Delta f(t) dt \tag{3.4}$$

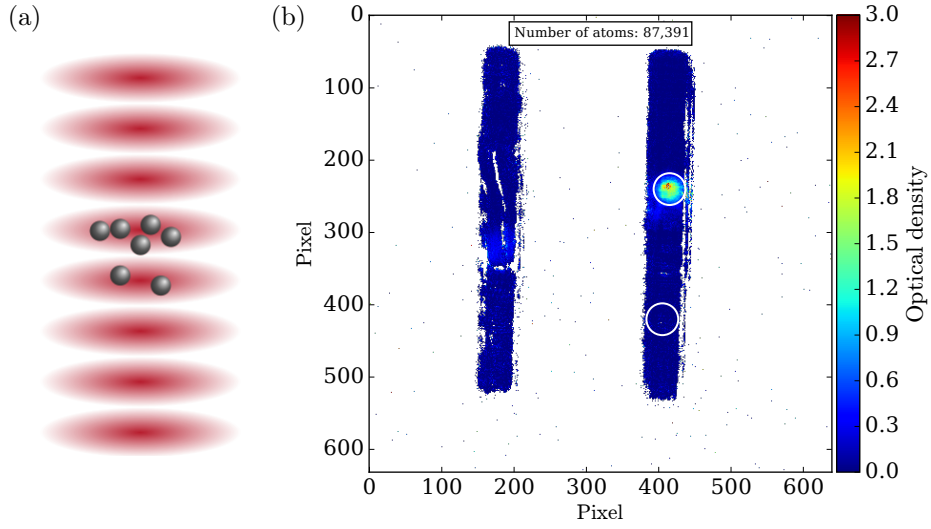

Figure 3.3 (a) Artistic impression of the atoms in the optical lattice. (b) A typical image of OD is shown in figure 3.3b, in which two membranes (blue) and a cloud of atoms (yellow) are clearly visible. The areas outside the membrane, where probe light is blocked by the substrate of the sample, are too noisy to pass the threshold for analysis and are left blank.

where t_{hold} is the time the atoms are held in the lattice. At $t = t_{\mathrm{hold}}$ the lattice beams are switched off and the atom can be imaged. The atom numbers determined from images at different hold times are plotted as a function of distance travelled in a so-called crash curve. Figure 3.4b shows typical examples of such curves with and without a transparent sample on the sample table. The curves have been corrected for static losses, which are determined in an experiment with $\Delta f_{\mathrm{max}} = 0$. In the case with the sample, the atoms are clearly crashing onto the sample surface and the sample position with respect to the loading point of the optical lattice can be estimated by eye to be 6 mm.

The main purpose of the atoms in the lift is to provide a measurable dip in signal in the transmission through the sample waveguide. Therefore, the number of atoms that light in the sample can interact with should be as large as possible. The lattice performance is optimised to have minimal atom loss during motion and maximum atom flux towards the sample surface. Optimum values for Δf_{max} to achieve minimum atom losses are in the range of $0.8\,\mathrm{MHz} < \Delta f_{\mathrm{max}} < 2\,\mathrm{MHz}$, because for higher and lower Δf_{max}, a considerable fraction of atoms is unable to follow the lattice and are left behind on the loading site [71]. The atom flux through the sample surface $\frac{\partial N_{\mathrm{atoms}}}{\partial t}$ can be calculated from the crash curve slopes

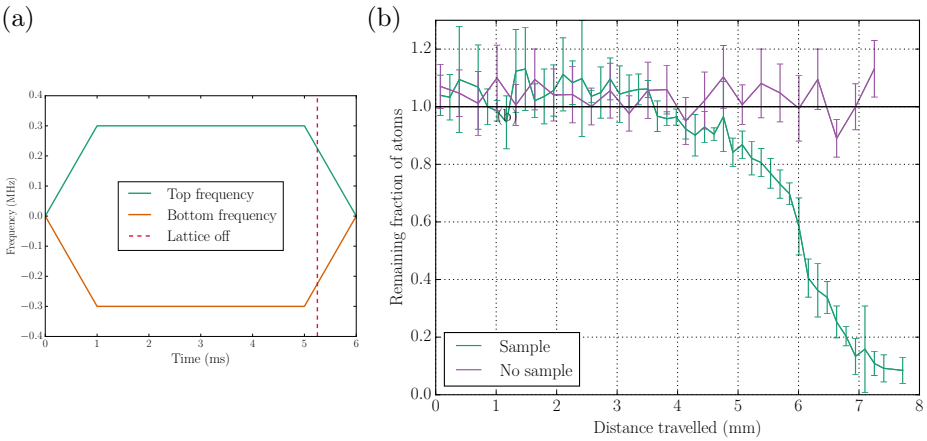

Figure 3.4 (a) The difference frequency applied top and bottom beam. (b) A resulting crash curve with (blue) and without (purple) a sample in the vacuum chamber. The blue curve loses atoms rapidly around 5.5 mm, where the sample surface is thus estimated to be. The remaining fractions have been corrected for static losses measured with $\Delta f_{\max} = 0$.

by

$$\frac{\partial N_{\text{atoms}}}{\partial t} = v\frac{\partial N_{\text{atoms}}}{\partial z} = \lambda_c \Delta f \frac{\partial N_{\text{atoms}}}{\partial z}, \tag{3.5}$$

where $\frac{\partial N_{\text{atoms}}}{\partial z}$ is the slope in the atom crash curve, without the correction for static losses.

Figure 3.5 shows these curves for $\Delta f_{\max} = 0.8, 1.6$ and $2\,\text{MHz}$. For all $\Delta f_{\max}$ the slopes are similarly steep $\frac{\partial N_{\text{atoms}}}{\partial z} \simeq 65\,\mu\text{m}^{-1}$, such that the maximum atom flux is $\frac{\partial N_{\text{atoms}}}{\partial t} \simeq 100\,\mu\text{s}^{-1}$ at $\Delta f_{\max} = 2\,\text{MHz}$. These crash curves and atom rates show a large improvement compared to earlier results [70]. This improvement is mainly the result of the inclusion of optical isolators in the beam paths of the lattice beams. These isolators prevent unwanted reflections from causing a static optical lattice to be superimposed onto the optical lattice, which hamper the atom transport.

3.3 Interaction experiments

A schematic view of the interaction measurements is shown in figure 3.6. Atoms are lowered towards the surface while the transmission through the waveguide slab is monitored. As a result of the presence of the atoms, a dip should appear in the transmission as atoms interact with the evanescent field of on-resonance light in the waveguide. For the dip to be significant, the atom flux should be as high as possible and the probe light intensity should be low enough to avoid

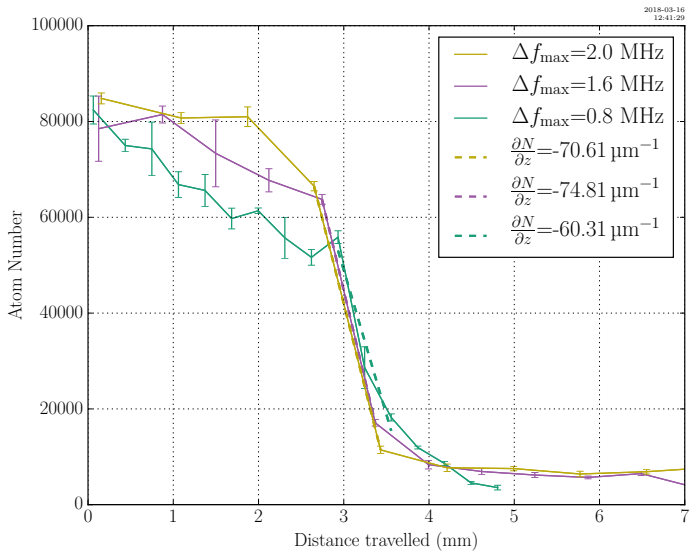

Figure 3.5 Crash curves for several values of $\Delta f_{\max} = 0$. The dotted lines are linear fits of the region of sharp decrease with a slope $\frac{\partial N_{\text{atoms}}}{\partial z}$ listed in the legend.

saturation of the atoms. In other words, the dip is measurable when a significant fraction of the light in the waveguide is absorbed by the atoms in the evanescent field of the waveguide mode.

In previous work in our group [70], an estimate was made of the expected signal-to-noise ratio for the proposed photon counting experiment. This was done using a simulation of atom trajectories through the evanescent field around a bridge waveguide. This simulation predicted a signal-to-noise ratio of 2.8 for a beam power of 12 pW and an atom flux of $\frac{\partial N_{\text{atoms}}}{\partial t} \simeq 6\,\mu\text{s}^{-1}$. In comparison to this analysis, the atom flux is a factor of 20 higher, which gives us a significant advantage over the previous estimate. However, in the detection, the outcoupling efficiency of 12% and losses of optical elements before the measuring apparatus have to be taken into account, such that the signal-to-noise ratio expected with the current parameters is around 5.

To achieve this signal to noise ratio, we should illuminate the incoupling grating with a beam power of 1.2 nW to couple $\sim$ 120 pW into the waveguide and measure the outcoupled signal of $\sim$ 12 pW. For detection of these small signals a photon-counting detector is required.

3.3.1 Detection setup

The part of the setup for imaging and detection is shown in figure 3.7. We need a photon-counting detector for the measurement and a camera and an avalanche photodiode for alignment. The imaging signal comes in from the left and has an intermediate image-plane at the position of the pinhole. Mirrors can be placed

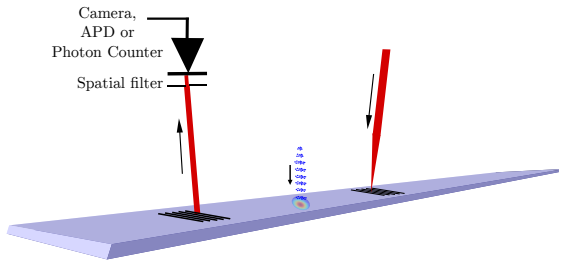

Figure 3.6 Schematic view of the interaction measurements. While atoms are lowered to the surface, the transmission through the waveguide is measured to detect the atom-light interaction.

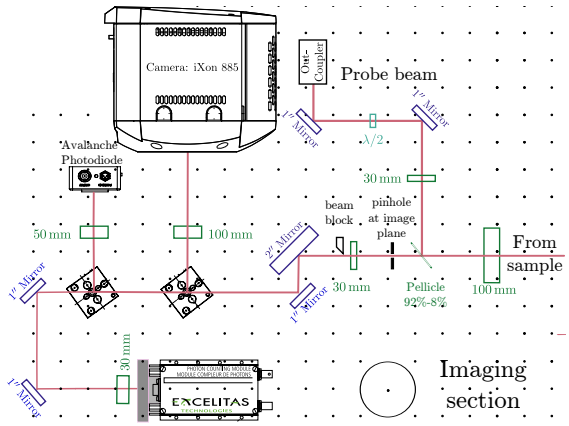

Figure 3.7 Imaging and detection part of the setup. The outcoupled signal from the sample comes in from the right, has an intermediate image plane at position of the movable pinhole. Mirrors can be placed on (or removed from) magnetic mounts to select one of three detection apparatus: a camera (Andor iXon885), an avalanche photodiode (Thorlabs APD-130A) or a single photon counter (Excelitas SPCM–780–10). Crash curve experiments and pinhole positioning on the outcoupling grating is performed using the camera. The avalanche photodiode is used in combination with a lock-in amplifier (Stanford Instruments at 520 MHz) and the signal is recorded by a data acquisition card (National Instruments NI-USB-6211). The probe beam, which is coupled into the membrane waveguide, is also in the figure and is injected into the same beam path at the position of pellicle.

on magnetic mounts to direct the signal to the various imaging and detection options, i.e. camera, photodiode or photon counting module. After taking the crash curves on the camera without the pinhole, the 100 µm pinhole is positioned to select the outcoupling grating using the camera image to align the pinhole. We then proceed to measure a time resolved signal on the avalanche photodiode to check the time dependence of the signal and to determine the timing for a photon counting experiment. The avalanche photodiode is used in combination

with a lock-in amplifier and a data acquisition (DAQ) card, which samples points with 250 kHz. Finally, a photon counting experiment can be conducted, in which the lattice beams are turned off and the incoupling beam is turned on at the time the atoms crash into the surface and the signal can be recorded by the photon counter. In this way, resonant stray light of the probe beam cannot cause any extra atom losses throughout the atom movement and stray light from the powerful lattice beams cannot interfere with the signal from the outcoupler.

3.3.2 Interaction measurements

In the time resolved measurement, the probe is turned on just before the start of the lattice motion and is left on till the end of the experimental cycle. Figure 3.8 shows the resulting lock-in amplified signal of the APD. Between the blue vertical lines, the lattice beams are on and the lattice is in motion. The large peak after turning the lattice on and before turning the lattice off, are caused by the lattice frequency Δf sweeping over the lock-in frequency and can be ignored in the analysis. The thick red line is the average APD-signal over 50 runs, of which ten individual runs are also shown in the figure. These individual runs show a large fluctuation, but by averaging over a large number of runs a small dip should still be measurable. The average of these runs however, shows a strong periodic fluctuation, which has a larger amplitude than the dip we intend to measure.

The source of the fluctuation is a mechanical vibration in the setup, due to the motion of the rotation stage which moves the optical dipole trap to the sample surface. Unfortunately, this movement is an essential part of the experimental cycle and the rotation stage itself is deeply embedded in the setup. Efforts to decouple the rotation stage from the rest of the setup and to optimise acceleration, deceleration and weight distribution of the rotation stage, have led to a large reduction of the vibration, of which figure 3.8 is already the outcome. A subtraction of the prevailing periodic signal would allow measuring of the small signal, but the timing of the experiment must be very stable for this method to work. The rotation stage however experiences timing jitter, because its internal clock cannot be synchronised with the experimental timing. Therefore, the phases of the periodic signals are different for all of the individual runs and a photon counting experiment is not feasible.

For the time resolved measurements on the APD however, the vibration *can* be removed by shifting the signals of individual runs to get the vibrations in phase. Although the signal dip is estimated to be too small to discern for this detection method, the magnitude of the dip and the sensitivity of detection might have been underestimated. To subtract the periodic fluctuation from the measurement signal we follow the following procedure. First, we take transmission traces with atoms and reference traces without atoms. The reference traces are then shifted in phase by optimising the overlap in the region between the two red lines. Traces are shifted to find the best overlap in this region for each run individually. The average periodic fluctuation during the move (between the blue lines) is then determined by the average of the shifted signals of the reference sig-

nal. Then, the traces of the interaction measurement are also individually shifted to overlap with the reference in the region between the red lines. To prevent the offsets from smearing out the dip, only the runs with an offset between $-250\,\mu s$ and $250\,\mu s$ are taken into account. The average of these lines is taken and the average periodic fluctuation (from the reference) is subtracted. Figure 3.8 shows the resulting shifted transmission traces of the selected 31 runs minus the average of the shifted reference traces. The signal is clearly smoother and small amplitude fluctuations are visible. Optimists would see a dip around 5.8 ms, when atoms arrive at the surface. The amplitude does however not exceed fluctuations elsewhere in the signal and furthermore the dip is not reproducible. Performing the experiment with different speeds of the optical lift, power of the probe light and timing of the probe light switching could not produce an average trace with a significant dip. We conclude that the setup is not stable enough to measure with the required sensitivity to measure the small changes in signal, which the interaction is expected to cause.

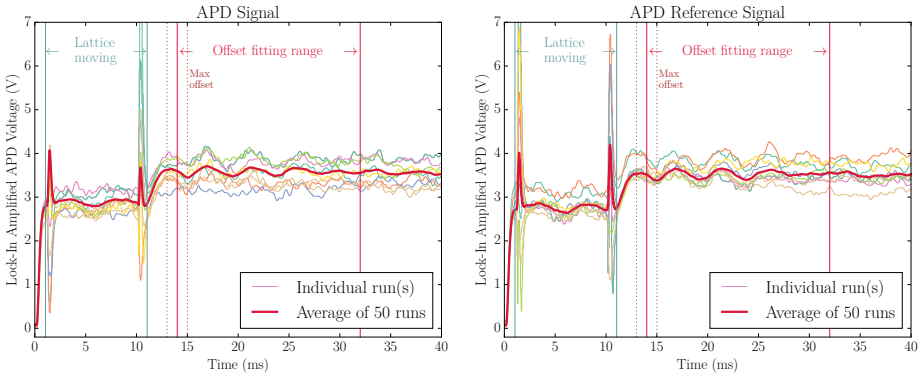

Figure 3.8 Transmission traces with (left) and without (right) atoms crashing onto the surface. The thick red line is the average of 50 runs, of which 10 are also shown in the figure. The lattice beams are on between the blue vertical lines and the lattice is moving. The periodic fluctuation on the signal is caused by mechanical vibrations inherent to the experimental cycle, changing the incoupling efficiency and the pinhole position. The offset fitting range is used in the procedure to make figure 3.9

3.4 Discussion

The dip in transmission due to interactions of the waveguide mode with the atoms could not be measured in this setup, even though calculations indicate that the effect should be strong enough to be measured. The following issues contribute to this.

Firstly, to avoid saturation, a very low power must be used and the outcoupling efficiency of 12% reduces this even further. A larger coupling efficiency

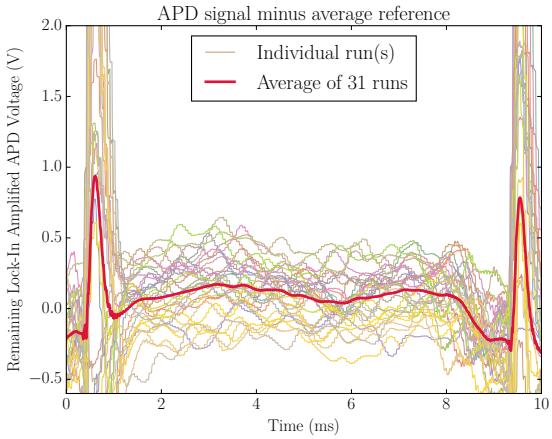

Figure 3.9 Result of post-process subtraction of the periodic fluctuations: shifted traces minus the average of the shifted traces of the reference signal. Shifts are determined by overlapping the signals between the red lines.

would still greatly enhance the visibility of the effect to be measured. Moreover, inspection of the gratings after a month of experiments revealed the gratings were damaged. The optical microscope image in figure 3.10 shows that the damage only appeared on the gratings on which experiments were performed. The experiment was repeated with a newly fabricated sample, but no significant changes in transmission were observed, which suggest that the observed damage was not the only reason the experiments were unsuccessful.

Secondly, mechanical noise induced by inherent mechanical vibrations of moving optical components cause systematic errors in the signal. The mechanical vibrations were reduced as much as possible, but could not be eliminated completely. Strongest vibrations originate from the rotating mirror of the moving dipole trap. If this element could be replaced with a rotation element with significantly lower moment of inertia, the problem could be overcome.

Thirdly, the problem of saturation and small probe powers could be circumvented by performing fluorescence measurements instead of absorption measurements. As fluorescence is a omnidirectional phenomenon and photons are emitted in all directions, a large numerical aperture would be desirable. In the current setup however, the numerical aperture is very small, because the first lens is placed outside the vacuum chamber, at 20 cm from the sample. In a setup with more direct optical access to the sample, fluorescence measurements would be feasible.

3.5 Conclusion

In the versatile atom transport apparatus for photonics, atoms are brought in contact with the evanescent field of a waveguided mode of a Si_3N_4 membrane

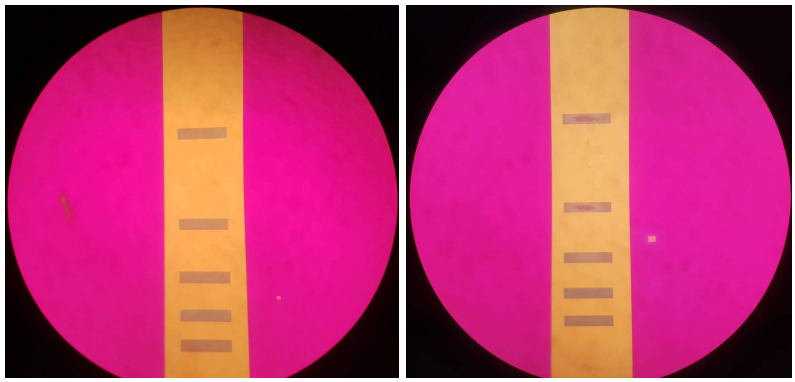

Figure 3.10 Optical microscope images of a membrane with clean gratings (left) and a membrane with damaged grating after performing experiments in the setup (right). Transmission experiments were only performed between the top two gratings.

sample. Improvements to the experimental setup enhanced the performance of the optical lift to an optimised atom flux $\sim 100\,\text{atoms}/\mu\text{s}$. The high atom flux gives us a significant advantage to measure the atom-light interaction. To avoid saturation of the atomic transition, optical power in the waveguide cannot exceed 120 pW. The setup is prepared to measure a small, few percent dip in the outcoupled transmission signal, which is only ~ 12 pW, with a photon counting module. The signal of the outcoupling is however distorted by fluctuations due to mechanical vibrations. The vibrations originate from the movement of the rotation stage of the optical dipole trap, which moves the atoms to sample position and is an indispensable part of the experimental cycle. Even after strong damping of the vibrations, the dip in transmission is still obscured by the fluctuations caused by the vibrations. A redesign of the setup with a rotation element with significantly lower moment of inertia, would enable the dip to be observed and the setup to be used for various other nanophotonic samples.

4

Light propagation and absorption in a dense rubidium vapour*

In this chapter we study non-linear absorption of intense monochromatic light through a dense rubidium vapour. The originally opaque vapour becomes transparent when illuminated with an intense laser beam. On-resonance transmission is measured through a 10 cm long heated vapour cell for atom densities up to $3 \times 10^{19}\,\mathrm{m}^{-3}$ and saturation parameters up to 10^4, for linear and circular polarisation. The strong absorption at low intensity is frustrated by an interplay of optical non-linearities (saturation and optical pumping) and non-linear effects due to the high atom density (collisional broadening and collisional depumping). To understand the results of the transmission measurements, we developed a model that incorporates these non-linear effects into the absorption. The model takes into account the absolute line strengths of all transitions from both hyperfine levels of the ground state of both isotopes of naturally abundant Rb. Doppler and collisional broadening are included in the Voigt profiles for the resonances. Being turned on one-by-one in the model, the non-linear processes reveal their effect on transmission curves. From comparison with experiments it is apparent that all non-linear effects are necessary for a quantitative agreement.

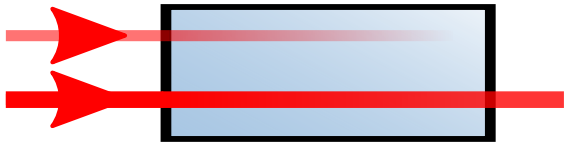

Figure 4.1 The basic concept of the experiment. A low intensity beam cannot penetrate the dense rubidium vapour, but the high intensity beam is transmitted.

*This chapter is based on the article *Combined effect of non-linear optical and collisional processes on absorption saturation in a dense rubidium vapour*, A.J. van Lange, P. van der Straten and D. van Oosten, *Journal of Physics B: Atomic, Molecular and Optical Physics* **53**(12) 125402 (2020).

4.1 Introduction

The study of optical properties of dense atomic vapours has resulted in the observation of fascinating non-linear effects on the propagation of light through such media [72]. An originally opaque dense vapour becomes transparent when excited with an intense control beam of laser light [39, 40]. This electromagnetically induced transparency (EIT) is performed in various schemes with resonant [73, 74] or off-resonant light [75, 76] and is applied in all-optical switching techniques [77–79]. An extreme way of controlling the propagation is in slow light experiments, in which the group velocity of the light is reduced by several orders of magnitudes compared to the speed of light in vacuum [41, 42]. In dense atomic vapours the velocity reduction has a broad bandwidth, making them suitable for slowing down picosecond pulses [80] and delaying nanosecond pulses by tens of pulse widths in a tunable all-optical delay line [81–83]. The dramatic reduction of speed to almost zero sparked research into storing light pulses in dense alkali vapours [43–47], which shows great promise in quantum network communication and synchronisation [48, 49].

In recent years, focus is on propagation through extremely dense vapours. In heated rubidium millicells, the transmission at low intensity was demonstrated to undergo collisional broadening [84, 85]. At frequencies below resonance and at high atomic densities, the propagation of the optical field was found to mimic the time evolution of a 2D-Bose gas with repulsive interactions [50, 51].

In the understanding of the effects of the experiments above, a proper description of the absorptive and refractive properties of the medium is pivotal. For specific ranges in intensity, atom density and detuning, these properties have been reported in earlier work: absorption has been studied at low laser intensities for high vapour densities [84, 86, 87], absorption with optical pumping at medium intensities [88–91], and absorption and refraction at high intensity and high atom density for large detunings [50, 92]. We capture these properties in a comprehensive model applicable over the whole range of detunings, saturation parameters and atomic densities. The principles of the model are applicable to any transition in an atomic vapour. This makes the model suitable for all of the above mentioned areas of research. We validate our model by comparing it to transmission measurements of a dense Rb vapour at high intensities close to resonance.

In this chapter, we first examine our experimental setup and the measured on-resonance transmission curves as a function of saturation parameters up to 2.5×10^4 for temperatures from 60 to 130 °C. These results inspire us to construct a model to calculate the transmission, which includes the following non-linear effects: collisional broadening, optical pumping to the dark ground state, collisional depumping and saturation. The influence of each of the effects on the resulting transmission curve becomes apparent and we conclude all effects are necessary to achieve quantitative agreement with the experimental results.

4.2 Experimental setup and transmission curves

The experimental setup to measure transmission through a heated rubidium cell is shown in figure 4.2. The 10 cm long vapour cell, containing rubidium with a natural isotope ratio (78.2% ^{85}Rb, 27.8% ^{87}Rb) with more than 98% purity, is wrapped with heating wires, isolated and placed in an aluminium heat shield. The temperature of the cell is controlled by the current through the wires and monitored by a thermocouple in direct contact with the cell wall.

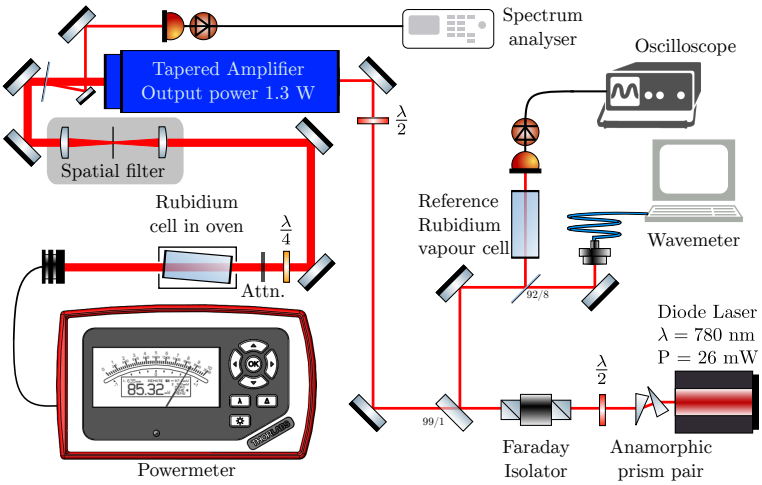

Figure 4.2 Schematic of the setup for high intensity and high density transmission measurements. Important components in the setup are the TuiOptics DL-100 light source, Toptica BoosTA Tapered amplifier, HighFinesse WS-6 wavemeter and the Rode & Schwarz FSL6 spectrum analyser.

Our light source is a continuous wave external cavity diode laser. An anamorphic prism pair ensures a circular beam and a 60dB Faraday isolator prevents unwanted reflections from destabilising the laser. Part of the light is split off by a beam splitter for characterisation of the laser frequency using a wavemeter and through a spectroscopy cell at room temperature for reference. The beam is amplified in a tapered amplifier (TA) to an output power of 1.3 W. Afterwards a small portion of the light is detected by a photodiode and analysed using an electronic spectrum analyser to ensure the diode laser has no multimode sidebands. Spatial filtering converts the elongated TA output mode into a Gaussian beam with a waist w_0 of 850 µm. At the entrance window of the heated cell the beam power is 500 mW, which can be attenuated to lower input powers P_{in} by absorptive neutral density filters just before cell entry. For circular polarisation measurements a quarter wave plate is placed in front of these attenuators. The transmission is collected and recorded by a power meter directly after the vapour cell.

The measured transmission for circular and linear polarisation at several cell

temperatures is shown in figure 4.3. The bare peak s_0 is determined by I_{peak}/I_s where $I_{\text{peak}} = 2P_{\text{in}}/(\pi w_0^2)$ and the saturation intensity I_s is 1.67 (2.50) mW/cm^2 for circular (linear) polarisation. The sudden rise from near-zero transmission to values clearly higher than a certain threshold value (in this chapter chosen as 0.01) suggests a saturation effect. At the highest experimental s_0 the transmission levels off to a value depending on the atom density. This suggests a non-linear effect in atom density.

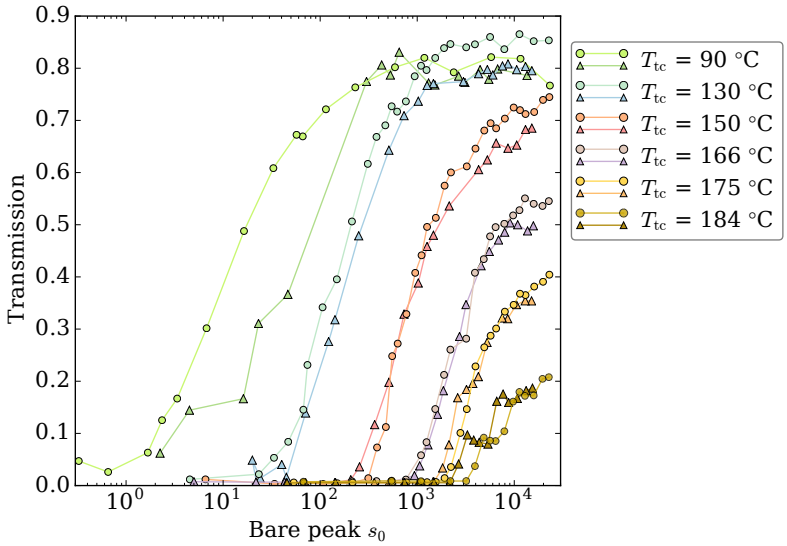

Figure 4.3 Transmission for circular (circles) and linear (triangle) polarisation for different cell temperatures. The bare peak saturation parameter is given by I_{peak}/I_s, where $I_{\text{peak}} = 2P_{\text{in}}/(\pi w_0^2)$ and I_s is 1.6 (2.5) mW/cm^2 for circular (linear) polarisation. Transmission is measured at $\omega = 384\,234\,576$ MHz (4170 MHz detuning in Table 4.1), the transition strength weighted average of the ^{87}Rb $F = 1 \rightarrow F' = 0, 1, 2$ manifold. Temperatures are measured by a thermocouple.

4.3 From wave equation to the Lambert-Beer law

For the propagation of the laser beam in our non-linear medium a general propagation equation is desirable. In this section, this equation is derived from the wave equation and seen to default to the Lambert-Beer law under the proper conditions. We thus relate two descriptions of light propagation in a homogeneous medium. On the one hand, light is an electromagnetic wave obeying Maxwell's equations, while on the other hand intensity of light is subject to the Lambert-Beer law for attenuation. Starting from Maxwell's equations, the *slowly varying paraxial approximation (SVPA)* and the *slowly varying envelope approximation (SVEA)* are applied to find the specific propagation equation for a light beam in

a homogeneous non-linear medium. When refraction is negligible this equation reduces to the Lambert-Beer law.

The wave equation for the electric field component of light, following from Maxwell's equations in a homogeneous medium is

$$\nabla^2\mathbf{E} - \frac{1}{c^2}\frac{\partial^2\mathbf{E}}{\partial t^2} = \mu_0\frac{\partial^2\mathbf{P}}{\partial t^2}, \tag{4.1}$$

where $\mathbf{E}$ is the electric field, $\mathbf{P}$ is the polarisation, and $c = \sqrt{\mu_0\varepsilon_0}$ is the speed of light in vacuum.

The polarisation response is assumed to be instantaneous and proportional to the electric field $\mathbf{P} = \varepsilon_0\chi\mathbf{E}$. The electric field is assumed to be periodic in time as $\mathbf{E} = \mathbf{A}\exp\{(-i\omega t)\}$, where ω is the laser frequency. Because the amplitude of the electric field varies slowly with respect to the laser frequency, the **slowly varying envelope approximation** is appropriate for $\mathbf{E}$ (and thus $\mathbf{P}$), stating

$$\frac{\partial\mathbf{A}}{\partial t} \ll \omega\mathbf{A} \quad \text{and} \quad \frac{\partial|\mathbf{P}|}{\partial t} \ll \omega\mathbf{P}, \tag{4.2}$$

which means

$$\frac{\partial^2\mathbf{E}}{\partial t^2} \simeq -\omega^2\mathbf{E} \quad \text{and} \quad \frac{\partial^2\mathbf{P}}{\partial t^2} \simeq -\omega^2\mathbf{P}. \tag{4.3}$$

The wave equation (Eqn 4.1) now becomes

$$\nabla^2\mathbf{E} + \frac{\omega^2}{c^2}\mathbf{E} = -\mu_0\omega^2\varepsilon_0\chi\mathbf{E}; \tag{4.4}$$

$$\nabla^2\mathbf{E} + \frac{\omega^2}{c^2}(1+\chi)\,\mathbf{E} = 0. \tag{4.5}$$

The z axis is chosen along the propagation direction and $\mathbf{P}$ is treated as a perturbation to $\mathbf{E}$ ($\chi \ll 1$), which is reasonable considering the values of χ at $T = 250\,^{\circ}\mathrm{C}$ [93]. For the unperturbed equation the solution then reads $\mathbf{E} = A\exp(-i(k_0 z + \omega t))$, where $k_0 = \omega/c$.

The equation is further simplified using the **slowly varying paraxial approximation** (SVPA), which states the amplitude change in the axial direction is small compared to the wave vector, $\partial A/\partial z \ll k_0$, such that

$$\frac{\partial^2\mathbf{E}}{\partial z^2} = \left(\frac{\partial^2 A}{\partial z^2} - 2ik_0\frac{\partial A}{\partial z} - k_0^2 A\right)\exp(-i(k_0 z + \omega t)); \tag{4.6}$$

$$\simeq \left(-2ik_0\frac{\partial A}{\partial z} - k_0^2 A\right)\exp(-i(k_0 z + \omega t)) \tag{4.7}$$

and thus

$$\nabla^2\mathbf{E} = \nabla_\perp^2\mathbf{E} + \frac{\partial^2\mathbf{E}}{\partial z^2} = \left(\nabla_\perp^2 A - 2ik_0\frac{\partial A}{\partial z} - k_0^2 A\right)\exp(-i(k_0 z + \omega t)). \tag{4.8}$$

We therefore find that the amplitude A obeys

$$\nabla_\perp^2 A^2 - 2ik_0 \frac{\partial A}{\partial z} + k_0^2 \chi A = 0, \tag{4.9}$$

where we used $k^2 = \omega^2/c^2$.

Taking the Fourier transformation of this equation and rearranging the terms yields the desired propagation equation for a beam propagating though a medium with susceptibility χ,

$$i\frac{\partial A}{\partial z} = \frac{\nabla_\perp^2}{2k_0} A - \frac{k_0}{2}\chi A, \tag{4.10}$$

which will hereafter simply be referred to as the propagation equation. Note that the susceptibility χ is in general still dependent on frequency ω and time averaged light intensity $I \propto |\mathbf{E}|^2 = |A|^2$.

Under our experimental conditions, the Gaussian beam is large, such that the diffraction term $(\nabla_\perp A)$ can be neglected. Furthermore, the measurements are performed on-resonance, such that the refraction term $\mathrm{Re}\{\chi(\omega)\} = 0$. With the intensity $I \propto |A|^2$, the propagation equation reduces to

$$\frac{\partial I}{\partial z} = -k_0 \,\mathrm{Im}\{\chi(\omega, I)\} I(\omega) \tag{4.11}$$

in which we recognise the Lambert Beer equation:

$$\frac{\partial I}{\partial z} = -\alpha I = -\sigma \varrho_{\mathrm{at}} I, \tag{4.12}$$

for $\alpha = \sigma \varrho_{\mathrm{at}} = k_0 \ \mathrm{Im}\{\chi(\omega, I)\}$.

4.4 Susceptibility of a dense Rubidium vapour

The susceptibility is the material property defining the behaviour of light in a medium, as can be seen in the propagation equation and the Lambert-Beer law. In this section the susceptibility is analysed in an atomic physics approach. The basis is a two-level system with saturation, yielding a power broadened Lorentzian lineshape. Collisions give rise to interaction broadening and the velocity distribution gives rise to Doppler broadening, transforming the Lorentzian line shape into a Voigt profile. When the level scheme of all the transitions in the Rb D_2 line is included in the model, optical pumping in between these levels becomes important.

4.4.1 Susceptibility of a two level system

In the simplest view of an atomic transition, the atom is a two level system with only a ground state g and an excited state e, with an energy difference of $\hbar\omega_{\mathrm{eg}}$.

Shining light onto the atom applies a coupling between the two states. The resulting Rabi two-level problem can be solved in a density matrix approach, that culminates in the optical Bloch equations (OBE)[19]. In this description the polarisability of an atomic vapour with density ϱ_{at} is given by

$$P = \varrho_{\mathrm{at}} p = \varrho_{\mathrm{at}}(\mu_{\mathrm{eg}}\varrho_{\mathrm{eg}} + c.c.), \tag{4.13}$$

where μ_{eg} is the electric dipole moment of the transition and ϱ_{eg} is the coupling term in the density matrix. In the steady state solution of the OBE this term is

$$\varrho_{\mathrm{eg}} = \frac{i\Omega}{2(\gamma/2 - i\delta)(1+s)}, \tag{4.14}$$

$$= i\frac{\mu_{\mathrm{eg}}|E|/\hbar}{(\gamma - 2i\delta)(1+s)}, \tag{4.15}$$

where $\Omega = |E|/\hbar$ is the Rabi frequency, γ is the decay rate of the excited state, $\delta = \omega_{\mathrm{laser}} - \omega_{\mathrm{eg}}$ is the detuning of the light with respect to the transition frequency ω_{eg}. The saturation parameter s is given by

$$s \equiv \frac{|\Omega|^2}{2|(\gamma/2 - i\delta)^2} \equiv \frac{s_0}{1 + (2\delta/\gamma)^2}, \tag{4.16}$$

where the on-resonance saturation parameter is defined as

$$s_0 \equiv 2|\Omega|^2/\gamma^2 = I/I_s, \tag{4.17}$$

with I_s the saturation intensity.

With this expression for the polarisation P, the susceptibility χ becomes

$$\chi \equiv \frac{P}{\varepsilon_0 E} = \frac{\varrho_{\mathrm{at}}\mu_{\mathrm{eg}}^2}{\varepsilon_0\hbar}\frac{2i}{(\gamma - 2i\delta)(1+s)} \tag{4.18}$$

$$= \frac{\varrho_{\mathrm{at}}\mu_{\mathrm{eg}}^2}{\varepsilon_0\hbar}\frac{2i}{\gamma}\frac{1 - i2\delta/\gamma}{1 + (2\delta/\gamma)^2 + s_0} \tag{4.19}$$

In the propagation equation (4.10) and the Lambert-Beer law (4.11), the important quantity is $k_0\chi$,

$$k_0\chi = \varrho_{\mathrm{at}}\frac{2k_0\mu_{\mathrm{eg}}^2}{\varepsilon_0\hbar\gamma}\frac{i - 2\delta/\gamma}{1 + (2\delta/\gamma)^2 + s_0} \tag{4.20}$$

$$= \varrho_{\mathrm{at}}\sigma_0\frac{\gamma_{\mathrm{nat}}}{\gamma}\frac{i - 2\delta/\gamma}{1 + (2\delta/\gamma)^2 + s_0}, \tag{4.21}$$

where we used $\sigma_0 = \frac{3\lambda^2}{2\pi} = \frac{6\pi}{k_0^2}$ and the definition of the unbroadened natural linewidth γ_{nat} for a two level system

$$\gamma_{\mathrm{nat}} = \frac{\mu_{\mathrm{eg}}^2\omega^3}{3\pi\varepsilon_0\hbar c^3} = \frac{\mu_{\mathrm{eg}}^2 k_0^3}{3\pi\varepsilon_0\hbar}, \tag{4.22}$$

such that

$$\sigma_0\gamma_{\rm nat} = \frac{6\pi}{k_0^2}\frac{\mu_{\rm eg}^2 k_0^3}{3\pi\varepsilon_0\hbar} = \frac{2k_0\mu_{\rm eg}^2}{\varepsilon_0\hbar}. \tag{4.23}$$

With this expression for the susceptibility, the propagation equation takes the form

$$\frac{\partial A}{\partial z} = \left[i\frac{\nabla_\perp^2}{2k_0} - i\varrho_{at}\ \frac{1}{2}\sigma_0\ \frac{2\left(\delta/\gamma\right) - i}{1 + \left(2\delta/\gamma\right)^2 + I/I_s}\right] A. \tag{4.24}$$

In the remainder of this chapter we consider absorption near resonance, where the refraction term $(\nabla_\perp^2 A)$ is negligible. In the next chapter the refraction term is reintroduced, when the detuning is shifted away from resonance. For now, we only take into account the real part of the right-hand side of the equation

$$\frac{\partial A}{\partial z} = -\varrho_{at}\ \frac{1}{2}\sigma_0\ \frac{1}{1 + \left(2\delta/\gamma\right)^2 + s_0} A. \tag{4.25}$$

To recover the Lambert Beer equation, we again look at $I = |A|^2$ and find

$$\frac{\partial I}{\partial z} = \frac{\partial |A|^2}{\partial z} = 2A\frac{\partial A}{\partial z} = -\varrho_{\rm at}\ \sigma_0\ \frac{1}{1 + \left(2\delta/\gamma\right)^2 + s_0} I, \tag{4.26}$$

where, on resonance and at low intensity, the cross section is indeed $\sigma \equiv \sigma_0 = \frac{3\lambda^2}{2\pi} = \frac{6\pi}{k_0^2}$. For detuning δ and saturation parameter s_0, this cross section σ_0 is multiplied by the Lorentzian lineshape $L(\delta, s_0)$

$$L(\delta, s_0) = \frac{1}{1 + \left(2\delta/\gamma\right)^2 + s_0}. \tag{4.27}$$

4.4.2 Interaction broadening

In dense atomic vapours, the changes in local environment due to the high density cause a broadening of the linewidth. This is a mean-field effect caused by the average of one atom's surroundings and is therefore a homogeneous effect, affecting the lifetime of the atom. The interaction of the atom with (the mean field of) the other atoms broadens line with a value proportional to the density of atoms. Depending on the field of research, the effect is often called collisional broadening, where the interactions are assumed to be collisions, or pressure broadening, named after the cause of the density increase.

The broadening of the natural linewidth $\gamma_{\rm nat}$ is experimentally determined to be

$$\gamma = \gamma_{\rm nat} + \beta\varrho_{\rm at}, \tag{4.28}$$

where for the rubidium D_2 line, the natural linewidth $\gamma_0 = 6.06\,\mathrm{MHz}$ and $\beta = (1.10 \pm 0.17) \times 10^{-19}\,\mathrm{m^3MHz}$ [85, 94]. The interaction also gives rise to a Lorentz-Lorenz shift in the transition resonances and even an additional collisional shift, but these shifts have negligible effects on the transmission at resonance [95].

Effect on the saturation parameter

The broadening by interactions also affects the saturation parameter, as can be readily seen from its definition

$$s_0 \equiv 2|\Omega|^2/\gamma^2 = I/I_s. \tag{4.17}$$

The bare s_0, determined directly from the intensity measurements, thus needs to be adjusted by

$$s_0 = s_{0,\mathrm{bare}} \frac{\gamma^2}{\gamma_{\mathrm{nat}}^2}, \tag{4.29}$$

in the dense rubidium vapour.

4.4.3 Doppler broadening

At the elevated temperatures in our experiment and even at room temperature, the atoms in the vapour cell are far from stationary and their velocity distribution gives rise to Doppler broadening of the resonances. The effective detuning of the laser depends on the velocity of the atom, because of the Doppler effect. The Lorentz line shape $L(\delta(v), s_0)$ therefore needs to be convoluted with the Doppler profile $D(v, T)$, which results in a Voigt profile $V(\delta, s_0, T)$

$$V(\delta, s_0, T) = \int_{-\infty}^{\infty} dv D(v, T) L(s_0, \delta). \tag{4.30}$$

The Voigt profile is required, because at high intensities power broadening makes the broadened Lorentz width comparable to the Doppler width and the Voigt profile thus ensures validity over a large range of detunings: from far above to far below the Doppler width (figure 4.4). In the convolution only the axial velocity distribution needs to be taken into account, because the velocity distributions in different directions are decoupled. The Doppler integral for the Voigt profile is thus

$$V(\delta, s_0) = \frac{1}{\sqrt{2\pi} v_{\mathrm{th}}} \int_{-\infty}^{\infty} dv\, e^{-\frac{1}{2}\frac{v^2}{v_{\mathrm{th}}^2}} \frac{1}{1 + (2\delta(v)/\gamma)^2 + s_0}, \tag{4.31}$$

where $v_{\mathrm{th}} = \sqrt{k_B T/m}$, γ is the linewidth of the transition and the detuning δ is dependent on the atom velocity v as $\delta = \delta_0 - v/\lambda$, with δ_0 the original detuning of the excitation and λ the transition wavelength.

The Voigt profiles are obtained using the real part of the Faddeeva function $w(z)$ [72] as follows

$$V(\delta_0, s_0; v_{\text{th}}, \gamma) = \int_{-\infty}^{\infty} dv' \frac{\frac{1}{\sqrt{2\pi}v_{\text{th}}} e^{-\frac{1}{2}\frac{v^2}{v_{\text{th}}^2}}}{1 + \left(2(\delta - v/\lambda)/\gamma\right)^2 + s_0} \tag{4.32}$$

$$= \frac{\pi\gamma}{2\sqrt{1+s_0}} \frac{\lambda}{\sqrt{2\pi}v_{\text{th}}} \text{Re}\{w(z)\}, \tag{4.33}$$

where

$$z = \frac{\delta_0 + i\gamma\sqrt{1+s_0}/2}{\sqrt{2}v_{\text{th}}/\lambda}. \tag{4.34}$$

In appendix B the full susceptibility with Voigt profiles is rewritten in terms of the Faddeeva function. To illustrate the relation between the Doppler, (power-broadened) Lorentz and Voigt profiles we show the interesting and relevant characteristics in Figure 4.4.

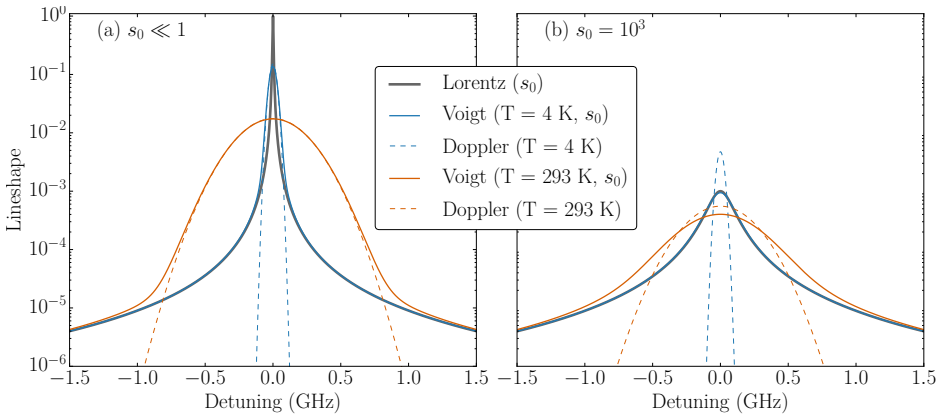

Figure 4.4 Lorentz, Doppler and Voigt profiles for a single resonance line for (a) low saturation ($s_0 \ll 1$) and (b) high saturation ($s_0 = 10^3$). The Doppler widths for $T = 4$ K and $T = 293$ K given by $\delta_{\text{th}} = v_{\text{th}}/\lambda$ are 25 and 215 MHz. The Doppler profiles are scaled with $\pi\gamma/(2\sqrt{1+s_0})$ for proper comparison with the Voigt profiles. (a) At low saturation the Voigt profile resembles the Doppler profile at low detuning $|\delta| \leq 4\delta_{\text{th}}$ and the Lorentz profile at high detuning. The Voigt profile is required for calculation over the full range of detuning. (b) At high saturation the power broadened Lorentz width becomes comparable to the Doppler width at room temperature and the Voigt profile is the only accurate description over a large range of detunings.

4.4.4 Rubidium energy levels

To determine the total absorption coefficient α we have to take into account all allowed transitions that make up the Rb D_2 line [87]. The vapour consists of

a natural mixture of ^{85}Rb (72.2%) and ^{87}Rb (27.8%). Figure 4.5 shows hyperfine structure around the D_2 line for ^{87}Rb with arrows depicting the allowed transitions. For the correct transition frequencies of the D_2 line transitions, we calculate the hyperfine frequency shifts for the ground state and the excited state of both isotopes [19, 96].

Table 4.1 shows the resulting frequencies for all transitions from $F_g = i$ to $F_e = j$ in the D_2 manifold. The frequencies ω_0^{ij} are listed with respect to the excitation frequency of ^{85}Rb, as determined without hyperfine splitting. There we also list the transition strength coefficients R^{ij} with respect to the cycling transition. The absorption coefficient α is calculated by summing over all the allowed transitions as

$$\alpha(\omega, I) = \frac{3\lambda^2}{2\pi} \sum_{\text{isotopes}} \sum_{i} \sum_{j=i-1}^{i+1} \varrho_i R^{ij} V(\omega - \omega_0^{ij}, s_0^{ij}), \tag{4.35}$$

where $\frac{3\lambda^2}{2\pi}$ is the light-atom scattering cross-section for a two-level system, λ is the transition wavelength, ϱ_i is the density of atoms in ground state i, and $s_0^{ij} = R^{ij} I / I_s$ is the transition specific saturation parameter with I_s the saturation intensity for the cycling transition.

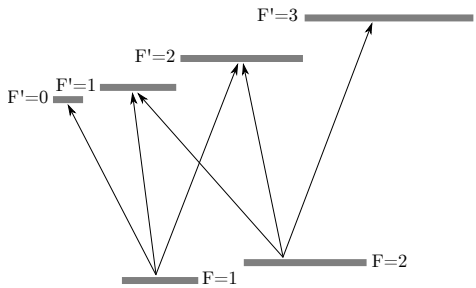

Figure 4.5 Schematic representation of contributing transitions of the ^{87}Rb D_2 lines.

To show the influence of all the individual lines, figure 4.6 shows a measured transmission spectrum at room temperature and low intensity, the fit to this spectrum and the contributions of the fit of all the individual transition lines. Since the intensity and thus s_0 is low, the fit function is $I = e^{-\alpha l}$, where l is the length of the cell and α is as defined in equation 4.35.

4.5 Temperature and density calibration

The response of the medium to a beam of light with intensity I and frequency ω thus only depends on two parameters: the temperature and the density. To eliminate one of the parameters, the density is expressed as a function of temperature

F_g (=i)	F_e (=j)	$\omega_0^{ij} - \omega_0$ (MHz)	R^{ij}
^{85}Rb	1	-1378.06875	0
$F_g = 3$	2	-1348.75475	$\frac{10}{27}$
	3	-1285.37375	$\frac{35}{27}$
	4	-1164.63375	$\frac{81}{27}$
^{85}Rb	1	1657.66125	1
$F_g = 2$	2	1686.97525	$\frac{35}{27}$
	3	1750.35625	$\frac{28}{27}$
	4	1871.09625	0

F_g (=i)	F_e (=j)	$\omega_0^{ij} - \omega_0$ (MHz)	R^{ij}
^{87}Rb	0	-2787.4225	0
$F_g = 2$	1	-2715.0995	$\frac{1}{6}$
	2	-2557.9295	$\frac{5}{6}$
	3	-2290.8745	$\frac{14}{6}$
^{87}Rb	0	4047.2575	$\frac{2}{6}$
$F_g = 1$	1	4119.5825	$\frac{5}{6}$
	2	4276.7525	$\frac{5}{6}$
	3	4543.8075	0

Table 4.1 Transition frequencies and transition strengths for the D_2-lines of rubidium. Frequencies are listed with respect to the excitation frequency without hyperfine splitting of ^{85}Rb (384 230 406.373 MHz). Transition strengths with respect to the cycling frequency transition strength.

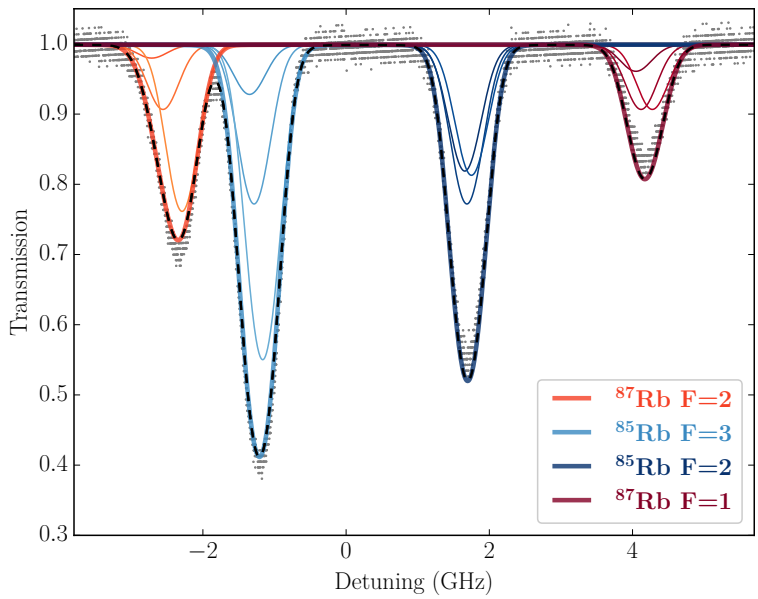

Figure 4.6 Contributions of the individual transition lines in the D_2 manifold to the fit. Experimental data (dots) is taken at room temperature and low intensity. The fit (dashed line) is built up of contributions from ^{85}Rb (blue) and ^{87}Rb (red). The thin lines are the individual transitions of table 4.1, thick lines are the contributions summed per ground state.

for a pure rubidium gas by

$$\varrho_{\mathrm{at}}(T) = \frac{p}{\mathrm{k_B} T}, \qquad \text{with} \quad \log_{10}(p) = 5.0057 + 4.312 - 4040/T, \tag{4.36}$$

where p is the vapour pressure and k_B is the Boltzmann constant [97]. We measure the temperature on a particular part of the cell wall, but the atoms in the vapour cell thermalise to the coldest point of the cell. Therefore we perform a calibration to relate the equilibrium temperature of the atoms to the measured temperature of the cell wall.

To calibrate the atom temperature in the vapour cell, we measure the transmission spectra of a low intensity beam and fit the spectra using the model above (figure 4.8). The setup for these low intensity experiments is slightly different and is shown in Figure 4.7. After the first beam splitter the light is sent directly through the heated cell without amplification and transmission signals from the heated cell are recorded on an oscilloscope together with the transmission signal from the reference cell. In this experiment the laser frequency is varied by modulating the current through the laser diode. Intensity changes due to this modulation are compensated for by fitting the background slope of the reference signal to second order in detuning.

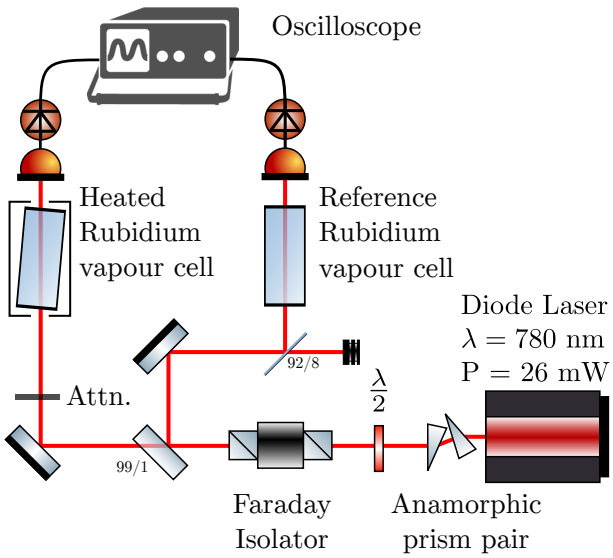

Figure 4.7 Setup for the temperature and density calibration at low intensity. The laser frequency is scanned over the resonances by modulating the current through the laser diode. The transmission through the heated cell and through a reference cell are recorded simultaneously, which allows laser intensity changes to be compensated and the spectral span to be properly calibrated.

As the transmission in a dense rubidium vapour is zero for large parts of the spectrum around the resonances, the frequency axis is calibrated by fitting the reference signal with our calculation model as a function of temperature. The result for room temperature measurements in figure 4.8 shows a good fit

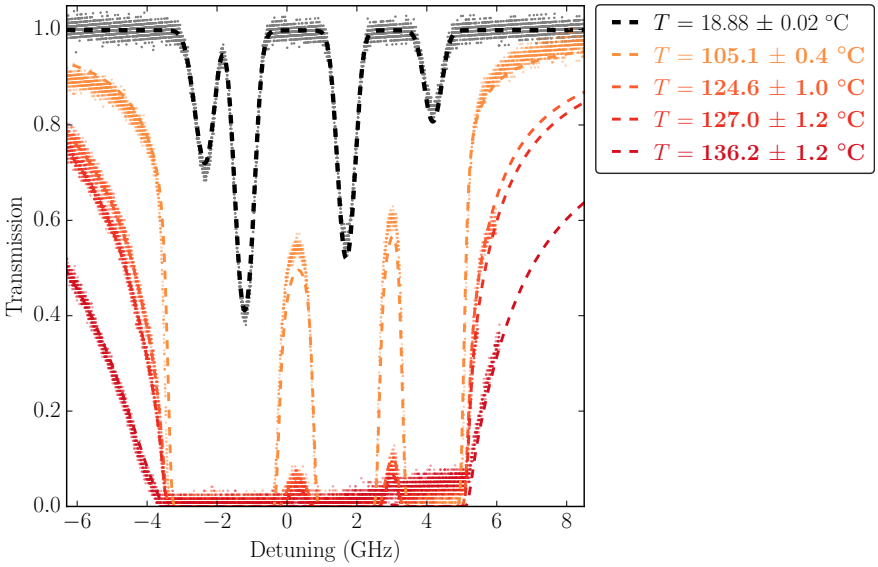

Figure 4.8 Measured transmission spectra for cell temperatures of 166 to 202 °C (coloured dots). The reference spectrum at room temperature (grey dots) is fitted with Doppler (blue line) and Voigt profile (black dashed) and determines the frequency-axis for the high temperature spectra. Coloured dashed lines are the Voigt fits for the corresponding higher temperature measurements.

with a temperature of 18.9 °C. The fit procedure was confirmed to produce a spectrum, indiscernible from the fit with pure Doppler profiles, which is equally appropriate for low intensity and a fitting range within a few Doppler widths of the resonances. We also verified the fit function by reproducing the spectral fits of transmission through high density vapours in millicells [98].

At higher temperatures the transmission is zero over a large range around the resonances. The parts of the spectrum useful for fitting are therefore located in the wings, where only the Voigt-profiles are valid. The fits in figure 4.8 show good agreement with the data. The table shows the relation between the temperature obtained from the spectral fit (T_{sp}) and the temperature measured by the thermocouple (T_{tc}). We use a linear fit to assign a spectral temperature to all the temperatures at which the transmission is measured in figure 4.3 and find the relation

$$T_{\mathrm{sp}} = (5.9 \pm 4.6)\,^{\circ}\mathrm{C} + (0.636 \pm 0.028)\ T_{\mathrm{tc}}. \tag{4.37}$$

This equation provides a good working value for the spectral temperature to calculate the transmission for high density and high temperature conditions of our measurements, despite the uncertainty in the relation.

(a)

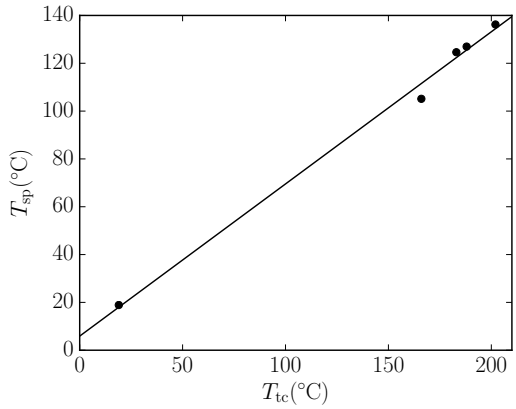

(b)

T_{tc} (°C)	T_{sp} (°C)	$\varrho_{at}(T)$ ($\times 10^{19}$m^{-3})
166	105.7 ± 0.4	0.82 ± 0.02
183	124.6 ± 1.0	2.62 ± 0.15
188	127.0 ± 1.2	2.89 ± 0.20
202	136.2 ± 1.2	4.93 ± 0.31
		($\times 10^{15}$m^{-3})
19	18.88 ± 0.02	6.56 ± 0.01

Figure 4.9 (a) Fit (solid line) of the spectrum temperature to the thermocouple temperature given by equation 4.37. Data points (dots) are the the spectrum temperatures from the fit of figure 4.8, listed in (b) along with the resulting densities.

4.6 Saturation and optical pumping

Even though the above model includes saturation and power broadening, it is not yet suitable to use at high intensities, where optical pumping comes into play. In optical pumping a fraction of the atoms is pumped into an optical dark state, leaving fewer atoms available for excitation in the bright state. The effect is most prominent when pumping is on resonance with the transitions from a particular ground hyperfine state. The strong laser beam pumps atoms from the resonant, bright hyperfine ground state to the excited state, from which they have a possibility of falling into the other, dark hyperfine ground state. For the on-resonance behaviour studied in this chapter, the detuning is set to the average of the ^{87}Rb $F = 1 \rightarrow F' = 0, 1, 2$ manifold.

The process of optical pumping is depicted in the Jablonski diagram in figure 4.10(a) for ^{87}Rb and can be described by Einstein rate equations. The pumping rate from ground state i to the combined excited level e is given by

$$\Gamma_{ie} = \frac{2\pi\gamma}{2} \sum_j V(\delta^{ij}, s_0^{ij}), \tag{4.38}$$

where $\delta^{ij} = \omega - \omega^{ij}$. The chance to fall back into the lower (upper) hyperfine ground state is given by the branching ratio br_{ei}, 1/2 (1/2) for ^{85}Rb and 4/9 (5/9) for ^{87}Rb [19].

Since we work at high atomic densities, collisions occur frequently. The collisional depumping rates Γ_{12} and Γ_{21}, which redistribute the population over the ground states, therefore need to be included. The rates are not equal because of a difference in multiplicity m_i and are given by $\Gamma_{12} = \Gamma_{\mathrm{col}} \frac{m_2}{m_1+m_2}$ and $\Gamma_{21} = \Gamma_{\mathrm{col}} \frac{m_1}{m_1+m_2}$. Here we have introduced the collision rate $\Gamma_{\mathrm{col}} = \varrho_{\mathrm{at}} v_{\mathrm{col}} \sigma_{\mathrm{col}}$,

where $v_{\mathrm{col}} = 2\,v_{\mathrm{th}}$ is the most probable interatomic speed and σ_{col} is the collisional cross section.

Collision rates and collisional cross sections specifically are notoriously difficult to determine and inherently specific for the process under investigation. Collision rates have been determined for ultracold Rb atoms in magnetic and magneto-optical traps [99] and spin relaxation and excitation-transfer collisions between Rb and buffer gases [100, 101], but not for the hyperfine ground state changing collision of concern here. To estimate this specific cross section we determine the relevant impact parameter by calculating the minimum distance between atoms for which the energy exchange exceeds the hyperfine splitting of the ^{87}Rb ground state. This is the largest energy difference to be overcome for a hyperfine state change, which can therefore occur during a collision between any two atoms. The energy transfer for a given impact parameter depends on the type of interaction involved in the collision. The collision between identical atoms is described by a Van der Waals potential C_6/R^6, for which the C_6 coefficient of Rb is 4.47×10^3 in atomic units [102, 103]. The estimate for the impact parameter b in this case is 1.43 nm and the collisional cross section is $\sigma_6 = \pi b^2 = 6.42\,\mathrm{nm}^2$, which is of the same order of magnitude as the total elastic scattering cross section $Q = 23.6\,\mathrm{nm}^2$ [99]. Dipole-dipole-type collisions, with Van de Waals potential C_3/R^3, between excited and ground state can be neglected, because the occupation of the excited state is severely reduced by optical pumping up to saturation parameters in the order of 10^5, when the power broadening becomes of the order of the ground state hyperfine splitting.

We solve the Einstein rate equations for the above values and find the populations of the ground states of both isotopes shown in figure 4.10(b). The population of the bright ground state reduces strongly when the pumping laser is on resonance with this bright state. We also notice this effect in the transmission spectra. The drop in bright state population strongly enhances the transmission.

The populations we find are the ingredient for a final adjustment of our treatment of saturation. The transition-specific saturation parameter depends on the occupation of the excited state in question. At high intensities, the contribution to the excitation from the other ground state cannot be neglected anymore, as due to power broadening their absorption overlaps significantly. The transition-specific s_0^{ij} will therefore also include a contribution from the other ground state, which we write formally as a sum over all other ground states as

$$s_0^{ij} = s_0 R^{ij} + s_0 \sum_{k \neq i} R^{kj} \frac{\varrho_k}{\varrho_i} \frac{1}{1 + (2\delta^{kj}/\gamma^{kj})^2}, \tag{4.39}$$

where $\gamma^{kj} = \gamma\sqrt{1 + R^{kj} s_0}$ is the transition specific power broadened linewidth. With the saturation parameters s_0^{ij} dependent on the populations ϱ_i, and the populations dependent on the saturation parameter, the model needs to calculate these quantities in an iterative procedure, for which convergence in our model is reached after 3 iterations.

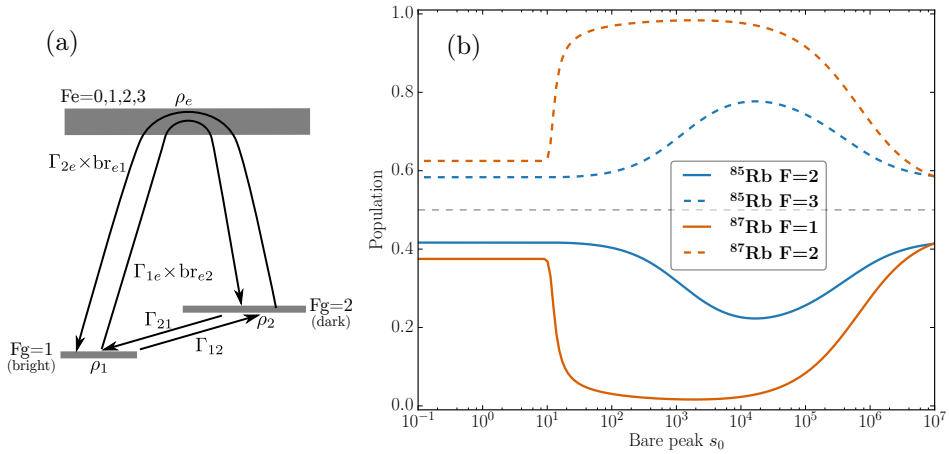

Figure 4.10 (a) Schematic energy diagram for the optical pumping mechanism for ^{87}Rb. The bright and dark state refer specifically to the case of pumping on resonance with the ^{87}Rb $F_g = 1$ state, as used in the experiment and in calculations in (b). (b) Steady state population of the ground states for pumping on resonance with the ^{87}Rb $F_g = 1$ state as function of s_0. Above $s_0 \simeq 10$ optical pumping becomes larger than collisional depumping and the population of the bright ground state is depleted severely.

4.7 Transmission at resonance

The interplay of all the non-linear processes described above has a particularly intriguing effect on the transmission at resonance. We apply our model to the transmission at the ^{87}Rb $F = 1 \rightarrow F' = 0, 1, 2$ transition over a wide range of saturation parameters s_0 for one typical temperature (111 °C). To accurately describe the experimental conditions, we simulate the propagation of a Gaussian beam by discretising the Gaussian in 20 regions and propagating these regions in parallel in 10 steps. For comparison with experimentally obtained transmission, we compensate for losses from passing the windows of the cell by a factor of $\sqrt{0.85}$ at each window. This factor is chosen to match the measured transmission of 85% far off-resonance at δ=20 GHz. To illustrate the influence of the separate non-linear effects, we turn the effects on one-by-one, as shown in figure 4.11.

We start with the curve taking into account only saturation (solid line). The threshold at which transmission becomes larger than 0.01 is at $s_0 \simeq 10^5$, far from the experimentally observed value of $\simeq 10^3$, and the curve has no intermediate plateau. With the introduction of optical pumping (dashed-dotted line) a plateau appears for $s_0 < 10^5$, caused by the near depletion of the bright state. As there are no collisions to repopulate the bright state, the bright state is only repopulated by the reverse optical pumping from the dark state, which is much weaker because it is much further detuned. In the steady state solution the population of the bright state is therefore only a few percent (see figure 4.10(b)),

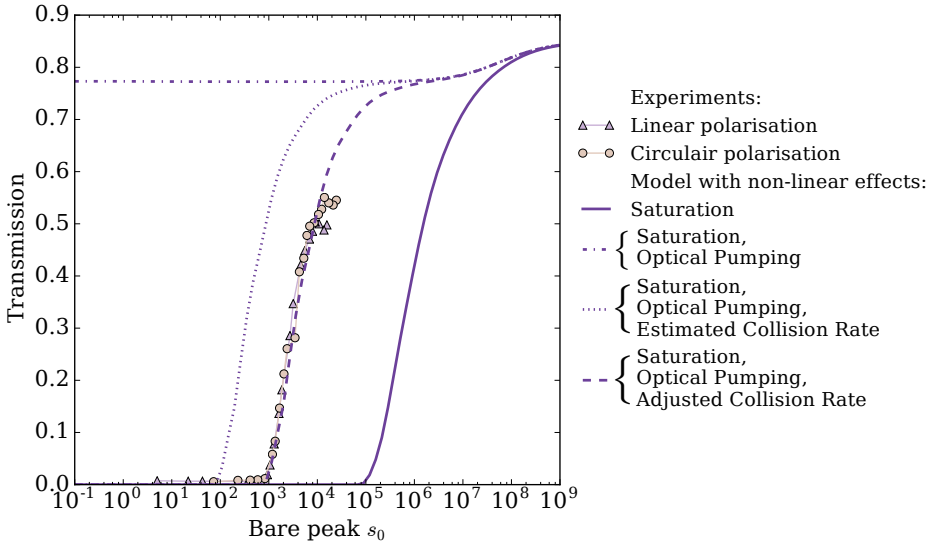

Figure 4.11 Transmission measurements at $T_{\mathrm{tc}} = 166\,^{\circ}\mathrm{C}$ and calculation at $T_{\mathrm{at}} = 111\,^{\circ}\mathrm{C}$ (from Eq. 4.37). In the plots the non-linear effects are turned on one-by-one. With only saturation turned on (solid line) the threshold s_0, where transmission becomes larger than 0.01, is too high. With the introduction of optical pumping (dash-dotted line) an the atom density dependent plateau appears and transmission does not approach zero for low s_0. Addition of collisions to the model introduces a new theshold s_0 for transmission larger than 0.01 , which is too low for the estimated collisional cross section of 6.4 nm^2. With a collision rate of 67 nm^2, adjusted to fit our measurements, the model (dashed line) shows the correct threshold value of $s_0 \simeq 10^3$. This collisional cross section is chosen to match the calculations to all experiments in figure 4.12 simultaneously.

which is nevertheless responsible for significant absorption. As this fraction of the atom density is stable for all s_0 (up to $s_0 \sim 10^5$), the amount of absorption and thus the level of transmission is determined by the atom density. The height of this plateau is therefore dependent on the atom density, in accordance with experimental observations.

With the introduction of collisions into our model (dotted line) the curve resembles the shape of the measurement data, as the effect of optical pumping is suppressed by collisional depumping for $\Gamma_{21} > \Gamma_{1e}\mathrm{br}_{e2}$. This criterion determines the threshold, where the transmission becomes larger than 0.01. For the collisional rate estimated above, this occurs at $s_0 \sim 20$, which is not in agreement with the experiments. We therefore adjust the collision rate through the estimated collisional cross section such that the model matches all of our measurements simultaneously.

The collisional cross section is an intrinsic property of the Rb vapour and independent on the atom density and temperature, for the range of temperatures

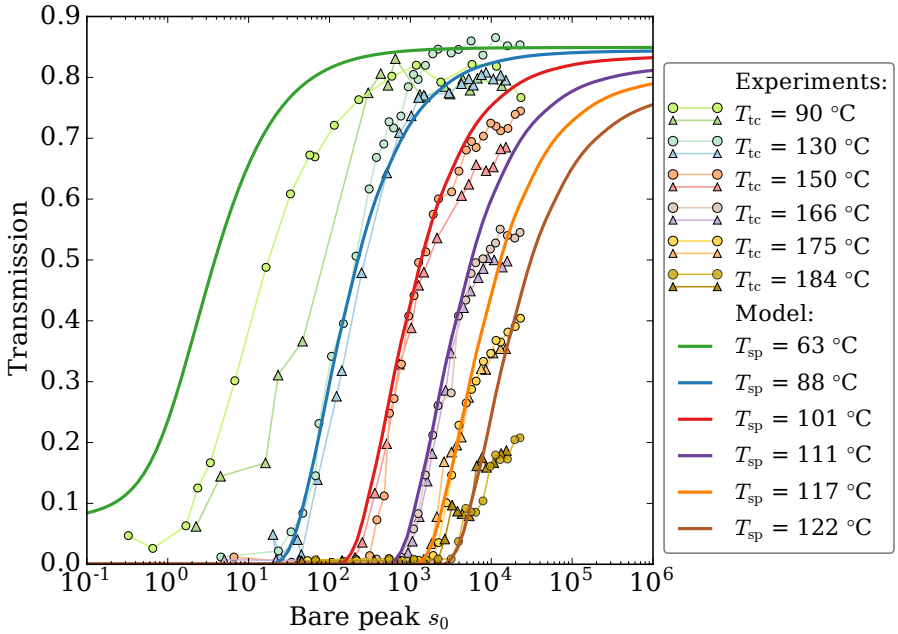

Figure 4.12 Transmission for circular (circles) and linear (triangle) polarisation for different cell temperatures. Transmission is measured at $\omega = 384\,234\,576$ MHz, which is 4170 MHz detuning in Table 4.1, the weighted average of the ^{87}Rb $F = 1 \rightarrow F' = 0, 1, 2$ manifold. Temperatures measured by the thermocouple T_{tc} and the corresponding temperatures T_{sp} from absorption spectrum analysis (Eq. 4.37) are used as input temperature for the model calculations (solid lines). The collisional cross section is set to $\sigma_{col} = 67$ nm^2.

that we have explored. The optimum value for the cross section is therefore best recovered by simultaneously matching our model to *all* of the measurements in figure 4.3, using a single value of the cross section as the only free parameter, for the temperature relation in equation 4.37. The resulting curves are judged on retrieval of the correct curve slopes and the correct thresholds for the value of s_0 at which transmission first exceeds the threshold value of 0.01. The results of this procedure are shown in figures 4.11 and 4.12 for an optimum value of $\sigma_{col} = 67\,\text{nm}^2$. In particular the correct slope for different temperatures and the correct threshold values for s_0 are captured. Note that this should not be interpreted as a measurement of σ_{col}, as the uncertainty in the coefficients of the temperature calibration leads to a large uncertainty in σ_{col}. The lower bound of the temperature yields an optimum for $\sigma_{col} = 322\,\text{nm}^2$, whereas the upper bound gives $\sigma_{col} = 19\,\text{nm}^2$. Since we are here concerned with the resulting optical properties, more accurate knowledge of T_{sp} and thus σ_{col} is not required.

The model only deviates from the measurement at $T_{tc} = 90\,°\text{C}$, at which the spectral temperature is more uncertain, as it is far away from the calibration

points (19, 166, 183, 188 and 202 °C) for the temperature fit of equation 4.37. But more importantly, at these intermediate temperatures the optical pumping scheme of figure 4.10, which neglects magnetic sublevels and hyperfine states of the excited state, might be an oversimplification. This notion is supported by the difference in behaviour for different polarisations, which is expected to occur when more subtle pumping effects including magnetic sublevels of the ground and excited states become important. For higher temperatures the model accurately describes the non-linear transmission through a dense rubidium vapour for $s_0 < 10^4$.

4.8 Conclusion

We developed a model to describe the absorption of a continuous light source in a dense rubidium vapour at high intensity. The model includes non-linear effects in intensity (optical pumping and saturation) and atomic density (collisional broadening and collisional depumping). The principles of the model are applicable to any transition in an atomic vapour. The model is particularly straightforward to transfer to the D_2 line of another alkali metal, as only values of the atomic properties need to be adjusted. We compare the results of our model to measurements of transmission through a 10 cm cell containing a dense vapour of a natural isotope mixture of rubidium. The transmission for light resonant with the highest line in the Rb D_2 manifold shows good agreement for saturation parameters $s_0 < 10^4$ and temperatures $90\,°\mathrm{C} < T_{\mathrm{sp}} < 130\,°\mathrm{C}$, when we assume a collisional cross section of $\sigma_{\mathrm{col}} = 67\ \mathrm{nm}^2$. We show that all the non-linear effects included in the model are essential to explain the characteristics of the transmission curves.

5

Beam shape modification due to the non-linear optical response in a dense rubidium vapour

Dense rubidium vapours have the ability to change beam profiles by virtue of their non-linear properties. A Gaussian input beam profile can emerge from a 10 cm long heated rubidium cell in peculiar and characteristic shapes, such as Airy-like patterns, a ring and even a traffic light shape. These characteristic beam profiles occur at well defined detuning for given input intensity and cell temperature. In our experiment, we track the detuning at which each of these shapes occur as a function of intensity by determining the maximal structural similarity (SSIM). We establish a detuning curve as a function of intensity for each shape at two cell temperatures. The detuning curves correspond remarkably well to striking features in transmission spectra obtained over the same intensity range, indicating an elevated transmission for these characteristic shapes. After proper scaling the detuning curves all collapse onto one universal dimensionless detuning curve. This suggest all shapes are manifestations of the same underlying phenomenon. The observed behaviour alludes to spontaneous formation of soliton-like modes in the dense rubidium vapour.

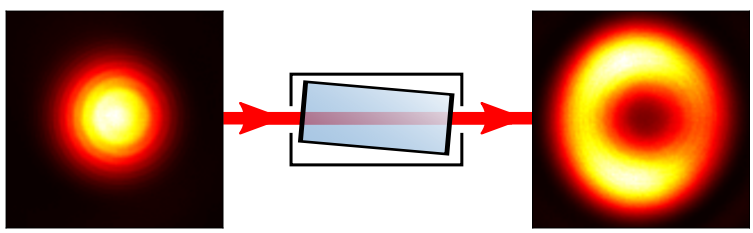

Figure 5.1 The basic concept of the experiment: the incoming laser beam profile has changed shape after propagation through a dense rubidium vapour.

5.1 Introduction

Dense rubidium vapours have recently regained interest for their ability to affect the statistics and shapes of a laser beam. Below the transition frequency, i.e. at negative detuning with respect to the atomic resonance, defocusing causes intriguing effects in beam statistics: a disorganised speckle pattern regains coherence gradually due to the defocusing nonlinearity [50] and the beam profile evolution in the cell is found to be analogous to the time-evolution of a 2D-Bose gas [51, 104].

Above the transition frequency, i.e. at positive detuning with respect to the atomic resonance, beams with extraordinary shapes have been observed emerging from a dense rubidium vapour. Already in the 80s, rubidium vapours were found to have a self-focusing effect on blue detuned laser beams due to saturated absorption [105]. More recently, Gaussian beams of nearly resonant light, focused strongly in the non-linear medium have produced Bessel-Gauss modes, which have self-reconstructing properties upon hitting an obstacle [53]. Under slightly different conditions cross-phase modulation produces size-variable Dark-Hollow Beams (DHB): optical modes with a bright ring around a dark centre [52]. The size of the rings is dependent on the vapour temperature and the laser beam intensity. The DHB can be turned into a self-healing Bessel beam by focusing.

In this chapter, we report on transmission experiments performed with high laser intensity and at high atomic densities. Various characteristic shapes are observed emerging from the dense rubidium vapour cell, shown in figure 5.2. These shapes appear at a different detuning for each beam intensity and temperature, are very robust, easily reproducible and highly similar for different detuning-intensity-temperature combinations. We track the detuning at which the characteristic shapes appear over a range of intensities and we relate this to striking features in transmission spectra measured over the same intensity range. To investigate whether these characteristic shapes and the features in the transmission are a result of a common physical phenomenon, we collapse the detuning curves of the characteristic shapes onto one universal dimensionless detuning curve.

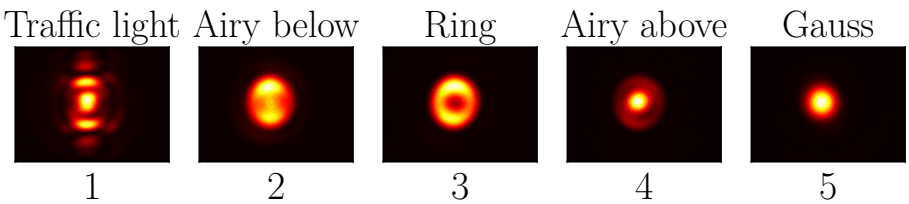

Figure 5.2 Characteristic shapes emerging from the dense rubidium vapour. These five shapes are tracked through detuning-intensity space in section 5.4.

5.2 Setup

The setup for the experiments in this chapter is an adapted version of the setup used in the previous chapter. Figure 5.3 shows the configuration, in which the emerging beams are detected by two cameras recording a real space image and Fourier image of the exit window of the heated cell containing a dense rubidium vapour. The Fourier image is measured in a 2f configuration in the following way. Output light is deflected by a 92%:8% pellicle beam splitter and collected by a 2 inch lens positioned at a focal length distance, $d = f = 100\,\text{mm}$. At a focal length distance from the lens, a camera is placed to record the image. The real space image is measured with a two lens imaging system with the Fourier lens as the first lens. After this lens, light is split by a 50%:50% pellicle beam splitter and the reflected light is collected by a tube lens, which is at a focal length away from the second camera to record the image. At high beam powers, attenuators are placed in front of the Fourier image camera and in front of the real space image tube lens.

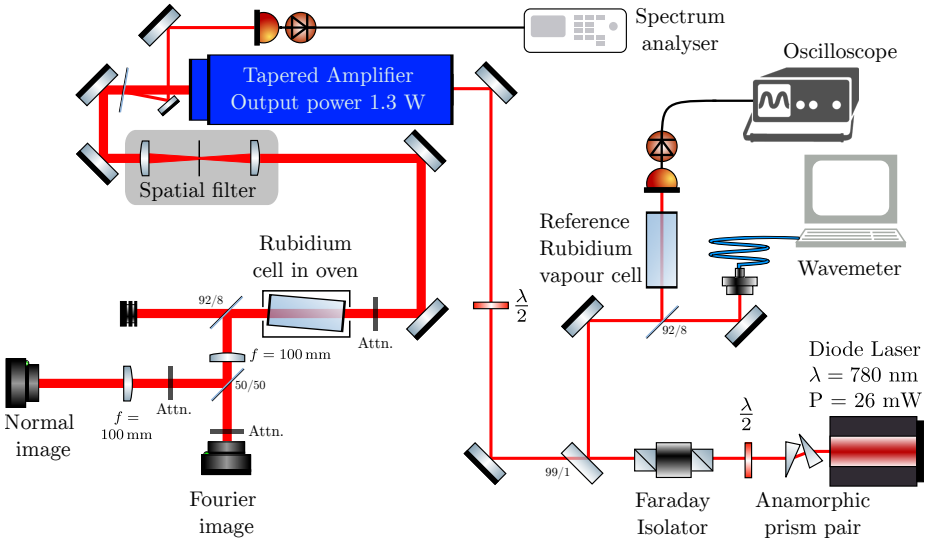

Figure 5.3 The setup to record the normal, real space image and the Fourier image of the output beam-profile after propagation through a dense rubidium vapour. From the diode laser light source, the beam passes through a prism pair and isolator. Laser frequency is determined by a wavemeter and a reference rubidium cell. Beam power is amplified by a tapered amplifier, spatially filtered and attenuated to the desired power. The rubidium is in an oven, consisting of a heat shield with isolation and heating wires. The exit window of the cell is imaged by a two lens imaging system and Fourier imaged in a 2f-configuration. Key components in the setup are the TuiOptics DL-100 light source, Toptica BoosTA Tapered amplifier, HighFinesse WS-6 wavemeter, the Rohde & Schwarz FSL6 spectrum analyser and two Point Grey Chameleon cameras.

5.3 A map of beam profiles in detuning and intensity

To get an initial sense of the kind of shapes emerging from the cell at different conditions, the real space images of the beam profiles are displayed on a grid of intensity and detuning in figure 5.4. The beam profiles are measured at equidistant steps in detuning and for different beam powers, determined by the available attenuator strengths. In the resulting array of pictures, two remarkable features catch the eye: self-focusing and ring formation.

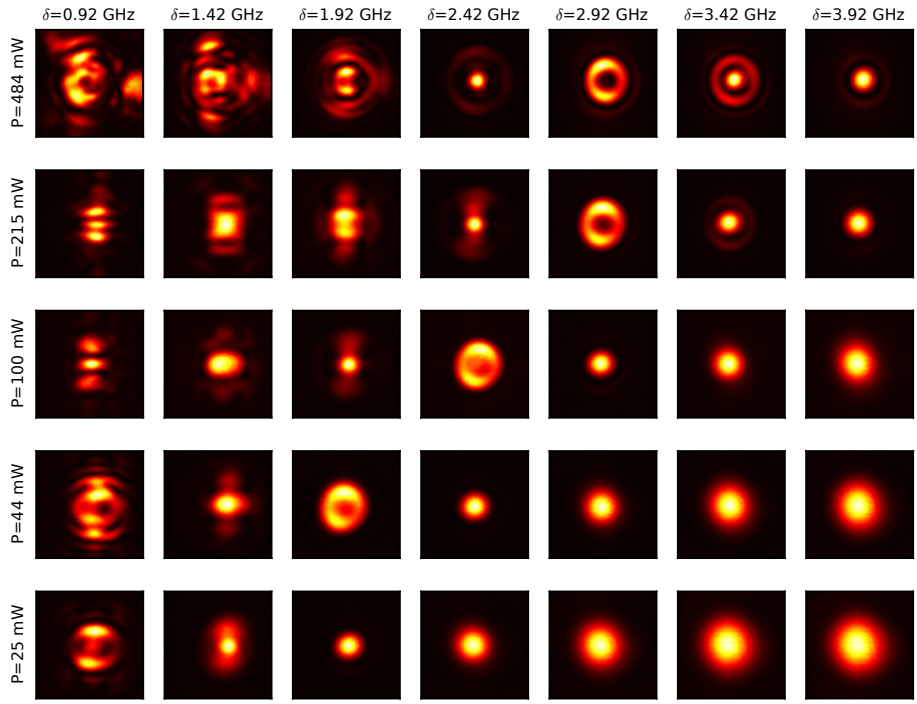

Figure 5.4 Emerging beam profiles on a power-detuning grid. The characteristic shapes appear along certain lines in this plot. The detunings are determined with respect to the average of the ^{87}Rb $F = 1 \rightarrow F' = 0, 1, 2$ manifold (384.234 58 THz). The power range corresponds to a peak s_0 of the Gaussian beam of 1.3×10^3 to 2.6×10^4.

Far above the resonance the profile has a Gaussian shape, which is unaltered from the incoming beam. When the resonance is approached from above, the width of the profile first becomes smaller and smaller, but the profile still resembles a Gaussian. This effect is clearly visible in the bottom two rows, where the beam diameter shrinks to roughly half the original size. For higher power the effect takes place outside the range of this figure. The effect is attributed

to the self-focusing of the beam in the dense rubidium vapour. In the dense rubidium vapour the refractive index depends on the intensity $I = P/(\pi w_0^2)$, and consequently on the saturation parameter $s_0 = I/I_s$ of the beam profile, where $I_s = 2.50\ \mathrm{mW/cm^2}$ is the saturation intensity. Figure 5.5 shows the absorption lineshape and the refractive index of a single resonance for several saturation parameters s_0 in a rubidium vapour at $T_{\mathrm{tc}} \simeq 175\,^{\circ}\mathrm{C}$, which corresponds to a density $\varrho_{\mathrm{at}} \simeq 2 \times 10^{19}\,\mathrm{m^{-3}}$ (through equations 4.36 and 4.37). Above the resonance the refractive index becomes larger with increasing intensity and the non-linearity is thus positive. As light is refracted towards the region with a higher refractive index, the beam is focused by its own beam profile.

The second eye-catching feature is the appearance of a ring shaped profile at several positions on the grid. Interestingly, these positions seem to be on a line with a specific relation between detuning and intensity. To uncover the relation we track the detuning of this shape (and others) over the whole intensity range in the following section.

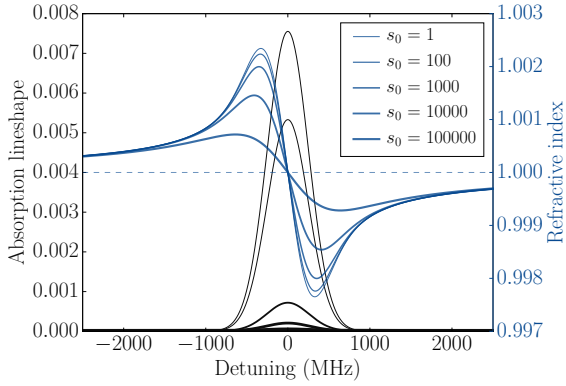

Figure 5.5 Absorption lineshape (grey) and refractive index (red) for a single resonance at several saturation parameters $s_0 = I/I_s$. The parameters for the profile are those for a rubidium vapour at $T_{\mathrm{tc}} \simeq 175\,^{\circ}\mathrm{C}$, for which $\varrho_{\mathrm{at}} \simeq 2 \times 10^{19}\,\mathrm{m^{-3}}$ (through equations 4.36 and 4.37). Above the resonance, increasing s_0 increases the refractive index and the non-linearity has a positive sign.

5.4 Tracking shapes through the detuning–saturation parameter plane

In this section, we track the detuning at which the characteristic shapes of figure 5.2 occur as a function of saturation parameter $s_0 = I/I_s$. For each s_0, we vary the detuning to find the profile that is most similar to the characteristic shape. We carry out this experiment at two different cell temperatures. Similar-

ity to the reference image is determined by the structural similarity index*(SSIM) of two images [106]. By definition, the SSIM index ranges from -1 to 1, where 1 indicates perfect similarity between identical images, 0 indicates all structural similarity between the images is lost and negative values indicate the image structure is inverted. The image is allowed to undergo affine transformations while determining the optimum SSIM value, such as displacement, scaling, shearing and rotation. We have chosen to optimise the SSIM value rather than to minimise the mean squared error, because SSIM deals better with noise, local disturbances and offsets [107, 108].

The characteristic shapes from figure 5.2, numbered from 1 to 5, are used as reference signal for the shape tracking. The optimum in SSIM between the reference image and the image at a different input power P_{in} is determined while varying the laser frequency, which results in a detuning curve $\delta_i(s_0)$ for each shape i. The resulting detuning curves $\delta_i(s_0)$ are shown in figure 5.6, where the bare peak s_0 is determined by I_{peak}/I_s, where $I_{\text{peak}} = 2P_{\text{in}}/(\pi w_0^2)$. The SSIM values we find for optimum similarity range from 1 at the reference image to a minimum of 0.7, which still indicates a high level of similarity. Importantly, the SSIM value has a clear maximum in detuning at each s_0, making the method well suited for the tracking of specific shapes. In all the experiments, the amount of affine transformation was small, as is readily confirmed by visual inspection of the transformed images.

All detuning curves δ_i in figure 5.6a depend on s_0 in a similar fashion: starting from a non-zero value of $\delta \simeq 1$ GHz, a very sharp initial increase is steadily converted to a gentle increase until it levels out at $s_0 > 1.5 \times 10^4$ to a final value $\delta_{i,\text{fin}}$ between 3 and 7 GHz. The curves for different temperatures are best compared on a logarithmic scale in figure 5.6b. The curves show similar behaviour for both temperatures, but with a different amplitude. The amplitude ratio is estimated from the values of $\delta_{i,\text{fin}}$ of both temperatures. For each of the shapes i, the ratio is calculated to yield an average of 1.63 ± 0.03. As temperature change mainly has effect through the density $\varrho(T)$, this ratio is compared to the density ratio between the two temperatures, which gives 3.19 and is a factor 2 higher. In search for other effects that depend on the density (and thus temperature), we find the ratio only corresponds well to the s_0 renormalisation in equation 4.29 of $\left(\frac{\gamma(\varrho_1)}{\gamma(\varrho_2)}\right)^2 = 1.64$, but the physical mechanism to connect this renormalisation to the detuning curves is not directly obvious and measurements at more temperatures are required to better understand this factor.

*We use the python implementation `structural_similarity` from the `skimage.metrics` package.

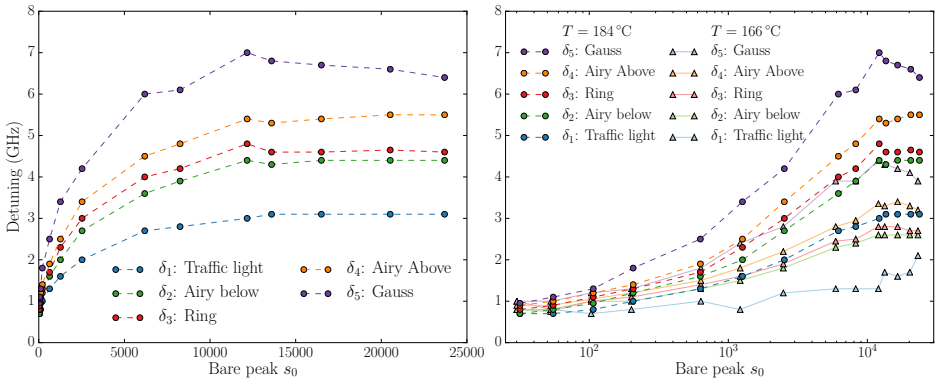

Figure 5.6 Tracking of characteristic beam profiles. (a) Detuning curve δ_i for the five characteristic beam profiles as function of s_0 on a linear scale for $T_{\mathrm{tc}} = 184\,°\mathrm{C}$ and (b) on a logarithmic scale for $T_{\mathrm{tc}} = 166\,°\mathrm{C}$ and $T_{\mathrm{tc}} = 184\,°\mathrm{C}$.

5.5 Transmission spectra and characteristic beam shapes

The formation of characteristic shapes is also expected to have an effect on the transmission. Due to their sharp intensity profile, the characteristic shapes will lead to a stronger saturation effect and therefore to an enhanced transmission. Transmission is measured over the whole detuning-intensity grid for $T_{\mathrm{tc}} = 164\,°\mathrm{C}$ and $T_{\mathrm{tc}} = 186\,°\mathrm{C}$ and shown in figure 5.7. Each row represents a full spectrum taken at the power specified on the vertical axis, such that the bottom rows of both graphs are equivalent to the profiles for $T_{\mathrm{tc}} = 166\,°\mathrm{C}$ and $T_{\mathrm{tc}} = 184\,°\mathrm{C}$ of figure 4.8. The transmission in these experiments is determined from the sum of all pixel counts on the camera and normalised to 1 for far off resonance transmission. Blue dashed lines indicate the centre resonance frequencies of the D_2 lines of ^{85}Rb and ^{87}Rb per hyperfine ground state.

For $T_{\mathrm{tc}} = 164\,°\mathrm{C}$, the spectra remain very similar for low $s_0 < 50$, but change severely for high $s_0 > 500$. Considering the spectrum as a whole, the region of low transmission becomes wider for increasing s_0 and the spectrum develops an asymmetry for increasing s_0. This asymmetry is also visible for the individual lines and is most profound in the resonance with the highest frequency. Around this transition and for $50 < s_0 < 500$, the width of the zero transmission region is decreasing from the right (above the transition), but stays the same on the left. Above $s_0 = 500$, the zero transmission region persists only below the transition, while above the transition the most striking behaviour takes place: lines of alternating low and high transmission branch off from the original spectrum. The intriguing consequence of this is that for these intensities the spectrum has extra structure with maxima and minima in a region without *any* atomic transitions to cause such effects. For $T_{\mathrm{tc}} = 186\,°\mathrm{C}$ the branching off is even clearer, with

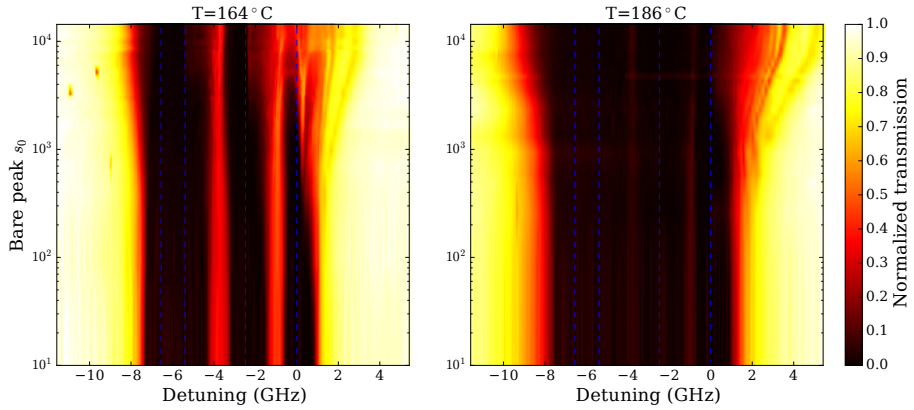

Figure 5.7 Total transmission as a function of detuning and power for 164 °C (left) and 186 °C (right). The transmission in these experiments is determined from the sum of pixel counts on the camera and normalised to 1 for far off resonance transmission. Blue dashed lines indicate the centre resonance frequencies of the D_2 lines of ^{85}Rb and ^{87}Rb per hyperfine ground state.

branches splitting off more vigorously and remaining clearly visible as they reach higher final detunings.

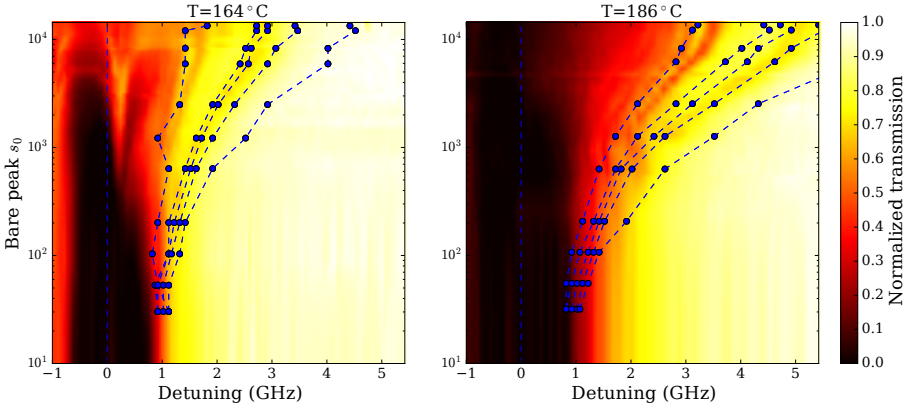

Figure 5.8 A zoom in of figure 5.7 around the highest resonance with the (transposed) detuning curves $\delta_i(s_0)$ for characteristic shapes (blue dots) displayed in the same figure. Transmission measurements are taken at 164 °C (left) and 186 °C (right), characteristic shapes are tracked at comparable temperatures of 166 °C (left) and 184 °C (right). The curves for characteristic shapes follow the same type of trajectory as the high transmission between low transmission lines branching off.

The behaviour of these typical features in the transmission shows remarkable resemblance to the detuning curves $\delta_i(s_0)$ resulting from the tracking of characteristic shapes. To illustrate this resemblance we transpose the trajectories of

characteristic profiles and plot them on top of a zoomed-in version of the transmission data in figure 5.8. The detuning curves of characteristic shapes have the same shape as the branches in the transmission spectra, where the detuning curves follow regions of enhanced transmission. This remarkable correlation between the detuning curves and high transmission branches, strongly suggest they find their origin in the same underlying phenomenon.

5.6 Influence of the input wavefront shape

To investigate the sensitivity of the output ring profile to the input wavefront of the beam, we deliberately change the input wavefront and compare the output for the ring shaped profile. In our experiment, the ring radius is remarkably constant for all positions on the detuning curve, while earlier reports show a ring diameter decreasing with input power [52, 53]. However, in those cases the initial beam was focused, whereas in the experiment discussed here, the Gaussian beam is prepared with the least possible curvature of the wavefront. As wavefront curvature appears to be an important parameter in the former experiments, we investigate the influence of changes to the initial beam profile shape and wavefront curvature on the emerging profiles.

The input wavefronts of the smooth Gaussian input beam are modified by several optical elements. In figure 5.9, the effects of the manipulations of the incoming beam on the emerging profiles are shown. The following optical elements are placed in front of the heated cell: a beam rotator in several orientations to rotate the beam by 0°, 90° and 180°, positive and negative lenses. Also the diaphragm after spatial filtering is further opened and closed. The detuning is adjusted to relocate the ring shaped profile.

In all these cases, a beam profile with similar radial profile is recovered. In the cases with the rotator (figure 5.9b, c and d) the ring remains clearly visible, but the regions of elevated intensity on the ring are rotated. In these cases the detuning only requires minor adjustments. The aperture of the diaphragm at the end of the spatial filter (figure 5.9g and h) has little influence on the emerging pattern. The detuning is adjusted to compensate for the loss (gain) of intensity due to the further closed (opened) diaphragm.

In the cases of a positive and especially a negative lens (figure 5.9e and f), the detuning must be adjusted considerably in order to recover a ring shaped profile. The whole sequence of beam profiles (row in figure 5.4) is shifted to higher detunings for the positive lens, which is interpreted as the lens accounting for the first part of the self-focusing. For the negative lens, the opposite effect takes place, extra self-focusing is required and the sequence is shifted to lower detunings. For the positive lens a dark hollow profile is recovered at higher detuning, but for the negative lens case, a spot in the centre of the ring remains, because the pattern breaks apart before the spot completely disappears. However, the onset of the ring is still clearly visible.

In conclusion, with all of the above distortions of the wavefront, the character-

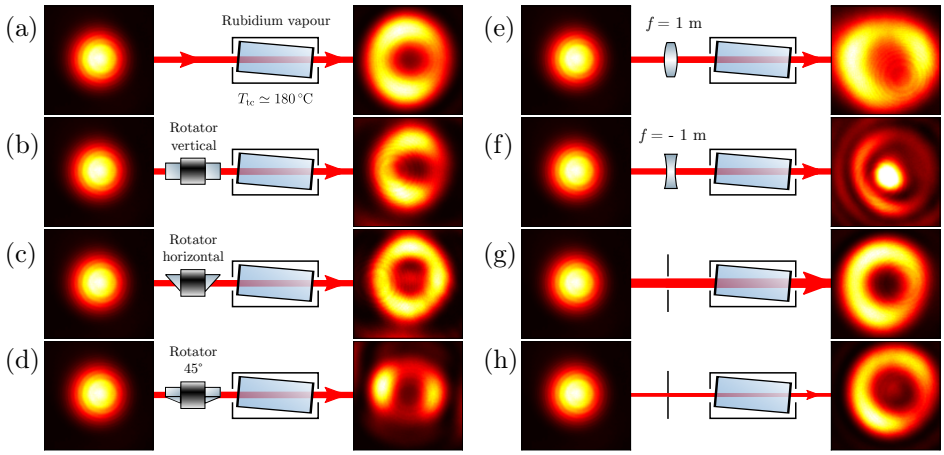

Figure 5.9 The robustness of the output ring under distortion of the incoming wavefront by the following optical elements: (a) undistorted reference case ($P = 44\,\mathrm{mW}$, $\delta = 1.6\,\mathrm{GHz}$ or $P = 200\,\mathrm{mW}$, $\delta = 7.0\,\mathrm{GHz}$), (b) beam rotator in vertical orientation ($P = 44\,\mathrm{mW}$, $\delta = 1.8\,\mathrm{GHz}$) , (c) beam rotator in horizontal orientation ($P = 34\,\mathrm{mW}$, $\delta = 1.5\,\mathrm{GHz}$), (d) beam rotator under 45° ($P = 37\,\mathrm{mW}$, $\delta = 1.4\,\mathrm{GHz}$), (e) positive lens ($P = 200\,\mathrm{mW}$, $\delta = 6.4\,\mathrm{GHz}$), (f) negative lens ($P = 200\,\mathrm{mW}$, $\delta = 1.0\,\mathrm{GHz}$), (g) diaphragm after spatial filtering completely opened ($P = 223\,\mathrm{mW}$, $\delta = 7.3\,\mathrm{GHz}$), (h) and closed to half the beam diameter ($P = 130\,\mathrm{mW}$, $\delta = 6.3\,\mathrm{GHz}$).

istic shapes still emerge from the heated rubidium cell. Lenses shift the detuning at which the shape is formed, but do not affect the vapour's ability to form these shapes. Therefore, the formation of the profiles is not due to a specific input wavefront, but the result of non-linear behaviour in the dense rubidium vapour.

5.7 A universal detuning curve

The detuning curves $\delta_i(s_0)$ all depend on s_0 in a very similar way and the spacing between the curves scales with the detuning. This behaviour suggests there is a universal $\delta - -s_0$ relation for profiles in the medium, of which the individual δ_i's are a special case. To unveil this universal behaviour, the curves are collapsed onto the same line by the following procedure. An offset of δ_{offset} is applied to all δ_i's, which are subsequently divided by their final value for high s_0 (corrected for δ_{offset}), yielding a normalised dimensionless detuning of

$$\bar{\delta}_i(s_0) = \frac{\delta_i(s_0) - \delta_{\mathrm{offset}}}{\delta_{i,\mathrm{fin}} - \delta_{\mathrm{offset}}}, \tag{5.1}$$

where $\delta_{i,\mathrm{fin}}$ is determined by the average of the last three data points in the curves for $\delta_i(s_0)$. For all δ_i's this gives similar $\bar{\delta}_i$ curves, for which we can make the collapse complete by determining the correct offset. Only the curve $\delta_1(166\,°\mathrm{C})$ is itself too erratic to produce a reasonable $\bar{\delta}_1$ curve. It is therefore discarded in

the analysis to determine the universal detuning curve. The optimum of offset $\delta_{\text{offset}} = 850\,\text{MHz}$ is determined by minimising the sum of standard deviations of $\bar{\delta}_i$'s per s_0.

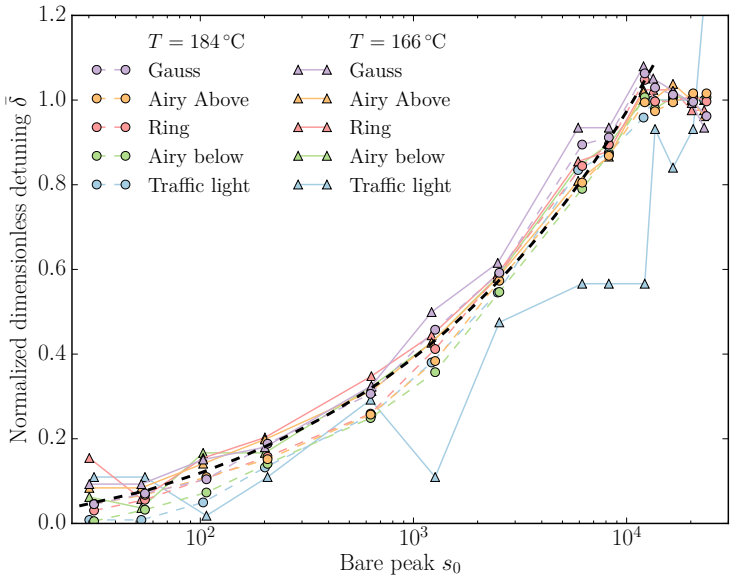

Figure 5.10 The collapse of the detuning curves on the universal dimensionless detuning curve $\bar{\delta}$, which is given by equation 5.1. The black dashed line is the fit for $\bar{\delta} = a + b\ {s_0}^c$, with $a = -0.12 \pm 0.3$, $b = 0.05 \pm 0.01$ and $c = 0.33 \pm 0.02$.

Figure 5.10 shows this collapse procedure to be very effective for all $\bar{\delta}_i$ (except $\bar{\delta}_1(166\,°\text{C})$). A universal detuning behaviour $\bar{\delta}(s_0)$ is clearly visible. With this universal detuning curve, a full detuning curve of any characteristic beam shape can be recovered from just its final detuning $\delta_{i,\text{fin}}$, using the inverse of equation 5.1. The rising part of the universal detuning curve, for $s_0 < 10^4$, can be captured in a fit function $\bar{\delta}(s_0) = a + b\ {s_0}^c$, with $a = -0.12 \pm 0.3$, $b = 0.05 \pm 0.01$ and $c = 0.33 \pm 0.02$. The universal curve for dimensionless detuning thus appears to be propotional to $\sqrt[3]{s_0}$ for $s_0 < 10^4$. This is curious, as one would perhaps rather expect a relationship to power broadening, which goes as $\sqrt{1 + s_0}$.

5.8 Conclusion and outlook

In our experiments we observe stable, robust optical profiles, spontaneously formed from a Gaussian input profile by non-linear effects in dense rubidium vapours at a high saturation parameter. These profiles occur at very specific combinations of the saturation parameter and detuning, which we captured in

detuning curves $\delta_i(s_0)$ for each shape i for a given temperature. The detuning curves are directly linked to high transmission regions in transmission spectra measured over the same range of saturation parameters. All the detuning curves collapse onto a universal dimensionless detuning curve, which indicates that the shapes are manifestations of the same phenomenon. These beam shapes have a sharp intensity profile, and therefore have increased transmissions due to stronger saturation of the vapour.

The above behaviour is consistent with the formation of spatial soliton-like modes. In such modes a balance is found between the inward directed refraction (self-focusing) and the outward directed divergence, or in terms of the propagation equation (4.10) the defocusing diffraction term $\propto \nabla_\perp^2 A(\omega)$ is balanced by the focusing refractive term $\propto \mathrm{Re}\left\{\chi(\omega, A^2)\right\} A(\omega)$. This can result in highly stable modes, which propagate without changing shape. A pure soliton also maintains its energy and thus amplitude, but in practice damping will come into play. To check whether the characteristic shapes indeed correspond to solitons, experiments with several cell lengths should be performed.

A second and arguably more elegant experimental approach involves the detection of the full electric field of the profile with off-axis holography. This method enables the measurement of both the amplitude and the phase profile of the emerging beam, instead of just the intensity. This method can be combined with wavefront shaping of the input beam with a spatial light modulator (SLM). The measured output field can be recreated by the SLM and used as the input for the next cycle of propagation through the cell. Thereby the profile can effectively be propagated over a large number of cell lengths and the evolution can be monitored at every step, such that the profile evolution can be studied at regular steps 'inside' the medium.

Alternatively, simulations of beam propagation with all non-linear effects can be used. Numerical implementation of the propagation equation with the full expression for the susceptibility χ is, however, far from trivial, especially considering the effects of optical pumping discussed in the previous chapter. In the full description, $\chi = \sum_{i,j} \varrho_i \sigma_0 \tilde{V}(\delta_{ij}, s_0^{ij}, T)$, where $\tilde{V}(\delta, s_0, T)$ from equation B.10 in appendix B and the saturation s_0^{ij} is given by equation 4.39. In simulations using a time splitting spectral method method and a simplified expression for χ, rings did emerge from the cell, but qualitative agreement could not be obtained.

Besides more experimental and numerical work, the results cry out for theoretical work to understand the common behaviour of the detuning curves. The experimental results in this chapter supply clear constraints to which such a theory should adhere, such as the dependence of the dimensionless detuning curve on s_0 and the dependence of the scaling on the temperature. The questions that remain to be answered are: On what principle does the scaling of individual detuning curves rely? Can we construct a theory that retrieves the universal dimensionless detuning curve? And what is the 'order parameter', that defines the characteristic shapes with high transmission? In short, our results pose a clear challenge for further experimental and theoretical research.

A

Effective index of the fundamental mode in the waveguide

For the design of our surface grating coupler we need to know the effective index of our waveguide mode. In this appendix we calculate the effective index for the fundamental TE and TM mode of the grating layer. These are the only modes available in our 220-nm thin layer of Si_3N_4 surrounded by air.

The effective indices follow from solving the Maxwell's equation for appropriate boundary conditions for TE and TM modes. For our symmetric layered system we follow the derivation of Burke [67], and solve the final equation numerically rather than graphically. This numerical treatment allows us expand the solving power to asymmetric systems, e.g. waveguide layers with different materials on the top and bottom.

First we describe the method to solve the fundamental TE and TM modes in a symmetric system, which we will then adapt to also make it suitable for asymmetric systems.

A.1 The symmetric case

In the symmetric case a waveguide is constructed by the following layered medium. A layer of thickness h and index n_{layer} surrounded by an infinite layer of index n_{cover} on both sides, with $n_{\text{layer}} > n_{\text{cover}}$. We use the symmetry of the system and choose $x = 0$ as the center of the waveguide layer. The example below shows a silicon nitride waveguide in air:

$$n = \begin{cases} n_{\text{core}} = n_{\text{Si}_3\text{N}_4} & \text{if} \quad |x| \leq h/2 \\ n_{\text{cover}} = n_{\text{air}} & \text{if} \quad |x| > h/2 \end{cases} \tag{A.1}$$

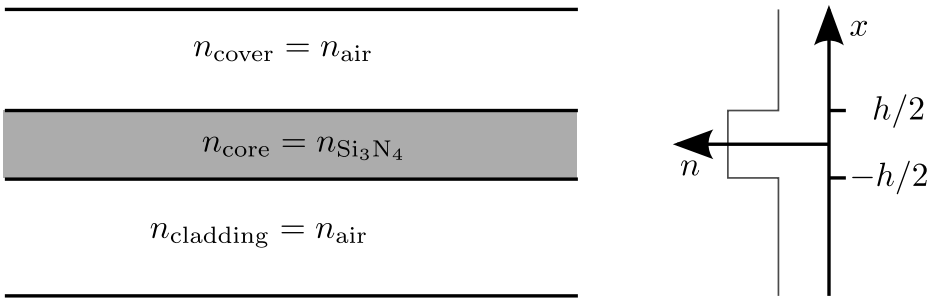

Figure A.1 Graphic representation of the layered medium supporting the waveguide mode in the symmetric case.

In all the cases we start the analysis with the wave equation for the electric field **E** and magnetic field **H** resulting from Maxwell's equations,

$$\begin{aligned} \left(\nabla^2 + \omega^2 \mu\varepsilon\right) \mathbf{E} &= 0; \\ \left(\nabla^2 + \omega^2 \mu\varepsilon\right) \mathbf{H} &= 0. \end{aligned} \tag{A.2}$$

A.1.1 TE modes

For TE modes **E** is parallel to the core-cladding interface. Or in other words perpendicular (or transverse) to the normal of the interface,

$$\mathbf{E} = E_y(x) e^{i\beta z} \hat{y}, \tag{A.3}$$

where the mode travels in the z-direction with β as propagation constant. The magnetic field **H** then follows from the Maxwell-Faraday equation

$$\nabla \times \mathbf{E} = i\omega\mu\mathbf{H}. \tag{A.4}$$

To find the **even TE modes** that propagate, we must have oscillatory solutions for the wave equation in the core and exponential decaying ones in the

cladding and cover. For the different regions we find the following solutions for the fundamental mode

$$\mathbf{E} = \begin{cases} C_0\ e^{-\gamma(|x|-h/2)} & e^{i\beta z}\ \hat{y} & \text{for} & |x| \geq h/2 \\ C_1\ \cos(\kappa x) & e^{i\beta z}\ \hat{y} & \text{for} & |x| < h/2 \end{cases}. \tag{A.5}$$

Now for $|x| > h/2$, we plug this expression for the electric field into the wave equation (Eq. A.2),

$$\begin{aligned} \left(\nabla^2 + \omega^2\mu\varepsilon\right) C_0\ e^{-\gamma(|x|-h/2)}\ e^{i\beta z}\ \hat{y} &= 0 \\ \gamma^2 - \beta^2 + \omega^2\mu\varepsilon &= 0. \end{aligned} \tag{A.6}$$

We remind ourselves that for $|x| > h/2$ we can write

$$\omega^2\mu\varepsilon = \omega^2\mu\varepsilon_0 n_{\text{cl}}^2 = \frac{\omega^2}{c^2} n_{\text{cl}}^2 = k_0^2 n_{\text{cl}}^2 \tag{A.7}$$

to find a relation between γ, β and n_{cl}. And we perform the same steps for region $|x| < h/2$ to find

$$\begin{aligned} -\gamma^2 + \beta^2 &= k_0^2 n_{\text{cl}}^2 \\ \kappa^2 + \beta^2 &= k_0^2 n_{\text{core}}^2. \end{aligned} \tag{A.8}$$

The first boundary condition ensures the continuity for the tangential **E**-field over the interface from medium 1 to 2;

$$E(h/2)|_1 = E(h/2)|_2\ ; \tag{A.9}$$

$$C_0 = C_1 \cos(\kappa h/2), \tag{A.10}$$

the *second boundary condition* ensures continuity of the tangential **H**-field. For the **H**-field,

$$\mathbf{H} = \frac{1}{i\omega\mu_0}\left(i\beta E_y \hat{x} + \frac{\partial E_y}{\partial x}\hat{z}\right) e^{i\beta z}, \tag{A.11}$$

only the second term in brackets is different over the boundary. Thus we find

$$-\frac{\gamma}{i\omega\mu_0} C_0 = -\frac{\kappa}{i\omega\mu_0} C_1 \sin\left(\sin\frac{\kappa h}{2}\right) \tag{A.12}$$

We rewrite the two equations resulting from the boundary conditions in matrix form

$$\begin{bmatrix} 1 & -\cos(\kappa h/2) \\ \gamma & -\kappa\ \sin(\kappa h/2) \end{bmatrix} \begin{bmatrix} C_0 \\ C_1 \end{bmatrix} = \begin{bmatrix} 0 \\ 0 \end{bmatrix}. \tag{A.13}$$

The matrix equation only has solutions if the determinant of the matrix is zero, which brings us to the constraint

$$-\kappa\ \sin(\kappa h/2) + \gamma\ \cos(\kappa h/2) = 0; \tag{A.14}$$

$$\gamma = \kappa \tan(\kappa h/2). \tag{A.15}$$

For **odd TE modes** the solutions for the wave equation are

$$\mathbf{E} = \begin{cases} C_0\ e^{-\gamma(x-h/2)}\ e^{i\beta z}\ \hat{y} & \text{for} \quad x \geq h/2 \\ C_1\ \sin(\kappa x)\ e^{i\beta z}\ \hat{y} & \text{for} \quad |x| < h/2 \\ -C_0\ e^{\gamma(x+h/2)}\ e^{i\beta z}\ \hat{y} & \text{for} \quad x \leq -h/2 \end{cases}. \tag{A.16}$$

The solution for the resulting matrix has $\frac{-\cos}{\sin}$ in stead of $\frac{\sin}{\cos}$ and thus the solution reads

$$\gamma = -\kappa \cot(\kappa h/2). \tag{A.17}$$

To find the mode-solutions we multiply the results from the boundary conditions with $h/2$ from both sides

$$\begin{aligned} \frac{\gamma h}{2} &= \frac{\kappa h}{2} \tan\left(\frac{\kappa h}{2}\right) && \text{for even modes;} \\ \frac{\gamma h}{2} &= -\frac{\kappa h}{2} \cot\left(\frac{\kappa h}{2}\right) && \text{for odd modes.} \end{aligned} \tag{A.18}$$

When we also write equations A.8 in terms of $\frac{\gamma h}{2}$ and $\frac{\kappa h}{2}$ and eliminate β on the way

$$\begin{aligned} \kappa^2 + \beta^2 - (-\gamma^2 + \beta^2) &= k_0^2 n_{\text{core}}^2 - k_0^2 n_{\text{cl}}^2\ ; \\ \kappa^2 + \gamma^2 &= k_0^2 \left(n_{\text{core}}^2 - n_{\text{cl}}^2\right)\ ; \\ \left(\frac{\kappa h}{2}\right)^2 + \left(\frac{\gamma h}{2}\right)^2 &= \left(\frac{h}{2}\right)^2 k_0^2 \left(n_{\text{core}}^2 - n_{\text{cl}}^2\right), \end{aligned} \tag{A.19}$$

which, when written in the same parameters as in the article by Burke [67], reads

$$\begin{aligned} u^2 + q^2 &= R^2 \quad \text{or} \\ u^2 + q^2 - R^2 &= 0. \end{aligned} \tag{A.20}$$

In this equation we plug in q for even or odd modes from Eq. A.18, and we numerically solve for u with the brentq method from the scipy package in python.

We then get β and thereby n_{eff} through

$$\beta = \sqrt{k_0^2 n_{\text{core}}^2 - \left(\frac{u}{h/2}\right)^2} \tag{A.21}$$

$$n_{\text{eff}} = \beta / k_0. \tag{A.22}$$

A.1.2 TM modes

For TM modes we start from the wave equation for **H**. In this case we only have an H_y-component to the **H**-field, from which we deduce the E-field:

$$\left(\nabla^2 + \omega^2\mu\varepsilon\right)\mathbf{H} = 0 \tag{A.23}$$

$$\mathbf{H} = H_y(x)e^{i\beta z}\hat{y} \tag{A.24}$$

$$\nabla \times \mathbf{H} = \varepsilon\frac{\partial \mathbf{E}}{\partial t} = i\omega\varepsilon\mathbf{E} \tag{A.25}$$

$$\mathbf{E} = \frac{1}{i\omega\varepsilon}\left(i\beta H_y\hat{x} - \frac{\partial H_y}{\partial x}\hat{z}\right). \tag{A.26}$$

Here we see the difference between TE and TM mode arising. Where mu is the same for the materials on either side of the interface, ε is different. We consider the fundamental TM mode and look at the boundary conditions.

For **even modes** we find from continuity of H_y and E_z

$$C_0 = C_1\cos(\kappa h/2) \tag{A.27}$$

$$\frac{-\gamma}{i\omega\varepsilon_{\text{cl}}}C_0 = \frac{-\kappa}{i\omega\varepsilon_{\text{core}}}\sin(\kappa h/2). \tag{A.28}$$

From the matrix equation

$$\begin{bmatrix} 1 & -\cos(\kappa h/2) \\ \gamma/\varepsilon_{\text{cl}} & -\kappa/\varepsilon_{\text{core}}\ \sin(\kappa h/2) \end{bmatrix}\begin{bmatrix} C_0 \\ C_1 \end{bmatrix} = \begin{bmatrix} 0 \\ 0 \end{bmatrix} \tag{A.29}$$

we then get the equation for γ

$$-\frac{\kappa}{\varepsilon_{\text{core}}}\sin(\kappa h/2) + \frac{\gamma}{\varepsilon_{\text{cl}}}\cos(\kappa h/2) = 0$$

$$\gamma = \frac{\varepsilon_{\text{cl}}}{\varepsilon_{\text{core}}}\kappa\tan(\kappa h/2)\ ;$$

$$\gamma = \frac{n_{\text{cl}}^2}{n_{\text{core}}^2}\kappa\tan(\kappa h/2), \tag{A.30}$$

and for **odd modes**

$$\gamma = -\frac{n_{\text{cl}}^2}{n_{\text{core}}^2}\kappa\cot(\kappa h/2). \tag{A.31}$$

The python script used to solve for n_{eff} is shown on the next page.

Listing A.1 Python code solving n_{eff} for the symmetric case

```
1  import numpy
2  import scipy.optimize
3
4  # following notation of Appl. Opt. 9, 2444 (1970)
5  def zero_function(u,a,n1,n2,k0,mode='TE',sym='even'):
6    k1=n1*k0
7    k2=n2*k0
8    Rsq=(k1**2-k2**2)*a**2
9    if mode=='TE':
10     factor=1
11   else: # mode=='TM'
12     factor= (n2/n1)**2
13   if sym=='even':
14     q=factor*u*numpy.tan( u)
15   else:
16     q=-factor*u/numpy.tan(u)
17   return q**2-(Rsq-u**2)
18
19 def beta(u,a,n1,k0):
20     k1=n1*k0
21     return numpy.sqrt(k1**2-u**2/a**2)
22
23 def effective_index(a,n1,n2,k0,mode='TE',sym='even'):
24     solution=scipy.optimize.brentq(zero_function,1e-50,
           numpy.pi,args=(a,n1,n2,k0,mode,sym))
25     keff=beta(solution,a,n1,k0)
26     neff=keff/k0
27     return neff
```

A.2 The asymmetric case

The problem becomes asymmetric when the core layer is sandwiched between two different materials. In this case truly even and odd modes no longer exist, as there is no symmetry. This loss of symmetry makes he equations longer and harder to read, but the principle for mode solving is the same as for the above symmetric case.

A.2.1 TE modes

In this case we choose the center ($x = 0$) at one of the interfaces and write for TE modes

$$E_y = \begin{cases} C_1 e^{\gamma_1 x} & \text{for } x \leq 0 \\ C_2 \cos(\kappa x) + C_3 \sin(\kappa x) & \text{for} 0 < x < h \\ C_4 e^{-\gamma_2 (x-h)} & \text{for } x \geq h \end{cases} . \tag{A.32}$$

We plug it into the wave equation to find the following equalities in the 3 regions

$$\begin{aligned} \gamma_1^2 - \beta^2 + \omega^2 \mu \varepsilon &= 0; \\ -\kappa^2 + \beta^2 + \omega^2 \mu \varepsilon &= 0; \\ \gamma_2^2 - \beta^2 + \omega^2 \mu \varepsilon &= 0, \end{aligned} \tag{A.33}$$

which we write for later convenience as

$$\begin{aligned} -\gamma_1^2 + \beta^2 &= (k_0 n_1)^2; \\ \kappa^2 + \beta^2 + (k_0 n_{\text{core}})^2 &= 0; \\ -\gamma_2^2 + \beta^2 &= (k_0 n_2)^2. \end{aligned} \tag{A.34}$$

For the boundary conditions at $x = 0$ we find

$$C_1 = C_2; \tag{A.35}$$

$$\gamma_1 C_1 = \kappa C_3, \tag{A.36}$$

which we plug into $E_y(x)$ right away

$$E_y = \begin{cases} C_1 e^{\gamma_1 x} & \text{for } x \leq 0 \\ C_1 \cos(\kappa x) + C_1 \gamma_1 / \kappa \sin(\kappa x) & \text{for} 0 < x < h \\ C_4 e^{-\gamma_2 (x-h)} & \text{for } x \geq h \end{cases} . \tag{A.37}$$

Now we look at the boundary conditions for $x = h$. First the continuity of the E_y-field:

$$C_1 \left[\cos(\kappa h) + \gamma_1 / \kappa \sin(\kappa h)\right] = C_4, \tag{A.38}$$

$$E_y = \begin{cases} C_1 e^{\gamma_1 x} & \text{for } x \leq 0 \\ C_1 \cos(\kappa x) + C_1 \gamma_1 / \kappa \sin(\kappa x) & \text{for } 0 < x < h \\ C_1 \left[\cos(\kappa h) + \gamma_1 / \kappa \sin(\kappa h)\right] e^{-\gamma_2 (x-h)} & \text{for } x \geq h \end{cases} . \tag{A.39}$$

Then the second boundary condition; continuity of H_z at $x = h$,

$$-\kappa \sin \kappa h + \gamma_1 \cos \kappa h = -\gamma_2 \left[\cos \kappa h + \frac{\gamma_1}{\kappa} \sin \kappa h\right], \tag{A.40}$$

which we divide by $\cos \kappa h$ on both sides

$$-\kappa \tan \kappa h + \gamma_1 = -\gamma_2 - \frac{\gamma_1 \gamma_2}{\kappa} \tan \kappa h \tag{A.41}$$

$$\tan \kappa h = \frac{\gamma_2 + \gamma_1}{\kappa \left(1 - \gamma_1 \gamma_2 / \kappa^2\right)}. \tag{A.42}$$

We simplify this equation in preparation for numerical solving where we'll use $\arctan\left(\frac{x+y}{1-xy}\right) = \arctan x + \arctan y$

$$\kappa h = \arctan\left(\frac{\frac{\gamma_1}{\kappa} + \frac{\gamma_2}{\kappa}}{1 - \frac{\gamma_1}{\kappa}\frac{\gamma_2}{\kappa}}\right) \tag{A.43}$$

$$= \arctan \frac{\gamma_1}{\kappa} + \arctan \frac{\gamma_2}{\kappa} \tag{A.44}$$

We can now combine this equation with the expressions for γ_1, γ_2 and κ from Maxwell's equations,

$$\begin{aligned} \gamma_1 &= \sqrt{\beta^2 - k_0^2 n_1^2} \\ \gamma_2 &= \sqrt{\beta^2 - k_0^2 n_2^2} \\ \kappa &= \sqrt{k_0^2 n_{\text{core}}^2 - \beta^2}, \end{aligned} \tag{A.45}$$

and after some simplification we find

$$\begin{aligned} \frac{\gamma_1}{\kappa} &= \sqrt{\frac{k_0^2 (n_{\text{core}}^2 - n_1^2)}{k_0^2 n_{\text{core}}^2 - \beta^2} - 1} \\ \frac{\gamma_2}{\kappa} &= \sqrt{\frac{k_0^2 (n_{\text{core}}^2 - n_2^2)}{k_0^2 n_{\text{core}}^2 - \beta^2} - 1} \end{aligned} \tag{A.46}$$

So we can write

$$\begin{aligned} h\sqrt{k_0^2 n_{\text{core}}^2 - \beta^2} = \arctan &\sqrt{\frac{k_0^2 (n_{\text{core}}^2 - n_1^2)}{k_0^2 n_{\text{core}}^2 - \beta^2} - 1} \\ &+ \arctan \sqrt{\frac{k_0^2 (n_{\text{core}}^2 - n_2^2)}{k_0^2 n_{\text{core}}^2 - \beta^2} - 1}. \end{aligned} \tag{A.47}$$

This is the equation we solve numerically for β. We search for β between

$$\max(n_1, n_2) < \beta / k_0 < n_{\text{core}},$$

which are the input variables for the scipy brentq numerical solver.

A.2.2 TM modes

For TM modes we perform the calculation analogous to the TE-modes above. And start at the $x = 0$ boundary conditions: continuity of H_y and continuity of E_z and find

$$C_1 = C_2 \tag{A.48}$$

$$C_3 = \frac{\varepsilon_{\text{core}}\ \gamma_1}{\varepsilon_1\ \kappa}. \tag{A.49}$$

Then at $x = h$ we apply the same requirements, starting with contuinity of H_y

$$C_4 = C_1 \left[\cos\kappa x + \frac{\varepsilon_{\text{core}}\gamma_1}{\varepsilon_1\kappa}\sin\kappa h\right], \tag{A.50}$$

Such that

$$H_y = \begin{cases} C_1 e^{\gamma_1 x} & \text{for } x \leq 0 \\ C_1\cos(\kappa x) + C_1\frac{\varepsilon_{\text{core}}\ \gamma_1}{\varepsilon_1\ \kappa}\sin(\kappa x) & \text{for} 0 < x < h \\ C_1\left[\cos(\kappa h) + \frac{\varepsilon_{\text{core}}\ \gamma_1}{\varepsilon_1\ \kappa}\sin(\kappa h)\right] e^{-\gamma_2(x-h)} & \text{for } x \geq h \end{cases}. \tag{A.51}$$

and continuity of E_z at $x = h$

$$\frac{1}{\varepsilon_{\text{core}}}\left[-\kappa\sin\kappa h + \gamma_1\frac{\varepsilon_{\text{core}}}{\varepsilon_1}\cos\kappa h\right] = -\frac{\gamma_2}{\varepsilon_2}\left[\cos\kappa h + \frac{\gamma_1\varepsilon_{\text{core}}}{\kappa\varepsilon_1}\sin\kappa h\right] \tag{A.52}$$

multiply both sides by $\frac{\varepsilon_{\text{core}}}{\cos\kappa h}$

$$\begin{aligned} -\kappa\tan\kappa h + \frac{\gamma_1}{\varepsilon_1\varepsilon_{\text{core}}} &= -\frac{\gamma_2\varepsilon_{\text{core}}}{\varepsilon_2} - \frac{\gamma_1\gamma^2\varepsilon_{\text{core}}^2}{\kappa\varepsilon_1\varepsilon_2}\tan\kappa h \\ \kappa\left(1 - \frac{\gamma_1\gamma_2}{\kappa^2}\frac{\varepsilon_{\text{core}}^2}{\varepsilon_1\varepsilon_2}\right)\tan\kappa h &= \gamma_1\frac{\varepsilon_{\text{core}}}{\varepsilon_1} + \gamma_2\frac{\varepsilon_{\text{core}}}{\varepsilon_2} \\ \tan\kappa h &= \frac{\frac{\varepsilon_{\text{core}}}{\varepsilon_1}\gamma_1 + \frac{\varepsilon_{\text{core}}}{\varepsilon_2}\gamma_2}{\kappa\left(1 - \frac{\gamma_1\gamma_2}{\kappa^2}\frac{\varepsilon_{\text{core}}^2}{\varepsilon_1\varepsilon_2}\right)} \end{aligned} \tag{A.53}$$

from where use $\arctan\left(\frac{x+y}{1-xy}\right) = \arctan x + \arctan y$ again to simplify, with $x, y = \frac{\varepsilon_{\text{core}}}{\varepsilon_{1,2}}\gamma_{1,2}/\kappa$

$$\kappa h = \arctan\frac{\varepsilon_{\text{core}}\gamma_1}{\varepsilon_1\kappa} + \arctan\frac{\varepsilon_{\text{core}}\gamma_2}{\varepsilon_2\kappa} \tag{A.54}$$

Now we can solve this numerically in the same way as the TE modes, but with an additional term $\frac{n_{\text{core}}^2}{n_i^2}$ in front of the square roots on the right side of Equation A.47. The python code is shown on the next page.

Listing A.2 Python code solving n_{eff} for the asymmetric case

```
1  import numpy
2  import pylab
3  import matplotlib.pyplot as plt
4  import scipy.optimize
5
6  def asymmetric_zero_function(beta,h,n1,n_core,n2,k0,mode='
       TE',order=0):
7      k_core=n_core*k0
8      k1=n1*k0
9      k2=n2*k0
10     if mode=='TE':
11         g1=numpy.sqrt((k_core**2-k1**2)/(k_core**2-beta**2)-1)
12         g2=numpy.sqrt((k_core**2-k2**2)/(k_core**2-beta**2)-1)
13     else: # mode=='TM'
14         g1=(n_core/n1)**2*numpy.sqrt((k_core**2-k1**2)/(k_core
               **2-beta**2)-1)
15         g2=(n_core/n2)**2*numpy.sqrt((k_core**2-k2**2)/(k_core
               **2-beta**2)-1)
16     return h*numpy.sqrt(k_core**2-beta**2)-numpy.arctan(g1)-
           numpy.arctan(g2)-order*numpy.pi
17
18 def effective_index(h,n1,n_core,n2,k0,mode='TE',order=0):
19         beta=scipy.optimize.brentq(asymmetric_zero_function,
               max(n1,n2)*k0,n_core*k0,args=(h,n1,n_core,n2,k0,
               mode,order))
20         neff=beta/k0
21         return neff
```

B

From Voigt profile to Faddeeva function

In this appendix we write the complex Voigt profile in the susceptiblity expression in terms of the Faddeeva function $w(z)$ defined as

$$w(z) = \frac{i}{\pi} \int_{-\infty}^{\infty} dt \frac{e^{-t^2}}{z-t}. \tag{B.1}$$

First tabulated by Vera Faddeeva, the function is now implemented in python via scipy as `scipy.special.wofz`*. In the standard decomposition in real and imaginary parts, $w(x+iy) = V(x,y) + iC(x,y)$, V and C are already called the real and imaginary Voigt functions, because with the right prefactors $V(x,y)$ is indeed the Voigt profile. The determination of the right prefactors for V and C is thus the task at hand in this appendix.

The complex Voigt profile in the susceptibility is given by

$$\tilde{V}(\delta, s_0) = \int_{-\infty}^{\infty} dv D(v,T) \tilde{L}(s_0, \delta) = \frac{1}{\sqrt{2\pi} v_{\text{th}}} \int_{-\infty}^{\infty} dv\, e^{-\frac{1}{2}\frac{v^2}{v_{\text{th}}^2}} \frac{2\delta(v)/\gamma - i}{1 + (2\delta(v)/\gamma)^2 + s_0}, \tag{B.2}$$

where we define the complex Lorentz lineshape as $\tilde{L}(s_0, \delta) = \frac{2\delta(v)/\gamma - i}{1+(2\delta(v)/\gamma)^2+s_0}$.

First, we rewrite $\tilde{L}(s_0, \delta)$ into the general mathematical form for a Lorentz profile $L \propto \frac{\gamma/\pi}{x^2+\gamma^2}$

$$\begin{aligned}
\tilde{L}(s_0, \delta(v)) &= \frac{2\delta(v)/\gamma - i}{1 + (2\delta(v)/\gamma)^2 + s_0} = \frac{2\delta(v)\gamma - i\gamma^2}{(1+s_0)\gamma^2 + (2\delta(v))^2} \\
&= \frac{2(\delta_0 - v/\lambda)\gamma - i\gamma^2}{(1+s_0)\gamma^2 + 4(\delta_0 - v/\lambda)^2} = \frac{2(\delta_0\lambda - v)\gamma\lambda - i\gamma^2\lambda^2}{(1+s_0)\gamma^2\lambda^2 + 4(\delta_0\lambda - v)^2} \\
&= \frac{2(v_0 - v)\gamma\lambda - i\gamma^2\lambda^2}{(1+s_0)\gamma^2\lambda^2 + 4(v_0 - v)^2} = \frac{2(v_0 - v)\tilde{v}_\gamma/\sqrt{1+s_0} - i\tilde{v}_\gamma^2/(1+s_0)}{\tilde{v}_\gamma^2 + 4(v_0 - v)^2},
\end{aligned} \tag{B.3}$$

where $\tilde{v}_\gamma = \sqrt{1+s_0}\gamma\lambda$ is the width in velocity space associated with the power-broadened linewidth.

*http://ab-initio.mit.edu/wiki/index.php/Faddeeva_Package

We now indentify the denominator as a special product and use

$$\frac{2(v_0-v)-i\tilde{v}_\gamma}{2(v_0-v)-i\tilde{v}_\gamma}\,\frac{1}{2(v_0-v)+i\tilde{v}_\gamma}=\frac{2(v_0-v)-i\tilde{v}_\gamma}{\tilde{v}_\gamma^2+4(v_0-v)^2} \tag{B.4}$$

to write the above expressions as

$$\tilde{L}(s_0,\delta_0,v)=\frac{\tilde{v}_\gamma}{\sqrt{1+s_0}}\left(\mathrm{Re}\left\{\frac{1}{2(v_0-v)+i\tilde{v}_\gamma}\right\}\right.$$
$$\left.-i\frac{1}{\sqrt{1+s_0}}\,\mathrm{Im}\left\{\frac{1}{2(v_0-v)+i\tilde{v}_\gamma}\right\}\right) \tag{B.5}$$

$$\tilde{V}(s_0,\delta_0,T)=\frac{\tilde{v}_\gamma}{\sqrt{1+s_0}}\int_{-\infty}^{\infty}dvD(v,T)\left(\mathrm{Re}\left\{\frac{1}{2(v_0-v)+i\tilde{v}_\gamma}\right\}\right.$$
$$\left.-i\frac{1}{\sqrt{1+s_0}}\,\mathrm{Im}\left\{\frac{1}{2(v_0-v)+i\tilde{v}_\gamma}\right\}\right). \tag{B.6}$$

As the real and imaginairy part can also be taken after integration, we only need to find an expression for the integral

$$\int_{-\infty}^{\infty}dvD(v,T)\frac{1}{2(v_0-v)+i\tilde{v}_\gamma}, \tag{B.7}$$

in terms of the Faddeeva function $w(z)$. To this end we perform the varial substitution $\eta^2=\frac{1}{2}v^2/v_{\mathrm{th}}^2$ and rewrite the terms to match the form of equation B.1 as

$$\frac{1}{\sqrt{2\pi}v_{\mathrm{th}}}\int_{-\infty}^{\infty}dv\,e^{-\frac{1}{2}\frac{v^2}{v_{\mathrm{th}}^2}}\frac{1}{2(v_0-v)+i\tilde{v}_\gamma}=\frac{1}{\sqrt{2\pi}v_{\mathrm{th}}}\int_{-\infty}^{\infty}dv\frac{e^{-\frac{1}{2}\frac{v^2}{v_{\mathrm{th}}^2}}}{i\tilde{v}_\gamma+2v_0-2v}$$
$$=\frac{1}{\sqrt{2\pi}v_{\mathrm{th}}}\int_{-\infty}^{\infty}v_{\mathrm{th}}\sqrt{2}d\eta\,\frac{e^{-\eta^2}}{i\tilde{v}_\gamma+2v_0-2\eta v_{\mathrm{th}}\sqrt{2}}=\frac{1}{\sqrt{2\pi}v_{\mathrm{th}}}\int_{-\infty}^{\infty}d\eta\,\frac{e^{-\eta^2}}{\frac{i\tilde{v}_\gamma+2v_0}{2v_{\mathrm{th}}\sqrt{2}}-\eta}$$
$$=\frac{1}{\sqrt{2\pi}v_{\mathrm{th}}}\int_{-\infty}^{\infty}d\eta\,\frac{e^{-\eta^2}}{z-\eta}=-\frac{i\,\pi}{2v_{\mathrm{th}}\sqrt{2\pi}}w(z), \tag{B.8}$$

with

$$z=\frac{i\tilde{v}_\gamma+2v_0}{2v_{\mathrm{th}}\sqrt{2}}. \tag{B.9}$$

The complex Voigt profile is thus fully expressed in terms of the Faddeeva function:

$$\tilde{V}(\delta,s_0,T)=\frac{\tilde{v}_\gamma}{\sqrt{1+s_0}}\left(\mathrm{Re}\left\{\frac{-i\pi}{2v_{\mathrm{th}}\sqrt{2\pi}}w(z)\right\}-i\,\mathrm{Im}\left\{\frac{1}{\sqrt{1+s_0}}\frac{-i\pi}{2v_{\mathrm{th}}\sqrt{2\pi}}w(z)\right\}\right)$$
$$=-\frac{\lambda\gamma\sqrt{\pi}}{v_{\mathrm{th}}2\sqrt{2}}\left(\mathrm{Im}\{w(z)\}-i\frac{1}{\sqrt{1+s_0}}\,\mathrm{Re}\{w(z)\}\right), \tag{B.10}$$

with

$$z = \frac{\delta + i\gamma\sqrt{1+s_0}/2}{\sqrt{2}\,v_{\mathrm{th}}/\lambda}. \tag{B.11}$$

To calculate the Faddeeva function, the python implementation `scipy.special.wofz` is used. For large $|z|$, this implementation uses the algorithm introduced by Gautschi [109] and Poppe and Wijers [110] also known as algorithm 680. For small $|z|$, it uses the algorithm 916 by Zaghloul and Ali [111], which provides higher accuracy near the real axis. Recently the cause and remedy for the loss of accuracy near the real axis for algorithm 680 has also been reported [112].

Bibliography

[1] L. Carroll, J.-S. Lee, C. Scarcella, K. Gradkowski, M. Duperron, H. Lu, Y. Zhao, C. Eason, P. Morrissey, M. Rensing, S. Collins, H. Y. Hwang, and P. O'Brien. "Photonic Packaging: Transforming Silicon Photonic Integrated Circuits into Photonic Devices". *Applied Sciences*, **6**, 426, 2016.

[2] W. Bogaerts and L. Chrostowski. "Silicon Photonics Circuit Design: Methods, Tools and Challenges". *Laser & Photonics Reviews*, **12**, 1700237, 2018.

[3] D. Englund, A. Majumdar, M. Bajcsy, A. Faraon, P. Petroff, and J. Vučković. "Ultrafast Photon-Photon Interaction in a Strongly Coupled Quantum Dot-Cavity System". *Physical Review Letters*, **108**, 2012.

[4] A. F. Kockum, A. Miranowicz, S. D. Liberato, S. Savasta, and F. Nori. "Ultrastrong coupling between light and matter". *Nature Reviews Physics*, **1**, 19, 2019.

[5] A. F. Koenderink, A. Alù, and A. Polman. "Nanophotonics: Shrinking light-based technology". *Science*, **348**, 516–521, 2015.

[6] H. Gersen, T. J. Karle, R. J. P. Engelen, W. Bogaerts, J. P. Korterik, N. F. van Hulst, T. F. Krauss, and L. Kuipers. "Real-Space Observation of Ultraslow Light in Photonic Crystal Waveguides". *Physical Review Letters*, **94**, 2005.

[7] B.-S. Song, T. Asano, S. Jeon, H. Kim, C. Chen, D. D. Kang, and S. Noda. "Ultrahigh-Q photonic crystal nanocavities based on 4H silicon carbide". *Optica*, **6**, 991–995, 2019.

[8] L. Novotny and N. van Hulst. "Antennas for light". *Nature Photonics*, **5**, 83–90, 2011.

[9] M. L. Brongersma. "Engineering optical nanoantennas". *Nature Photonics*, **2**, 270–272, 2008.

[10] E. Verhagen, M. Spasenović, A. Polman, and L. K. Kuipers. "Nanowire Plasmon Excitation by Adiabatic Mode Transformation". *Physical Review Letters*, **102**, 2009.

[11] G. Maire, L. Vivien, G. Sattler, A. Kazmierczak, B. Sanchez, K. B. Gylfason, A. Griol, D. Marris-Morini, E. Cassan, and D. Giannone. "High efficiency silicon nitride surface grating couplers". *Optics Express*, **16**, 328–333, 2008.

[12] Z. Cheng and H. K. Tsang. "Experimental demonstration of polarization-insensitive air-cladding grating couplers for silicon-on-insulator waveguides". *Optics Letters*, **39**, 2206, 2014.

[13] J. Kang, Z. Cheng, W. Zhou, T.-H. Xiao, K.-L. Gopalakrisna, M. Takenaka, H. K. Tsang, and K. Goda. "Focusing subwavelength grating coupler for mid-infrared suspended membrane germanium waveguides". *Optics Letters*, **42**, 2094, 2017.

[14] J. Hong, A. M. Spring, F. Qiu, and S. Yokoyama. "A high efficiency silicon nitride waveguide grating coupler with a multilayer bottom reflector". *Scientific Reports*, **9**, 1–8, 2019.

[15] D. Vermeulen, S. Selvaraja, P. Verheyen, G. Lepage, W. Bogaerts, P. Absil, D. Van Thourhout, and G. Roelkens. "High-efficiency fiber-to-chip grating cou-

plers realized using an advanced CMOS-compatible silicon-on-insulator platform". *Optics Express*, **18**, 18278–18283, 2010.

[16] V. J. Cadarso, A. Llobera, M. Puyol, and H. Schift. "Integrated Photonic Nanofences: Combining Subwavelength Waveguides with an Enhanced Evanescent Field for Sensing Applications". *ACS Nano*, **10**, 778–785, 2016.

[17] A. Z. Subramanian, E. Ryckeboer, A. Dhakal, F. Peyskens, A. Malik, B. Kuyken, H. Zhao, S. Pathak, A. Ruocco, A. D. Groote, P. Wuytens, D. Martens, F. Leo, W. Xie, U. D. Dave, M. Muneeb, P. V. Dorpe, J. V. Campenhout, W. Bogaerts, P. Bienstman, N. L. Thomas, D. V. Thourhout, Z. Hens, G. Roelkens, and R. Baets. "Silicon and silicon nitride photonic circuits for spectroscopic sensing on-a-chip [Invited]". *Photonics Research*, **3**, B47–B59, 2015.

[18] X. J. He, T. Y. Li, L. Wang, J. M. Wang, X. H. Tian, J. X. Jiang, and Z. X. Geng. "Electromagnetically induced transparency and slow light in a simple complementary metamaterial constructed by two bright slot-structures". *Applied Physics A*, **116**, 799–804, 2014.

[19] P. van der Straten and H. Metcalf. *Atoms and Molecules Interacting with Light: Atomic Physics for the Laser Era*. Cambridge University Press, 2016. ISBN 9781316106242.

[20] M. H. Anderson, J. R. Ensher, M. R. Matthews, C. E. Wieman, and E. A. Cornell. "Observation of Bose-Einstein Condensation in a Dilute Atomic Vapor". *Science*, **269**, 198–201, 1995.

[21] K. B. Davis, M. O. Mewes, M. R. Andrews, N. J. van Druten, D. S. Durfee, D. M. Kurn, and W. Ketterle. "Bose-Einstein Condensation in a Gas of Sodium Atoms". *Physical Review Letters*, **75**, 3969–3973, 1995.

[22] M. Greiner and S. Fölling. "Optical lattices". *Nature*, **453**, 736–738, 2008.

[23] C. Gross and I. Bloch. "Quantum simulations with ultracold atoms in optical lattices". *Science*, **357**, 995–1001, 2017.

[24] C. Perrella, P. Light, S. A. Vahid, F. Benabid, and A. Luiten. "Engineering Photon-Photon Interactions within Rubidium-Filled Waveguides". *Physical Review Applied*, **9**, 2018.

[25] A. Hilton, C. Perrella, F. Benabid, B. Sparkes, A. Luiten, and P. Light. "High-efficiency cold-atom transport into a waveguide trap". *Physical Review Applied*, **10**, 2018.

[26] T. G. Tiecke, K. P. Nayak, J. D. Thompson, T. Peyronel, N. P. de Leon, V. Vuletić, and M. D. Lukin. "Efficient fiber-optical interface for nanophotonic devices". *Optica*, **2**, 70, 2015.

[27] J. D. Thompson, T. G. Tiecke, N. P. de Leon, J. Feist, A. V. Akimov, M. Gullans, A. S. Zibrov, V. Vuletić, and M. D. Lukin. "Coupling a Single Trapped Atom to a Nanoscale Optical Cavity". *Science*, **340**, 1202–1205, 2013.

[28] M. Scheucher, A. Hilico, E. Will, J. Volz, and A. Rauschenbeutel. "Quantum optical circulator controlled by a single chirally coupled atom". *Science*, **354**, 1577–1580, 2016.

[29] A. Dareau, Y. Meng, P. Schneeweiss, and A. Rauschenbeutel. "Observation of Ultrastrong Spin-Motion Coupling for Cold Atoms in Optical Microtraps". *Physical Review Letters*, **121**, 253603, 2018.

[30] Y. Meng, A. Dareau, P. Schneeweiss, and A. Rauschenbeutel. "Near-Ground-State Cooling of Atoms Optically Trapped 300 nm Away from a Hot Surface". *Physical Review X*, **8**, 031054, 2018.

[31] A. Goban, C.-L. Hung, S.-P. Yu, J. D. Hood, J. A. Muniz, J. H. Lee, M. J. Martin, A. C. McClung, K. S. Choi, D. E. Chang, O. Painter, and H. J. Kimble. "Atom–light interactions in photonic crystals". *Nature Communications*, **5**, 3808, 2014.

[32] C.-L. Hung, S. M. Meenehan, D. E. Chang, O. Painter, and H. J. Kimble. "Trapped atoms in one-dimensional photonic crystals". *New Journal of Physics*, **15**, 083026, 2013.

[33] J. S. Douglas, H. Habibian, C.-L. Hung, A. V. Gorshkov, H. J. Kimble, and D. E. Chang. "Quantum many-body models with cold atoms coupled to photonic crystals". *Nature Photonics*, **9**, 326, 2015.

[34] B. Juliá-Díaz, T. Graß, O. Dutta, D. E. Chang, and M. Lewenstein. "Engineering p -wave interactions in ultracold atoms using nanoplasmonic traps". *Nature Communications*, **4**, 1–7, 2013.

[35] M. Gullans, T. G. Tiecke, D. E. Chang, J. Feist, J. D. Thompson, J. I. Cirac, P. Zoller, and M. D. Lukin. "Nanoplasmonic Lattices for Ultracold Atoms". *Physical Review Letters*, **109**, 235309, 2012.

[36] A. González-Tudela, C.-L. Hung, D. E. Chang, J. I. Cirac, and H. J. Kimble. "Subwavelength vacuum lattices and atom–atom interactions in two-dimensional photonic crystals". *Nature Photonics*, **9**, 320–325, 2015.

[37] D. van Oosten and L. Kuipers. "Trapping a single atom with a fraction of a photon using a photonic crystal nanocavity". *Physical Review A*, **84**, 011802, 2011.

[38] K.-J. Boller, A. Imamoğlu, and S. E. Harris. "Observation of electromagnetically induced transparency". *Physical Review Letters*, **66**, 2593–2596, 1991.

[39] S. E. Harris. "Electromagnetically Induced Transparency". *Physics Today*, **50**, 36–42, 1997.

[40] M. Fleischhauer, A. Imamoglu, and J. P. Marangos. "Electromagnetically induced transparency: Optics in coherent media". *Reviews of Modern Physics*, **77**, 633–673, 2005.

[41] L. V. Hau, S. E. Harris, Z. Dutton, and C. H. Behroozi. "Light speed reduction to 17 metres per second in an ultracold atomic gas". *Nature*, **397**, 594–598, 1999.

[42] C. Slowe, N. S. Ginsberg, T. Ristroph, A. Goodsell, and L. V. Hau. "Ultraslow Light & Bose-Einstein Condensates: Two-way Control with Coherent Light & Atom Fields". *Optics and Photonics News*, **16**, 30–34, 2005.

[43] D. F. Phillips, A. Fleischhauer, A. Mair, R. L. Walsworth, and M. D. Lukin. "Storage of Light in Atomic Vapor". *Physical Review Letters*, **86**, 783–786, 2001.

[44] C. Liu, Z. Dutton, C. H. Behroozi, and L. V. Hau. "Observation of coherent optical information storage in an atomic medium using halted light pulses". *Nature*, **409**, 490–493, 2001.

[45] G. Heinze, C. Hubrich, and T. Halfmann. "Stopped Light and Image Storage by Electromagnetically Induced Transparency up to the Regime of One Minute". *Physical Review Letters*, **111**, 2013.

[46] G. Wang, W. Zhou, H.-L. Chen, Y. Xue, J.-H. Wu, H.-L. Xu, and J.-Y. Gao. "Efficient light storage with reduced energy loss via nonlinear compensation in rubidium vapor". *Laser Physics*, **26**, 065201, 2016.

[47] O. Katz and O. Firstenberg. "Light storage for one second in room-temperature alkali vapor". *Nature Communications*, **9**, 1–6, 2018.

[48] L. Schweickert, K. D. Jons, M. Namazi, G. Cui, T. Lettner, K. D. Zeuner, and L. S. Montana. "Electromagnetically Induced Transparency of On-demand Single

Photons in a Hybrid Quantum Network". *arXiv*, **1808.05921**, 2018.

[49] J. D. Siverns, J. Hannegan, and Q. Quraishi. "Demonstration of slow light in rubidium vapor using single photons from a trapped ion". *Science Advances*, **5**, eaav4651, 2019.

[50] N. Šantić, A. Fusaro, S. Salem, J. Garnier, A. Picozzi, and R. Kaiser. "Nonequilibrium Precondensation of Classical Waves in Two Dimensions Propagating through Atomic Vapors". *Physical Review Letters*, **120**, 2018.

[51] Q. Fontaine, T. Bienaimé, S. Pigeon, E. Giacobino, A. Bramati, and Q. Glorieux. "Observation of the Bogoliubov Dispersion in a Fluid of Light". *Physical Review Letters*, **121**, 2018.

[52] Q. Zhang, X. Cheng, B. He, H. Chen, Z. Ren, and J. Bai. "Size-variable dark-hollow beam generation using cross-phase modulation". *Optics and Laser Technology*, **119**, 2019.

[53] J. D. Swaim, K. N. David, E. M. Knutson, C. Rios, O. Danaci, and R. T. Glasser. "Atomic vapor as a source of tunable, non-Gaussian self-reconstructing optical modes". *Scientific Reports*, **7**, 2017.

[54] S. Romero-García, F. Merget, F. Zhong, H. Finkelstein, and J. Witzens. "Silicon nitride CMOS-compatible platform for integrated photonics applications at visible wavelengths". *Optics Express*, **21**, 14036, 2013.

[55] G. Rempe, R. J. Thompson, R. J. Brecha, W. D. Lee, and H. J. Kimble. "Optical bistability and photon statistics in cavity quantum electrodynamics". *Physical Review Letters*, **67**, 1727–1730, 1991.

[56] C. R. Doerr, L. Chen, Y.-K. Chen, and L. L. Buhl. "Wide Bandwidth Silicon Nitride Grating Coupler". *IEEE Photonics Technology Letters*, **22**, 1461–1463, 2010.

[57] A. Z. Subramanian, S. Selvaraja, P. Verheyen, A. Dhakal, K. Komorowska, and R. Baets. "Near-Infrared Grating Couplers for Silicon Nitride Photonic Wires". *IEEE Photonics Technology Letters*, **24**, 1700–1703, 2012.

[58] C. Lacava, S. Stankovic, A. Z. Khokhar, T. D. Bucio, F. Y. Gardes, G. T. Reed, D. J. Richardson, and P. Petropoulos. "Si-rich Silicon Nitride for Nonlinear Signal Processing Applications". *Scientific Reports*, **7**, 1–13, 2017.

[59] H. Zhang, C. Li, X. Tu, J. Song, H. Zhou, X. Luo, Y. Huang, M. Yu, and G. Q. Lo. "Efficient silicon nitride grating coupler with distributed Bragg reflectors". *Optics Express*, **22**, 21800, 2014.

[60] A. Vochezer, T. Kampschulte, K. Hammerer, and P. Treutlein. "Light-Mediated Collective Atomic Motion in an Optical Lattice Coupled to a Membrane". *Physical Review Letters*, **120**, 073602, 2018.

[61] W. S. Bakr, J. I. Gillen, A. Peng, S. Fölling, and M. Greiner. "A quantum gas microscope for detecting single atoms in a Hubbard-regime optical lattice". *Nature*, **462**, 74–77, 2009.

[62] L. W. Cheuk, M. A. Nichols, M. Okan, T. Gersdorf, V. V. Ramasesh, W. S. Bakr, T. Lompe, and M. W. Zwierlein. "Quantum-Gas Microscope for Fermionic Atoms". *Physical Review Letters*, **114**, 193001, 2015.

[63] A. Omran, M. Boll, T. A. Hilker, K. Kleinlein, G. Salomon, I. Bloch, and C. Gross. "Microscopic Observation of Pauli Blocking in Degenerate Fermionic Lattice Gases". *Physical Review Letters*, **115**, 263001, 2015.

[64] R. W. Wood. "On a Remarkable Case of Uneven Distribution of Light in a Diffraction Grating Spectrum". *Proceedings of the Physical Society of London*,

18, 269–275, 1902.

[65] S. Rytov. "Electromagnetic Properties of a Finely Stratisfied Medium". *Soviet Physics JETP*, **2**, 466–475, 1956.

[66] R. Halir, P. J. Bock, P. Cheben, A. Ortega-Moñux, C. Alonso-Ramos, J. H. Schmid, J. Lapointe, D.-X. Xu, J. G. Wangüemert-Pérez, I. Molina-Fernández, and S. Janz. "Waveguide sub-wavelength structures: a review of principles and applications". *Laser & Photonics Reviews*, **9**, 25–49, 2015.

[67] J. J. Burke. "Propagation constants of resonant waves on homogeneous, isotropic slab waveguides". *Applied Optics*, **9**, 2444–2452, 1970.

[68] V. Liu and S. Fan. "S4 : A free electromagnetic solver for layered periodic structures". *Computer Physics Communications*, **183**, 2233–2244, 2012.

[69] F. Bernal Arango, A. Kwadrin, and A. F. Koenderink. "Plasmonic Antennas Hybridized with Dielectric Waveguides". *ACS Nano*, **6**, 10156–10167, 2012.

[70] B. O. Mußmann. *A Versatile Atom Transport Apparatus for Photonics*. Ph.D. thesis, Universiteit Utrecht, 2016.

[71] K. Voutyras. *Using an Optical Conveyor for Light-Matter Interaction Experiments*. Master's thesis, Universiteit Utrecht, Utrecht, 2017.

[72] P. Siddons. "Light propagation through atomic vapours". *Journal of Physics B: Atomic, Molecular and Optical Physics*, **47**, 093001, 2014.

[73] S. E. Harris and Y. Yamamoto. "Photon Switching by Quantum Interference". *Physical Review Letters*, **81**, 3611–3614, 1998.

[74] M. Yan, E. G. Rickey, and Y. Zhu. "Observation of absorptive photon switching by quantum interference". *Physical Review A*, **64**, 2001.

[75] M. O. Scully. "Enhancement of the index of refraction via quantum coherence". *Physical Review Letters*, **67**, 1855–1858, 1991.

[76] M. O. Scully and M. Fleischhauer. "High-sensitivity magnetometer based on index-enhanced media". *Physical Review Letters*, **69**, 1360–1363, 1992.

[77] D. A. Braje, V. Balić, G. Y. Yin, and S. E. Harris. "Low-light-level nonlinear optics with slow light". *Physical Review A*, **68**, 2003.

[78] J. Zhang, G. Hernandez, and Y. Zhu. "All-optical switching at ultralow light levels". *Optics Letters*, **32**, 1317–1319, 2007.

[79] H. Wu, M. Xiao, and J. Gea-Banacloche. "Evidence of lasing without inversion in a hot rubidium vapor under electromagnetically-induced-transparency conditions". *Physical Review A*, **78**, 2008.

[80] R. M. Camacho, M. V. Pack, J. C. Howell, A. Schweinsberg, and R. W. Boyd. "Wide-Bandwidth, Tunable, Multiple-Pulse-Width Optical Delays Using Slow Light in Cesium Vapor". *Physical Review Letters*, **98**, 153601, 2007.

[81] H. Tanaka, H. Niwa, K. Hayami, S. Furue, K. Nakayama, T. Kohmoto, M. Kunitomo, and Y. Fukuda. "Propagation of optical pulses in a resonantly absorbing medium: Observation of negative velocity in Rb vapor". *Physical Review A*, **68**, 2003.

[82] M. R. Vanner, R. J. McLean, P. Hannaford, and A. M. Akulshin. "Broadband optical delay with a large dynamic range using atomic dispersion". *Journal of Physics B: Atomic, Molecular and Optical Physics*, **41**, 051004, 2008.

[83] P. Siddons, N. C. Bell, Y. Cai, C. S. Adams, and I. G. Hughes. "A gigahertz-bandwidth atomic probe based on the slow-light Faraday effect". *Nature Photonics*, **3**, 225–229, 2009.

[84] L. Weller, R. J. Bettles, P. Siddons, C. S. Adams, and I. G. Hughes. "Absolute

absorption on the rubidium D1 line including resonant dipole–dipole interactions". *Journal of Physics B: Atomic, Molecular and Optical Physics*, **44**, 195006, 2011.

[85] J. Keaveney. *Cooperative interactions in dense thermal Rb vapour confined in nm-scale cells*. Ph.D. thesis, Department of Physics, Durham University, South Road, Durham, DH1 3LE, UK, 2013.

[86] S. Shin and H.-R. Noh. "Analytic calculation of absorption spectra for doppler-broadened alkali-metal atoms at low laser intensity". *Journal of the Korean Physical Society*, **57**, 325–328, 2010.

[87] P. Siddons, C. Adams, C. Ge, and I. Hughes. "Absolute absorption on rubidium D lines: Comparison between theory and experiment". *Journal of Physics B: Atomic, Molecular and Optical Physics*, **41**, 2008.

[88] T. M. Stace and A. N. Luiten. "Theory of spectroscopy in an optically pumped effusive vapor". *Physical Review A*, **81**, 2010.

[89] S. R. Shin and H. Noh. "Effect of optical pumping on transmission spectra of rubidium". In *2009 Conference on Lasers Electro Optics The Pacific Rim Conference on Lasers and Electro-Optics*, pages 1–2. 2009.

[90] T. Lindvall and I. Tittonen. "Effect of optical pumping on alkali-atom Doppler-limited spectra". *Journal of Modern Optics*, **54**, 2779–2793, 2007.

[91] T. Lindvall and I. Tittonen. "Interaction-time-averaged optical pumping in alkali-metal-atom Doppler spectroscopy". *Physical Review A*, **80**, 2009.

[92] P. Siddons, C. S. Adams, and I. G. Hughes. "Off-resonance absorption and dispersion in vapours of hot alkali-metal atoms". *Journal of Physics B: Atomic, Molecular and Optical Physics*, **42**, 175004, 2009.

[93] J. Keaveney, I. G. Hughes, A. Sargsyan, D. Sarkisyan, and C. S. Adams. "Maximal Refraction and Superluminal Propagation in a Gaseous Nanolayer". *Physical Review Letters*, **109**, 2012.

[94] R. Kondo, S. Tojo, T. Fujimoto, and M. Hasuo. "Shift and broadening in attenuated total reflection spectra of the hyperfine-structure-resolved D_2 line of dense rubidium vapor". *Physical Review A*, **73**, 062504, 2006.

[95] L. Weller. *Absolute Absorption and Dispersion in a Thermal Rb Vapour at High Densities and High Magnetic Fields*. Ph.D. thesis, Department of Physics, Durham University, South Road, Durham, DH1 3LE, UK, 2013.

[96] E. Arimondo, M. Inguscio, and P. Violino. "Experimental determinations of the hyperfine structure in the alkali atoms". *Reviews of Modern Physics*, **49**, 31–75, 1977.

[97] C. B. Alcock, V. P. Itkin, and M. K. Horrigan. "Vapour Pressure Equations for the Metallic Elements: 298–2500K". *Canadian Metallurgical Quarterly*, **23**, 309–313, 1984.

[98] L. Weller, T. Dalton, P. Siddons, C. S. Adams, and I. G. Hughes. "Measuring the Stokes parameters for light transmitted by a high-density rubidium vapour in large magnetic fields". *Journal of Physics B: Atomic, Molecular and Optical Physics*, **45**, 055001, 2012.

[99] H. C. W. Beijerinck. "Rigorous calculation of heating in alkali-metal traps by background gas collisions". *Physical Review A*, **61**, 2000.

[100] F. A. Franz and C. Volk. "Spin relaxation of rubidium atoms in sudden and quasimolecular collisions with light-noble-gas atoms". *Physical Review A*, **14**, 1711–1728, 1976.

[101] T. J. Beahn, W. J. Condell, and H. I. Mandelberg. "Excitation-Transfer Collisions

between Rubidium and Helium Atoms". *Physical Review*, **141**, 83–87, 1966.

[102] A. Derevianko, W. R. Johnson, M. S. Safronova, and J. F. Babb. "High-Precision Calculations of Dispersion Coefficients, Static Dipole Polarizabilities, and Atom-Wall Interaction Constants for Alkali-Metal Atoms". *Physical Review Letters*, **82**, 3589–3592, 1999.

[103] J. L. Roberts, N. R. Claussen, J. P. Burke, C. H. Greene, E. A. Cornell, and C. E. Wieman. "Resonant Magnetic Field Control of Elastic Scattering in Cold ^{85}Rb". *Physical Review Letters*, **81**, 5109–5112, 1998.

[104] A. Aprà. *Superfluidity of light in a nonlinear atomic medium*. Ph.D. thesis, Sapienza Università di Roma, 2017.

[105] M. G. Boshier and W. J. Sandle. "Self-focussing in a vapour of two-state atoms". *Optics Communications*, **42**, 371–376, 1982.

[106] Z. Wang, A. Bovik, H. Sheikh, and E. Simoncelli. "Image Quality Assessment: From Error Visibility to Structural Similarity". *IEEE Transactions on Image Processing*, **13**, 600–612, 2004.

[107] Z. Wang, A. C. Bovik, and E. P. Simoncelli. "Structural Approaches to Image Quality Assessment". In *Handbook of Image and Video Processing*, pages 961–974. Elsevier, 2005. ISBN 978-0-12-119792-6.

[108] Z. Wang and A. C. Bovik. "Mean squared error: Love it or leave it? A new look at Signal Fidelity Measures". *IEEE Signal Processing Magazine*, **26**, 98–117, 2009.

[109] W. Gautschi. "Efficient Computation of the Complex Error Function". *SIAM Journal on Numerical Analysis*, **7**, 187–198, 1970.

[110] G. P. M. Poppe and C. M. J. Wijers. "More efficient computation of the complex error function". *ACM Transactions on Mathematical Software (TOMS)*, **16**, 38–46, 1990.

[111] M. R. Zaghloul and A. N. Ali. "Algorithm 916: Computing the Faddeyeva and Voigt Functions". *ACM Transactions on Mathematical Software (TOMS)*, **38**, 15:1–15:22, 2011.

[112] M. R. Zaghloul. "Remark on "Algorithm 680: Evaluation of the Complex Error Function": Cause and Remedy for the Loss of Accuracy Near the Real Axis". *ACM Transactions on Mathematical Software (TOMS)*, **45**, 24:1–24:3, 2019.

Samenvatting

Ons wereldbeeld wordt gevormd door de wisselwerking tussen licht en materie. Kijk maar om je heen: alles wat je ziet, is het directe gevolg van die wisselwerking! Elke lichtstraal die je oog bereikt, heeft immers wisselwerking gehad met materie en wel op precies zo'n manier dat de wereld eruit ziet zoals wij hem kennen. Buiten deze directe beeldvorming, wordt ons wereldbeeld ook beïnvloed door allerhande digitale informatiestromen. Voor deze communicatie tussen elektronische apparaten is de wisselwerking ook van cruciaal belang. Het internetverkeer bestaat uit lichtpakketjes verstuurd door een glasvezelkabel, die bij ontvangst worden omgezet naar een elektronisch signaal met behulp van deze wisselwerking. In deze elektronische apparaten wordt het signaal gelezen, aangepast en opnieuw verzonden als lichtpakket.

Om rekenchips sneller te maken zal elektronica in de toekomst uiteindelijk worden vervangen door fotonica, waarin fotonen (lichtdeeltjes) de informatiedrager zijn in plaats van elektronen. Niets kan immers sneller dan het licht. Met de opkomst van fotonica, wordt de omzetting van en naar een elektronisch signaal bij verzending en ontvangst wellicht overbodig, maar voor het veranderen van het signaal is nog steeds licht-materie wisselwerking vereist. Licht heeft namelijk geen directe wisselwerking met ander licht. Tenminste, niet op de redelijke energieschalen die wij hier beschouwen. Laat twee lichtstralen elkaar snijden en ze verschijnen onveranderd aan de andere kant: lichtstralen botsen niet. Om toch een wisselwerking te verkrijgen, moet er op het snijvlak iets anders aanwezig zijn om de wisselwerking door te geven, te weten materie. Op die manier kunnen fotonische schakelingen worden gemaakt, die dezelfde functionaliteit hebben als hun elektronische evenknieën, zoals de transistor. Deze componenten kunnen dan worden gebruikt om geïntegreerde fotonische chips te maken. In dit proefschift wordt niet gezocht naar een specifieke functionaliteit, maar wordt de fundamentele wisselwerking tussen licht en materie onderzocht. Omdat de chips steeds kleiner worden, zullen functionele componenten zo klein worden, dat zowel licht, materie als de wisselwerking tussen beiden dicht bij de fundamentele limiet komen. De opsluiting van licht in zulke extreem kleine ruimten, zal bovendien zorgen voor hoge intensiteit en daardoor sterke niet-lineaire effecten.

Nanofotonica

Het licht in de bovengenoemde geïntegreerde fotonica is doorgaans opgesloten in een dunne laag van een diëlektricum. De functionalitieit wordt verzorgd door het aanbrengen van specifieke vormen en patronen op de nanoschaal. Hier betreden

we het domein van de nanofotonica ofwel nano-optica, de studie van licht op de nanoschaal. Nog specifieker gezegd beschrijft nanofotonica licht dat ingesloten is in stucturen kleiner dan zijn eigen vacuümgolflengte. Zo kan licht bijvoorbeeld worden geleid, afgeremd en zelfs opgesloten in fotonische kristallen, die een periodieke diëlektrische structuur hebben op de nanoschaal. Plasmonische nanostucturen (van metaal) worden gebruikt als golfgeleiders en nano-antennes, die zorgen voor een koppeling tussen licht in het nabije veld (in de structuur) naar licht in het verre veld (in de vrije ruimte). Dunne nanolagen van een diëlektricum zoals silicium (Si) of siliciumnitride (Si_3N_4) kunnen ook dienst doen als golfgeleiders voor licht in het infrarode respectievelijk zichtbare deel van het spectrum. De inkoppeling van licht kan hier worden verzorgd door een inkoppeltralie met de juiste tralieconstante. De opsluiting in een kleine ruimte zorgt voor hoge piekintensiteit van het licht en steile gradiënten in het elektromagnetische veld van het licht. Hierdoor kan het goed gebruikt worden voor precieze spectroscopie *én* voor het waarnemen en vangen van koude atomen.

Koude atoomgassen

Het onderzoeksveld van koude atomen kwam tot stand door de ontwikkeling van het laserkoelen en -vangen van neutrale atomen. Mede dankzij deze techniek werden in 1995 Bose-Einsteincondensaten van natrium en rubidium geobserveerd, waarvoor Ketterle, Wiemann en Cornell in 2001 de Nobelprijs voor de natuurkunde ontvingen. Met deze techniek kunnen atomen worden gekoeld tot $\sim 100\,\mu K$, waardoor het mogelijk is de atomen daarna over te laden in andere geavanceerde en geraffineerde vallen. Volledig optische vallen worden gebruikt als optisch pincet en optische roosters, die door hoge mate van verstelbaarheid allerlei vastestoffysica kunnen nabootsen in kwantumsimulaties. In een optische fiber met lege kern zijn atomen gevangen in een golfgeleiderval, die een effectieve foton-foton wisselwerking bewerkstelligt.

Voor nog kleinere vallen wordt een beroep gedaan op nanofotonica. Atomen kunnen worden gevangen in het evanescente (uítstekende) veld van een nanotrilholte in een 1D fotonisch kristal aan het eind van een taps toelopende fiber, en in het evanescente veld van een flessenhalstrillingskring. Voor plasmonstructuren zijn ook verscheidene vallen voorgesteld en zelfs een één-atoomsval rond een nanotrilholte in een 1D fotonisch kristal op een golfgeleiderbrug, waarvoor slechts een fractie van een foton nodig is om het atoom te vangen.

In dit proefschrift wordt de wisselwerking onderzocht tussen koude ^{87}Rb atomen en licht in een Si_3N_4 golfgeleidermembraan van 220 nm dikte. Rubidium atomen zijn zeer geschikt voor laserkoeling vanwege hun lage smeltpunt van 40 °C en de beschikbaarheid van relatief goedkope lasersystemen voor de resonantiegolflengte van 780 nm. Voor deze golflengte is Si_3N_4 een geschikt materiaal voor golfgeleiding. De inkoppeling in deze laag met behulp van een oppervlakte inkoppeltralie wordt beschreven in **hoofdstuk 2**. Alle relevante fysica wordt gevangen in een elegante ontwerpformule voor de tralieconstante. Zonder zware bereke-

ningen kan daardoor een traliekoppelaar worden ontworpen voor elke laagdikte, gewenste golflengte en hoek van inval. De ontwerpformule beschrijft een verband tussen de hoek van inval op het tralie en de efficient ingekoppelde golflengte. Dit verband wordt ondersteund door een numerieke simulatie en experimenten in een opstelling met een Fourier microscoop. Met behulp van de ontwerpformule vinden we een inkoppelefficientie van 12% voor een golflengte van 780 nm, een laagdikte van 220 nm en een inkoppelhoek van 3° van de normaal. Deze kleine inkoppelhoek is vereist voor het experiment in hoofdstuk 3, omdat we in de opstelling het membraan slechts van boven kunnen bekijken.

In **hoofdstuk 3** brengen we koude atomen in contact met het evanscente veld van het licht in het golfgeleidende membraan. Omdat de golflengte van het licht groter is dan de dikte van het membraan, steekt de geleide toestand uit in het omliggende vacuüm. In dit evanescente veld kunnen atomen wisselwerken met het licht in het membraan. De atomen worden geprepareerd in een veelzijdige opstelling ter verplaatsing van atomen voor fotonica. Daarin worden de atomen uiteindelijk boven het membraan gevangen in een optisch rooster, gemaakt door twee tegen elkaar in gerichte laserbundels. Wanneer de frequenties van de bundels iets worden verstemd ten opzichte van elkaar, komt het rooster in beweging en bewegen de atomen in deze optische lift richting het membraan. De instellingen van de optische lift worden geoptimaliseerd tot een atoomflux naar het oppervlak van 100 atomen per microseconde. Om de atomen niet te verzadigen sturen we laserlicht met zeer laag vermogen (120 pW) door het membraan. In het uitgekoppelde signaal verwachten we een klein dal van enkele procenten als de atomen arriveren. Met zeer gevoelige, fotontellende detectoren in de opstelling is zo een signaal meetbaar. Het signaal wordt echter verstoord door een mechanische trilling van de opstelling, veroorzaakt door een essentieel bewegend onderdeel in de cyclus van de atoompreparatie. Demping van de verstoring en nabewerking op het gedetecteerde signaal zijn onvoldoende om het signaal van de atomen zichtbaar te maken. In een herontwerp van de opstelling dient dit storende element vervangen te worden.

Hete atoomdampen

In de experimenten met koude atomen wisselwerkt een klein aantal atomen met een klein aantal fotonen. Deze kleine aantallen maken de te meten signalen erg klein, waardoor het moeilijk is de niet-lineaire wisselwerking inzichtelijk te maken. Deze niet-lineaire wisselwerking kan ook worden onderzocht in hete dampcellen, waarin atomen met hoge dichtheid wisselwerken met licht van hoge intensiteit. Als gevolg kunnen opmerkelijke verschijnselen optreden, zoals elektromagnetisch geïnduceerde transparantie, waarbij een aanvankelijk ondoorzichtige damp transparant wordt, wanneer het beschenen wordt met een intense laserbundel. In dichte atoomdampen kan licht ook worden afgeremd met vele ordes van grootte, zodat er zelfs onderzoek wordt gedaan naar het volledig afremmen en opslaan van lichtpulsen in dichte atoomdampen, hetgeen bijzonder interessant is voor

communicatie en synchonisatie in het toekomstige kwantuminternet.

In **hoofdstuk 4** wordt de transmissie van licht op de resonantiefrequentie door een hete rubidium dampcel onderzocht. Geïnspireerd door waarnemingen in onze experimentele metingen, stellen we een model op voor de transmissie door een 10 cm lange rubidium dampcel. Het model bevat niet-lineare effecten in de intensiteit (verzadiging en optisch pompen) én niet-lineare effecten in de dichtheid (botsingsverbreding en botsingstegenpompen). Voor toenemende intensiteit raakt de overgang verzadigd, omdat atomen geen licht kunnen verstrooien gedurende hun relaxatieperiode. Reeds bij lagere intensiteiten wordt optisch pompen van belang, waardoor atomen naar een donkere grondtoestand worden gepompt, waaruit ze moeilijker worden aangeslagen. Botsingen zorgen voor een herverdeling over de grondtoestand en werken het optisch pompen tegen. Door deze niet-lineare processen één voor één aan te zetten in het model, wordt duidelijk welk effect ieder proces heeft op de transmissie. Hieruit concluderen we dat alle processen vereist zijn om tot kwantitatieve overeenstemming te komen.

Voor frequenties boven de atomaire overgang kan een inkomend normaal (Gaussisch) bundelprofiel van vorm veranderen door niet-lineare processen in een rubidium dampcel. Hierdoor ontstaan karakteristieke vormen aan het eind van de dampcel, zoals een ringvormig bundelprofiel. In **hoofdstuk 5** onderzoeken we bij welke intensiteiten en welke verstemmingen ten opzichte van de resonantiefrequentie deze vormen ontstaan. Voor 5 karakteristieke vormen bepalen we de verstemming, waarbij de vorm voorkomt, als functie van de lichtintensiteit en verkrijgen zo vijf verstemmingskrommen. In de transmissiespectra, gemeten bij dezelfde intensiteiten, verschijnen verscheidene pieken en dalen in het gebied boven de resonantie. De verstemmingskrommen komen zeer goed overeen met de positie van de pieken in de spectra. Bovendien kunnen de verstemmingskrommen door de juiste schaling toe te passen op één kromme worden samengebracht: de universele dimensieloze verstemmingskromme. Dit gemeenschappelijke gedrag wijst erop dat deze spontaan gevormde profielen dezelfde oorzaak hebben. Een verschijnsel dat goed overeenkomt met al deze eigenschappen, is het onstaan van soliton toestanden. Solitonen zijn golven die hun vorm en amplitude behouden tijdens de propagatie. In de dichte rubidiumdamp is in zo'n geval de niet-lineaire focusserende breking in balans met de defocusserende diffractie. Om te onderzoeken of de karakteristieke profielen daadwerkelijk het gevolg zijn van spontane solitonvorming, zou men op verschillende posities in de propagatie willen meten. De meest elegante manier om dit te doen, vereist het opzetten van holografie in de ventwegconfiguratie. Hiermee kan zowel de amplitude als de fase van het profiel aan het eind van de dampcel worden gemeten. Met behulp van een ruimtelijke lichtmodulator kan het gemeten profiel daarna weer als inkomend profiel aan de dampcel worden aangeboden voor een volgende propagatieronde door de cel. Zodoende kan het profiel tijdens de propagatie op vaste plekken *in* het dichte gas worden gemeten.

Publicatielijst

Arie Johannes van Lange, Andries Lof and Dries van Oosten, "Non-contact surface grating coupling for arrays of atom-photonic devices", *J. Opt. Soc. Am. B* **37**(4), 921-926 (2020).

A. J. van Lange, P. van der Straten and D. van Oosten, "Combined effect of non-linear optical and collisional processes on absorption saturation in a dense rubidium vapour", *Journal of Physics B: Atomic, Molecular and Optical Physics* **53**(12), 125402 (2020).

Marijn A. M. Versteegh, A. J. van Lange, H. T. C. Stoof and Jaap I. Dijkhuis, "Observation of preformed electron-hole Cooper pairs in highly excited ZnO", *Phys. Rev. B* **85**(19), 195206 (2012).

Dankwoord

"Tijdens je promotie leer je heel veel..., met name over jezelf", zei een wijs persoon mij aan het begin van mijn promotietraject. Aan die uitspraak heb ik vaak teruggedacht in de jaren die volgden, want het is een waarheid als een koe. De spreuk zou in elk lab of kantoor op een tegeltje kunnen! Gelukkig ben ik in de afgelopen jaren niet alleen mijzelf tegengekomen, maar ook vele andere prachtige personen van wie ik veel hulp en steun heb ondervonden. Bedankt voor jullie aandeel in de totstandkoming van dit proefschrift! Zonder jullie was het proefschrift niet geworden zoals het nu is.

Allereerst bedank ik mijn co-promotor en directe begeleider. Dries, de veelzijdigheid van je kennis en kunde binnen de natuurkunde én daarbuiten maken je tot een geweldig adviseur. Je weet net zo makkelijk raad bij vragen over rf-elektronica, computer hardware, uitlijning, theorie, gitaren als kung-fu. Je was altijd beschikbaar voor advies wanneer ik daarom vroeg en je hebt me op vele vlakken veel bijgebracht. Met name de manier van resultaten structureren voor een presentatie of artikel blijft mij bij. Daarbij staat de vraag "Wat is het verhaal dat we willen vertellen" altijd centraal, en je hebt het dan ook liever over 'een verhaal houden' dan over 'een presentatie geven'. Onze inhoudelijke discussies waren meestal interessant, omdat we vaak hele andere bewoordingen kozen om hetzelfde uit te drukken. Tegen de tijd dat we elkaar dan verstonden, was het begrip van het onderwerp aan beide zijden toegenomen. Zo konden we lang praten over zaken waar we het over eens waren. Naast onze communicatiestijl was ook onze aanpak in het lab verschillend doch complementair: de één een rasechte doener en de ander wat meer ... bedachtzaam. Dit kwam treffend tot uiting bij het starten van een nieuwe run van het experiment. Daarbij kan je controleren of je alle parameters goed hebt ingesteld vóórdat je op enter drukt, of nádat je op enter hebt gedrukt en het experiment al loopt. Qua efficiëntie maakt dat eigenlijk niet zoveel uit: de seconden die je wint door de run eerder te starten, verlies je wel weer doordat je alle foutieve runs moet bijhouden. Het gaat meer om de instelling die erachter schuil gaat. Ik hoor je nog zeggen "Druk op enter!". Erg lang stonden we meestal niet samen in het lab. We konden elkaar weliswaar goed helpen om problemen op te lossen, maar het verschil in werkwijze wekte uiteindelijk ook wel wat irritatie op. In het lab is het ook niet altijd eenvoudig geweest: toen ondanks al onze inspanningen de resultaten uitbleven, hebben we de dappere beslissing gemaakt toch een nieuw experiment op te starten. Met veel pijn, moeite en verdriet hebben we de oude opstelling, waarin zoveel manuren zaten, vaarwel gezegd. Ik ben er trots op dat we de moed hebben gehad om deze beslissing te maken en daardoor het promotietraject te volbrengen. En gelukkig heeft deze spanning van het lab onze persoonlijke relatie nooit in de weg gezeten.

Als tweede bedank ik mijn promotor. Peter, de gesprekken met jou over mijn onderzoek leverden altijd wat op. Je hebt de gave om elke situatie met een frisse blik te bekijken, zelfs als je daar zelf ook onderdeel van bent. Hierdoor kreeg het gesprek vaak een onverwachte wending en een onverwachte uitkomst. Dat komt óók doordat je lichaamshouding nog wel eens een andere boodschap uitstraalt. Iedereen in de groep weet dat je tijdens het houden van een verhaal beter niet naar Peter kan kijken, want dan krijg je het idee dat het -op zijn zachts gezegd- niet zo goed gaat, terwijl hij na afloop de spreker oprecht becomplimenteert met diens voordracht. Vaak heb je ook míj verrast met een compliment, dat ik compleet niet aan zag komen in het gesprek, maar juist daarom erg motiverend werkte. Je hebt er in de gesprekken ook voor gezorgd het doel duidelijk voor ogen te houden met de woorden "Wat is er nog nodig voor dít hoofdstuk?" en "Kunnen we hier geen artikel van maken?". Ik waardeer je betrokkenheid, die ik ook een keer gruwelijk heb onderschat. Toen ik jou pas na een week vertelde over de eerste keer dat we transmissie door de waveguide hadden gemeten, viel in plaats van lof verontwaardiging mij ten deel: "Waarom vertel je mij dit nu pas?!". Na duidelijk gemaakt te hebben dat dit écht niet kon, verplichtte je me overigens wel om dit succes *per direct* te vieren, want het belang van het vieren van successen kan niet worden onderschat! Het was dan ook erg schrijnend dat we het inleveren van mijn proefschrift niet samen hebben kunnen vieren vanwege de maatregelen tegen het coronavirus. Ongetwijfeld hadden we anders geproost met McChouffe of Italiaanse wijn! Bij zulk soort feestelijke gelegenheden blijkt ook dat je toegankelijkheid als professor ongeëvenaard is! Hoe 'normaal' je bent gebleven blijkt wel uit het spel "Wie van ons twee is de professor?", dat je eens met Paul in Kafé België speelde. Van de ondervraagden had precies de helft het goed. Wat me verder is bijgebleven uit Kafé België, is dat je niet zomaar een tweede fles McChouffe mag bestellen! Volgens mij ben je daar nog steeds verontwaardigd over!

Next persons to thank are the colleagues who have worked on the same setup: Ole Mußmann and Sandy Pratama. Ole, jij was de eerste promovendus op deze opstelling. Omdat jij de opstelling van de grond af hebt opgebouwd, kon ik met al mijn vragen bij jou terecht. Dank daarvoor! Je vindingrijkheid in het maken van lab-gadgets was inspirerend. Ducttape, tiewraps, kaarsvet en tandartsspiegels: alles werd gebruikt. Een vaardigheid, waarvan het nut niet tot het lab beperkt blijft. Ik heb er nog vaak profijt van in en om het huis. Het is erg jammer dat we de opstelling, die toch voor een groot deel jouw 'kindje' was, niet tot volle wasdom hebben kunnen brengen en naar volle potentie hebben kunnen laten draaien. Maar wat waren we dichtbij! Gelukkig brengt de liefde voor bordspellen en eten ons zo nu en dan nog samen. This love for food is deeply shared with Sandy. Sandy, you amazed me by going on a holiday to Taiwan, just for the amazing food. No sightseeing, just eating. This straightforward approach is also your signature in communication: even for Dutch standards your directness is astounding! Your ability to write code without bugs, was never really transferred into the lab. But your legacy lives on for anyone who wants to align something

'Sandy-perfect'!

Special thanks goes to the students, whom I was fortunate enough to supervise. I say fortunate, because I had a very good working relationship with *all* of them, which is by no means a given. Sebas, you were my first masterstudent and we had a blast. You absorbed all the knowledge on labwork and writing skills, while at the same time we had fun inside and outside the lab. Soon afterwards you decided to switch to a less complicated setup for a PhD and become my colleague and roommate. A decision neither of us ever regretted!
Kostas Voutyras, we had excellent synergy from the start. We pushed the limits of the setup and improved it immensely. We battled mother nature, but had to settle with a draw. Our friendship extends way beyond the lab. I enjoyed the Greek nights in the werfkelder of Rhodos where you played the lute in the band *Tsipouro* and true Greek mezedes were served. *Tsipouro* made Abhi show off his dance skills, made Dashka wear his glasses backwards, and let all of us have a good time! I thank you for all the good BBQ times and for the perfect Tzatziki recipe, and I hope we can still find time to go on that sailing trip to your home island Kea!
Ik bedank bachelorstudenten Tessa Verboven voor het mooie werk aan de optimalisatie van het laden van de MOT en Luuk Visser voor de optimalisatie van de optische lift in de mock-up opstelling. Gijs Buist bedank ik voor het voortzetten van het onderzoek naar voortplanting van licht in een verwarmde cel. Ik ben zeer benieuwd welke verschijnselen je weet bloot te leggen!

Even belangrijk als goede labmaten zijn goeie kantoormaten. En die had ik! Sebastiaan Greveling en Pritam Pai, bedankt voor het fijne gezelschap deze jaren! Sebas, je dacht toch niet dat je er met zo'n karig stukje als masterstudent vanaf kwam in mijn dankwoord?! Je bent een geval apart: door je ijzeren wil en doorzettingsvermogen wel eens een tank genoemd, maar dan wel met een enorme betrokkenheid bij de groep. Met jou erbij wist je dat er altijd iets leuks georganiseerd kon worden, en het ook niet alleen bij plannen bleef! Borrels, bootcamp, boulderen, Jins karaoke, lab karaoke, Sergeis Lonely-Island-afscheid en ga zo maar door. In ons kantoor hebben we ongelooflijk veel gegrapt, gelachen en geklaagd. Soms schoten we wel eens door en moesten we ons afvragen: "Are we the baddies?", maar meestal waren de cynische grappen even onschuldig als die van Statler & Waldorf. Het mooiste was dat ik sommige grappen allang niet meer hoefde te maken, omdat je al wist hoe laat het was wanneer ik je aankeek. En heb je nog een slecht liedje in je hoofd? Wacht, ik help je: "Everybody get up! Singin' 1,2,3,4...".
Pritam 'Owww yeah' Pai, voor jou schrijf ik ook in het Nederlands, want tsjongejonge wat pik je dat snel op! Je lessen begonnen in ons kantoor met muzikale toppers als "Per Spoor (Kedeng kedeng)" en "Ik vind je lekkah!". Later werd het onderwijs naar een hoger niveau gebracht door het woord van de week van Dante, waardoor we er al snel niet meer vanuit konden gaan dat je Nederlands niet verstond. Ook op het gebied van sport konden we elkaar goed verstaan, en we bespraken dan ook vaak de sport van de dag. Djokovic, Federer, Liverpool,

AZ, cricket en rugby kwamen het meest aan bod. En het bleef niet alleen bij praten. Vaak genoeg heb je me overgehaald om mee te doen met bootcamp, tennis en tafeltennis. Ik bedank je voor alle mooie potjes die we gespeeld hebben! Onze onderzoeksonderwerpen raakten elkaar maar zijdelings, waardoor in onze discussies altijd een frisse inval aanwezig was. Je was dan ook de perfecte persoon om mijn proefschrift helemaal proef te lezen. Hartelijk dank hiervoor!

Dan de geweldige technici van onze groep, want aan hen ben ik ook veel dank verschuldigd. Om te beginnen aan Buurman & Buurman: Dante Killian en Paul Jurrius. Dante, niet alleen bedank ik je voor de precies naar wens gemaakte elektronische 'kastjes', maar ook voor alle pepermuntjes die ik in jouw kantoor heb verorberd. Daarbij ging het trouwens meer om de humor die erbij gepaard ging, dan om de hang naar frisse adem. Zelden heb ik iemand ontmoet met een even grote bewondering voor de vieze man van Koot als ikzelf. Er zijn dan ook heel wat pepermuntjes zomaar in één keer ingeslok: "Euwh, wat zonde! Hij was ineens weg! Heb ik hem geeneens goed kunne proevah!". Je mooie two-liners als kleine Italiaanse maffioso zal ik erg gaan missen, net als je guitige blik als er een grap bij je opkwam tijdens de lunch en het meest natuurlijk de vieze-man-begroetingen. "Nou, daaggh!".
Paul, je bent het sociale cement van deze groep! Je praat makkelijk met alles en iedereen en dat maakt je uniek. Ik kon altijd bij je terecht voor een praatje, of het nou voor een klus was of als er gewoon wat dwars zat. Je hebt me geleerd hoe samen te werken met technici. Daar pluk ik nog steeds de vruchten van, want stiekem verschilt de technicus niet zoveel van een 'normaal' persoon en was de les om iemand deelgenoot te maken van je probleem een algemene les in samenwerken! Je was altijd in voor een borrel, ook al drink je er altijd maar twee. En het was mooi om samen met jou inkopen te doen voor de borrel en een dürümpje te happen. Een dankwoord is te kort om alle mooie verhalen over jou helemaal te vertellen, maar ik koester de mooie herinneringen aan reparaties aan de fiets, Rochefort 10 bij Jan Primus, broodjes bij de Sfinx, prachtige snijballen, ongevangen eieren en je fanatisme en drinksnelheid bij borrelspelletjes!
Dan onze lasertechnicus Cees de Kok. Weliswaar wat minder aanwezig dan Buurman & Buurman hierboven, maar niet minder belangrijk. Ik kon altijd op je rekenen als het ging over optica, bestellingen bij leveranciers, betalingen bij journals en de onvermijdelijke bureaucratische hobbels bij die bestellingen en betalingen. Zo rustig als je hiermee om kon gaan, zo geanimeerd kon je deelnemen aan lunchdiscussies over politiek of geloof. Of nog liever: politiek *en* geloof! Om vervolgens ook weer doodgewoon over te gaan tot de orde van de dag: de dagelijkse bepaling der rijpheid des avocado's. Cees, bedankt en geniet van je pensioen en je huis in Spanje!
Verder bedank ik de medewerkers van Instrumentatie voor de hulp en het herhaaldelijk lenen van de spectrum analyser, Ingmar Swart voor het 'lenen' van tantaaldraad uit zijn lab en Daniël Vanmaekelbergh voor gebruik van de optische microscoop.

De samples voor de eerste hoofdstukken van dit proefschrift zijn gemaakt en

gekarakteriseerd op AMOLF. Ook daar heb ik goeie (technische) ondersteuning genoten. Ik bedank Hans Zeijlemaker en in het bijzonder Andries Lof voor het ontwerpen en maken van de samples. Andries, het was prettig om met zo'n enthousiast iemand als jou samen te werken. De communicatie over de vele ontwerpen die we hebben geprobeerd, verliep altijd soepel en oplossingsgericht. Je was altijd bereid om iets nieuws uit te proberen en wilde zelfs nog graag door met het maken van bruggen, toen wij daarmee op moesten houden. Ik vind het dan ook erg leuk dat jij co-auteur bent van het artikel van hoofdstuk 2 en dat jouw golfgeleiderbrug op de kaft is terecht gekomen! Ik bedank de groep van Femius Koenderink voor de hulp bij de karakterisatie van het sample in hun opstelling. Marko Kamp, Hugo Doeleman en Clara Osorio, bedankt voor de uitleg van de opstelling en meedenken over de aanpassingen om de opstelling voor mijn doeleinden geschikt te maken!

De volgende drie dames zijn ook van groot belang geweest; met name voor mijn mentale gesteldheid. Mijke Heldens, Karindra Perrier en Pegah Asgari, bedankt voor de mooie gesprekken en goede adviezen! Mijke, hoe kan je zo meelevend en attent zijn en tegelijkertijd zo sarcastisch?! Complimenten over een nieuwe bril worden moeiteloos afgewisseld met "Kreeg je die broek gratis bij twee pakken waspoeder?" of "Ben je toevallig onderweg naar een lelijke-broekencongres?". Je bent een gummbah-fan in hart en nieren: "Hmmm, dat was weer een heerlijk kopje koffie of thee, Henk!" en zelfs in je frustratie is je bewoording zo creatief, dat het soms grappiger is dan je bedoeling is. Bedankt voor je prachtige, veneinige sneren en je oprechte, eloquente complimenten!
Karindra, met jou had ik altijd mooie lunches. Lunch o'clock betekende vaak ook b#@% o'clock, waarin we frustratie over werk- of thuissituatie lekker van ons af klaagden. Dates kwamen dan ook veel ter sprake: Eerst de mijne, later de jouwe. Omdat we over veel dingen nét iets anders denken, heb ik veel aan die gesprekken gehad. Bedankt! Ook heb ik genoten de verjaardagsfeestjes, een paar stapavonden en van de concerten van je band *Faradays*. Mooi om ook de ontspanning te delen!
Pegah, you arrived in later years, but have made quite the impression. Very soon mysterious notes were appearing on my desk saying things like: "Those guys are inside you building a piece of shit, Arjon. There inside you building a monument to compromise. F—'em, f— those people, f— this whole thing, Arjon". It took me a while to realise it was *you* and you were 'just' quoting Rick & Morty! These jokes and the diabolical giggle are your trademark, but the other side of you is a lovely person asking you how you're really feeling and reading 'Blootpad' together with Dante. I appreciate your genuine enquiries about my well-being, your understanding and willingness to help, and I hope to have been able to help you, when you happened to bump into something.

The following nanophotonic group members of the past and present have played a smaller, but not insignificant role in the completion of this booklet. Om te beginnen bedank ik Jaap Dijkhuis en Marijn Versteegh, door wie ik in mijn masteronderzoek ben geënthousiasmeerd om te promoveren en zij zijn ook

daarna altijd geïnteresseerd gebleven. Ik bedank Allard voor de interesse in mijn werk en discussies over mijn experimenten. En voor de perfecte voordracht van sinterklaasgedichten! Ik ben vereerd dat je in mijn promotiecommissie zit. Then Javier Hernandez, during your time as a postdoc in our group, I learned a lot from your devotion and way of working. You had a great influence on the entire group! Jasper Smits, ik vond het mooi hoe je altijd mijn kantoor binnen kwam denderen met een verhaal over een heel tof gelukt experiment, een idiote Rus op Dota of een dilemma in je datingavonturen. Bijna altijd een mooi verhaal, maar als je zag dat ik druk aan het werk was, zei je na twee zinnen: "Sorry man, ik zie dat je druk aan het werk bent" en liep je net zo makkelijk weer weg. Je enthousiasme is prachtig om te zien en nu je niet zo'n ongeleid projectiel meer bent, kan het alleen maar in je voordeel werken! Jeroen, je bent wat ze noemen een zonderlinge figuur, maar wel een erg interessante. Je wereldbeeld is verfrissend en verbazingwekkend, waardoor je de toehoorder vaak verbouwereerd achterlaat. Bij mij bijvoorbeeld naar aanleiding van het aantal kilo garnalen in je vriezer en jouw versie van een recept voor pasta bolognese: "Ik heb wat tomaten, wortels en uien in een pan gedaan. En wat gehakt en pasta erbij". Ook je lach zal ik niet snel vergeten! Sergei Sokolov, you are just as amazingly uncomformistic as Jeroen: the Russian who's always cold and doesn't like vodka. We've had wonderful times putting a box around your setup at 8pm, flying your drone and discussing its successor 'baby bullet' or debating whether you had an accent or not. Unfortunately I let all the opportunities to practice my Russian slip, except the time when it was the only language option: talking to your mother at your graduation party. That party and the parties organised by you and Anna for both of your research groups, were great integration events and above all a lot of fun! I also thank all the other (former) group members: Sanli Faez, Frits Ditewig, Dashka Baasanjav, Bogdan Yeroshenko, Dorian Bouchet, Jacob Seifert, Marcel Scholten, Zhu Zhang, Pieter Bons and Alexander Groot. And thanks to all the bachelor and master students, whose presence made our group so lively!

Buiten het labwerk om heb ik prettig samengewerkt met mensen in verscheidene gremia. Ik bedank alle leden van het promovendi-overleg Utrecht (PrOUt) en met name Tim van Werkhoven, Ralph de Wit, Willem Janssen, Jeroen Goudsmit en Sophie van Uijen, de leden van de Debye aiocommissie (DAC) en het bestuur van de Nederlandse Natuurkundige Vereniging (NNV). Het is dankzij jullie dat ik me met zoveel plezier in heb kunnen zetten voor deze zaken in de periferie van promoveren in de natuurkunde.

Dan nu tijd voor mijn vrienden! Ik ben jullie enorm dankbaar voor alle steun als het tegenzat, inspiratie als de fut eruit was en ontspanning als de stress opliep. Om te beginnen bedank ik mijn jaarclub voor de mooie diepgaande gesprekken afgewisseld met slap geouwehoer. Joris, Mark, Erwin, Imbert, Peter, Peter en Jeroen, jullie lieten me lachen en zetten me aan het denken: bedankt! Dank aan Steven, Thomas, Willem en Sweitse voor alle bordspellen die we hebben gespeeld en de levensadviezen tussen het spelen door! Voor de sport bedank ik allereerst mijn voetbalteam *Lokomotiv Unitask*, al 15 jaar in het team en nog geen haar

op mijn hoofd die denkt aan een transfer! Ten tweede bedank ik de mannen van het footyteam voor de mooie avonden 7 tegen 7, 6 tegen 6 en de bijbehorende voetbalhumor. Verder bedank ik Lotte de Vos voor het zwemmen en de daarvoor vereiste 'groepsdruk' over en weer, en Stephan Wolbers voor de (s)portavonden met voetbal, tennis of tawny!

Maar de grootste dank gaat uit naar mijn (schoon)familie en in het bijzonder naar mijn lieve moeder en zussen. Jullie onvoorwaardelijke liefde is een groot goed! Tijdens ons altijd prettig samenzijn boden jullie een luisterend oor, stelden jullie de juiste vragen, gaven jullie blijk van genetische herkenning en voorzagen jullie me van nieuwe ideeën en strategieën. Ik voel me *altijd* enorm door jullie gesteund, en zelfs nog meer dan enorm in moeilijke tijden. Dank voor jullie onuitputtelijke steun en liefde!

Dan mijn geweldige paranimfen, Caro en Joris. Ik ben er trots op dat jullie fysiek achter mij zullen staan op 26 augustus, zoals jullie altijd al spreekwoordelijk achter me staan. Ik kan altijd van jullie op aan, en dat al 13 en 23 jaar lang! Als er iets gedaan moet worden, staan jullie paraat. Als er iets gevierd moet worden, staan jullie paraat. En als er iets betreurd moet worden, staan jullie paraat. En als we elkaar lang niet hebben gezien, voelt het bij de ontmoeting toch altijd weer als gisteren; zelfs de tijd kan ons niet uit elkaar drijven. Ik weet zeker dat ik met jullie aan mijn zijde vol vertrouwen en trots zal verdedigen!

Als laatste bedank ik jou, Willemijn. Je hebt zo'n geweldige invloed gehad op mijn leven, vanaf het moment dat ik je heb ontmoet! Je bent zo ontwapenend, dat je mij gemakkelijk tot een prettige openheid verleidt. Je hebt altijd begrip voor mijn twijfels, geduld voor mijn bedachtzaamheid en bewondering voor mijn doorzettingsvermogen en geduld. Bovendien heb ik met jou altijd iets om naar uit te kijken, mede omdat je altijd in bent voor een nieuwe activiteit of een nieuw gerecht. Ik bewonder je gestructureerdheid en de vanzelfsprekendheid waarmee je om hulp kan vragen. Iets waar ik nog van kan leren! Je steunde me deze jaren altijd, maar met name tijdens de periode van schrijven, waarin je zorgde dat het me aan niks ontbrak om hard door te schrijven. Je steun, begrip en liefde waren heel belangrijk voor het resultaat en betekenen ontzettend veel voor me!

About the author

Arie Johannes van Lange was born on 8th October 1985 in Haarlem and grew up in De Rijp, a small town in North-Holland. After graduating from the Murmellius Gymnasium in Alkmaar in 2003, he started his bachelor *Physics and Astronomy* at the Universiteit Utrecht and received his degree in 2008. His bachelor research supervised by Gerard van Rooij at FOM Differ at Rijnhuizen dealt with the hydrogenic retention in carbon under conditions resembling those in a fusion-reactor divertor. During his bachelor programme he was active in student and study associations, including a full-time board position in the study association A–Eskwadraat in 2005-2006.

After his bachelor he enrolled in the master programme *Nanomaterials: Chemistry and Physics* at Utrecht University. In his master's project under supervision of Marijn Versteegh, Jaap Dijkhuis and Henk Stoof, he investigated the existence of electron-hole Cooper pairs in zinc oxide in theory and experiment: he adjusted BCS-theory to find the appropriate critical temperatures and performed low-temperature measurements to show existence of preformed Cooper pairs.

In 2011 he started his PhD research in the group of Dries van Oosten and Peter van der Straten in a project combining cold-atom physics with nanophotonics: the interaction of cold rubidium atoms with light in nanophotonic waveguides. The work performed during his PhD research is described in this thesis and presented at several conferences. During his PhD project he happily supervised a number of bachelor and master students and has been a teaching assistant for courses in Modern Condensed Matter and Electrodynamics. He attended the month-long summer school in theoretical physics in Les Houches in 2012, was a member of the board for the Dutch Physical Society (NNV) on behalf of PhD candidates and was the chairman of the PhD network Utrecht (PrOUt).

In his free time, Arjon enjoys playing football at moderate level, playing board games with friends, travelling and sailing to places with exotic names and cooking exciting new dishes.